J. Fluid Mech. (2019), *vol.* 874, P1, doi:10.1017/jfm.2019.284

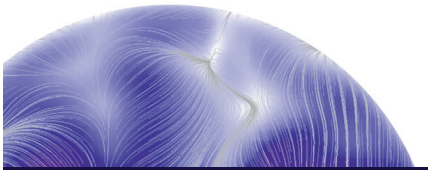

JFM Perspectives
cambridge.org/jfmperspectives

Undulatory and oscillatory swimming

Alexander J. Smits†

Mechanical and Aerospace Engineering, Princeton University, Princeton, NJ 08544, USA

Theory and modelling remain central to improving our understanding of undulatory and oscillatory swimming. Simple models based on added mass can help to give great insight into the mechanics of undulatory swimming, as demonstrated by animals such as eels, stingrays and knifefish. To understand the swimming of oscillatory swimmers such as tuna and dolphins, models need to consider both added mass forces and circulatory forces. For all types of swimming, experiments and theory agree that the most important velocity scale is the characteristic lateral velocity of the tail motion rather than the swimming speed, which erases to a large extent the difference between results obtained in a tethered mode, compared to those obtained using a free swimming condition. There is no one-to-one connection between the integrated swimming performance and the details of the wake structure, in that similar levels of efficiency can occur with very different wake structures. Flexibility and viscous effects play crucial roles in determining the efficiency, and for isolated propulsors changing the profile shape can significantly improve both thrust and efficiency. Also, combined heave and pitch motions with an appropriate phase difference are essential to achieve high performance. Reducing the aspect ratio will always reduce thrust and efficiency, but its effects are now reasonably well understood. Planform shape can have an important mitigating influence, as do non-sinusoidal gaits and intermittent actuation.

Key words: flow–structure interactions, propulsion, swimming/flying

1. Introduction

The fluid dynamics of underwater propulsion is an area of research that has stimulated vigorous collaborations between biologists and engineers, and fostered

† Email address for correspondence: asmits@princeton.edu

numerous mathematical treatments, experimental investigations and numerical simulations. It has contributed to a deeper understanding of the underlying biology of fish and aquatic mammals, and provided inspiration for developing innovative new underwater systems. This level of attention is no doubt driven at least in part by the grace and beauty displayed by many swimming animals. There is also the possibility that evolution has led to propulsive mechanisms that are inherently more efficient, manoeuvrable and quieter than those currently in use in marine applications.

The literature surrounding this field is extensive. The books by Gray (1968), Blake (1983*a*) and Videler (1993) provide a comprehensive portrait of fish swimming, while more specific topics, such as the hydrodynamics and energetics of fish propulsion, dolphin hydrodynamics and performance, fish swimming mechanics and behaviour in altered flows, passive and active flow control by swimming fishes and mammals and the mechanics and control of swimming, are considered by Webb (1975), Fish & Rohr (1999), Colgate & Lynch (2004), Fish & Lauder (2006) and Liao (2007), respectively, and Lauder & Tytell (2005) present a particularly insightful review of the hydrodynamics of undulatory propulsion. The analyses by Lighthill (1969) for slender bodies and Wu (1961) for thin flexible membranes continue to be influential, as do the considerations on hydrodynamic scaling by Triantafyllou, Triantafyllou & Yue (2000) and Triantafyllou *et al.* (2005). There are also three notable popular articles that have helped introduce a broad audience to the subject (Webb 1984; Triantafyllou & Triantafyllou 1995; Fish & Lauder 2013). This is by no means a comprehensive list.

Our aim here is to supplement this body of work with a contemporary perspective on our understanding of the fundamental fluid dynamic aspects of oscillatory and undulatory swimming, and to consider the implications for novel propulsors for future underwater vehicles. We will primarily consider motions at cruise condition, where the animal is moving in a straight line at an average speed that is constant. This is expected to be the most efficient condition, in that it is the mode chosen by fish for sustained swimming (Fish & Rohr 1999; Triantafyllou *et al.* 2005).

1.1. *Swimming styles*

The biology is evidently rich with complexity, encompassing a vast range of body morphologies and swimming styles. A primary sorting can be made on the basis of Reynolds number. When viscous forces dominate, as they do for micro-organisms such as bacteria, propulsion requires non-reciprocal motion that breaks symmetry as a consequence of the linearity of the governing equations. Very small fish, with lengths of a millimetre or so, also live in this world. However, for somewhat larger fish, say of length 10 mm, swimming at one body length per second, the Reynolds number will exceed 100, and reciprocal motions become the dominant form of propulsion.

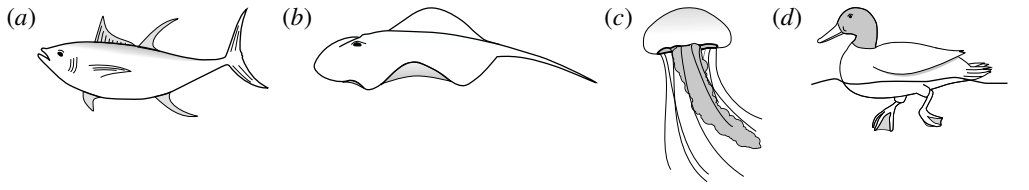

FIGURE 1. Examples of four swimming types: (*a*) oscillatory – tuna; (*b*) undulatory – ray; (*c*) pulsatile jet – jellyfish; and (*d*) drag based – duck. Reproduction with permission from Van Buren, Floryan & Smits (2019*a*).

For such organisms, we can identify four major types of swimmers: undulatory, oscillatory, pulsatile and drag-based, as illustrated in figure 1. Undulatory swimmers are animals that generate a travelling wave along their body or propulsive fins to push fluid backwards. Examples include eels, lampreys and some rays. Oscillatory swimmers, such as salmon, tuna, dolphins and sharks, propel themselves primarily using a semi-rigid caudal fin or fluke that is oscillated periodically. Animals that periodically ingest a volume of water and then discharge it impulsively to produce thrust by reaction are called pulsatile swimmers, and examples include jellyfish, squid, frogfish and some molluscs (Fish 1987; Dabiri 2009). Finally, drag-based swimmers such as humans, turtles, seals and ducks propel a bluff body such as a rigid flipper through the water to generate thrust (Fish 1996).

Our principal consideration here will be undulatory and oscillatory swimmers that use body and/or caudal fin locomotion. In the conventional view, anguilliform swimmers such as eels and lampreys pass a travelling wave of increasing amplitude along the whole body, whereas for thunniform swimmers such as tuna and mackerel the anterior part of the body is held to be relatively stiff, and only the posterior third of the body is used for propulsion, with the notable presence of a high-aspect-ratio caudal fin (Lindsey 1978; Sfakiotakis, Lane & Davies 1999). We shall see that this distinction is not entirely accurate, and also less useful than one based on the wavelength of actuation, in that, broadly speaking, undulatory swimmers display a wavelength shorter than their body length, and oscillatory swimmers display a wavelength longer than their body length.

1.2. *Wake structure*

The hydrodynamic structure of the wake is determined by the Reynolds number, the non-dimensional frequency and the non-dimensional amplitude of the motion. The non-dimensional frequency is typically expressed either as the Strouhal number St, or the reduced frequency k. Here, $St = 2af/U$ and $k = fc/U$, where a is the amplitude of oscillation of the tail, f is the frequency of oscillation (Hz), U is the speed of swimming and c is a characteristic length such as the length of the body or the chord of the caudal fin or fluke.

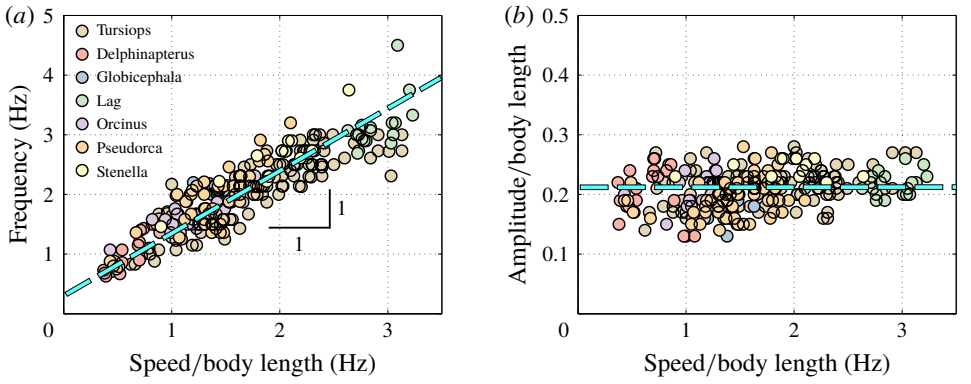

FIGURE 2. (*a*) Fluke-beat frequency and (*b*) non-dimensional fluke-beat amplitude as functions of length-specific swimming speed for several odontocete cetaceans. Original data from Rohr & Fish (2004), replotted as in Floryan *et al.* (2017*a*), reproduced with permission.

Triantafyllou, Triantafyllou & Grosenbaugh (1993) analysed the swimming performance of a wide variety of fishes and mammals, from bream to sharks to dolphins, and found that they swam broadly within the range of Strouhal numbers from 0.2 to 0.35. This observation echoes a number of earlier studies (for example, Bainbridge 1958) that showed that fish tend to increase their swimming speed by increasing their tail beat frequency while keeping their amplitude of motion more or less constant (typically 15–20 % or so of the body length), in effect keeping their Strouhal number fixed. Similar results were found for cetacean swimming by Fish & Rohr (1999) (see figure 2), although for rainbow trout Webb, Kostecki & Stevens (1984) found that the amplitude of the tail beat relative to the body size decreased with the size of the specimen.

Triantafyllou *et al.* (1993) made two additional observations. First, the efficiency of a heaving and pitching foil displayed a peak in this 'optimal' range ($0.2 \leqslant St \leqslant 0.35$). Second, the average velocity profile in the wake resembles a jet, and they showed that the jet profile is convectively unstable over a narrow range of frequencies that corresponds well to this Strouhal number range. Triantafyllou *et al.* (1993) therefore concluded that fish swim in this particular Strouhal number range because it corresponds to the frequency of maximum amplification and therefore it is expected to be most efficient. In addition, the associated wake structure resembled a reverse von Kármán street pattern (Weihs 1972), that is, a pattern akin to the von Kármán vortex street but with the signs of the vortices reversed so that thrust is produced instead of drag. No Reynolds number effects were considered, presumably because the Reynolds numbers for their data set were relatively high (10^4 to about 10^6 based on body length). However, as we will show, viscous effects may continue be important even at very high Reynolds numbers (see § 3.1).

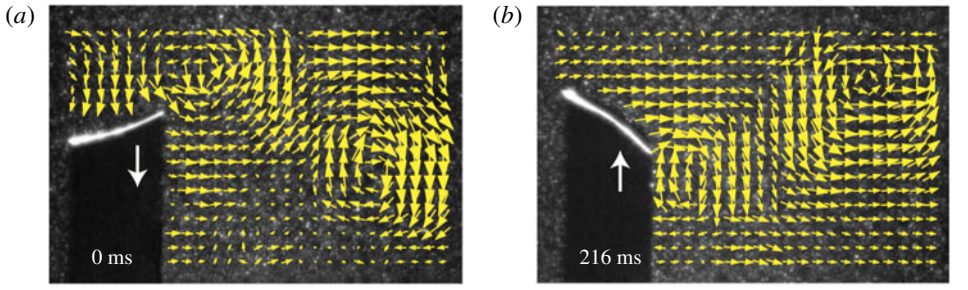

FIGURE 3. Representative flow fields in the wake of the oscillating caudal fin of sunfish during steady swimming at 1.1 L/s, where L is total body length. Adapted with permission from Drucker & Lauder (2001).

This view, that the reverse von Kármán street wake pattern corresponds to the most efficient swimming mode, and that it is typical of cruising fish, is still widely held. At the time, however, evidence for the ubiquity in nature of the reverse von Kármán street wake structure was rather scant, and it was not really until the advent of particle image velocimetry (PIV) that the vortex patterns produced by fish could be examined in detail (Müller *et al.* 1997; Drucker & Lauder 2001; Lauder & Tytell 2005). An early example showing the formation of a reverse von Kármán street wake, as visualized in the plane of the tail motion, is shown in figure 3. This type of structure is also called 2S, that is, two vortices are shed into the wake per shedding cycle, after Williamson & Roshko (1988) who coined the phrase with respect to wakes generated by oscillating cylinders.

A different example is given in figure 4(*a*) for an American eel in steady swimming. Large vortices are shed by the flapping tail, but when viewed in the plane of the tail motion this wake pattern does not resemble that of a reverse von Kármán street. The wake of a robotic lamprey, another undulatory swimmer, shown in figure 4(*b*), displays a very similar vortex pattern, as do alligators (Fish & Lauder 2013), and although dolphins typically generate 2S wakes they also sometimes generate this type of wake (Fish *et al.* 2014). We see a structure that is more reminiscent of Williamson and Rosko's 2P wake structure, where two vortex pairs are shed per cycle. It is clear that different wake patterns are possible, and we shall see that efficient swimming is not necessarily restricted to one particular wake pattern.

These visualizations in the plane of the tail motion tend to ignore the fact that fish wakes will naturally be highly three-dimensional, even if the caudal fin has a large aspect ratio. As anticipated by Lighthill (1969), the spanwise vorticity shed from the central part of the caudal fin is much greater than what can be shed from the tapered tips, and so the vortex lines shed from the central part must bend downstream. Further downstream, they must turn inwards, and then close up when they reach the vorticity of opposite sign shed by the fin half a period earlier. This

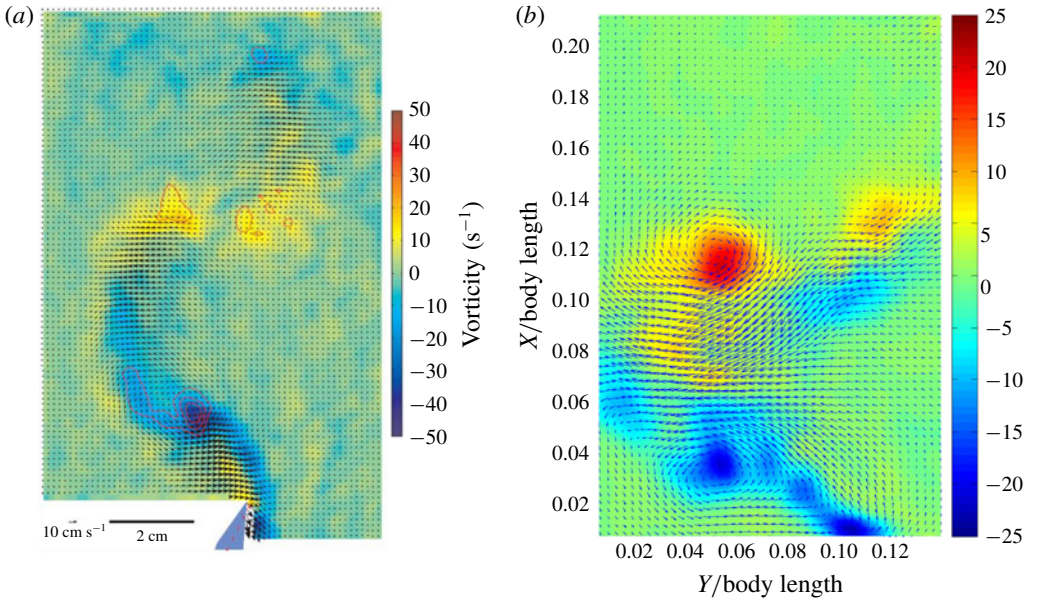

FIGURE 4. Phase-averaged velocity fields in the wake of (*a*) an American eel moving at constant speed, adapted with permission from Tytell & Lauder (2004), and (*b*) a robotic lamprey, adapted with permission from Hultmark, Leftwich & Smits (2007). Contours give levels of spanwise vorticity. The views represent the flow field at a similar phase in the motion.

line of thinking suggests that the wake consists of a series of vortex rings or loops of alternate sign, and that the reverse von Kármán street is seen only in a particular cross-section through this structure (see also Videler 1993). Nauen & Lauder (2002) make this description more explicit by direct observations on chub mackerel at Strouhal numbers of approximately 0.4. Thus, the stability argument advanced by Triantafyllou *et al.* (1993) for two-dimensional flows is unlikely to translate directly to actual fish wakes.

In addition, we should note that for a free swimming fish moving at constant speed no resultant force is acting, and the overall wake in the frame of the fish motion is momentumless. So even if the cross-sectional view of the wake resembles a 2S or a 2P structure the vortices appear aligned in such a way so that there is no net axial jet. This is illustrated by the wakes shown in figure 4(*a*,*b*), visualized under free swimming conditions.

We will show here that we should treat the wake structure and the swimming performance (thrust, power and efficiency), as two separate but inter-related topics, in that there is no obvious one-to-one connection between them. Zhang (2017), in the context of a flapping wing, cautioned that examining the flow pattern is much like looking at the footprints of terrestrial animals; although some information can be gleaned from the wake, it does not tell the whole story. Similarly, Taylor

(2018) writes that an explanation of propulsive efficiency given only in terms of the wake feels a little incomplete, and notes that Eloy (2012) suggested that efficient development of the wake may be a consequence, rather than a cause, of efficient propulsion. See also Floryan, Van Buren & Smits (2019).

1.3. *Measures of performance*

We have a particular interest in the thrust, power and efficiency of a wide variety of 'swimmers', a term that may include animals, robots, as well as isolated propulsors such as oscillating foils and flexible plates. As indicated earlier, the principal non-dimensional variables governing the performance are the Strouhal number, St, the reduced frequency, k, and the chord-based Reynolds number, $Re = cU/\nu$, where ν is the fluid kinematic viscosity. We also have the aspect ratio $\mathcal{AR} = s^2/A$, where s is the span and A is the planform area of the propulsor, as well as some measure of the body flexibility such as the effective stiffness. The results on propulsive performance are usually presented in terms of the non-dimensional thrust output coefficient, input power coefficient and Froude efficiency, conventionally defined according to

$$C_T = \frac{T}{\frac{1}{2}\rho U^2 A}, \quad C_P = \frac{P}{\frac{1}{2}\rho U^3 A}, \quad \eta = \frac{TU}{P} = \frac{C_T}{C_P}, \tag{1.1a–c}$$

where T is the net streamwise (x-direction) component of the force developed by the motion, P is the power expended and ρ is the fluid density. Unless otherwise indicated, we consider only time averaged values.

What about the drag on the body? The net thrust, T, is given by the thrust produced by the motion, F_x, minus the drag force, D, so that $T = F_x - D$. For a body in steady self-propelled motion (free swimming), the total thrust is equal to the total drag, so that $T = 0$, $C_T = 0$ and the efficiency can no longer be defined. In such cases the cost of transport CoT is often used, as first introduced by Von Kármán & Gabrielli (1950). That is, for an animal of weight mg, $CoT = P/(mgU)$. This is a useful quantity to help compare the performance of dissimilar animals where P is given by the metabolic rate, and the minimum CoT is assumed to occur at the velocity at which the animal can cover the largest distance for the smallest energy cost. Fish & Rohr (1999) note that fish have the lowest CoT for any vertebrate, and that cetaceans have values two or three times higher than similar sized fish, probably because of the higher maintenance costs. Intriguingly, they found that the minimum value of the CoT for fish and mammals is a function of body mass m, scaling approximately according to $m^{-0.25}$.

In some animals, we can separate the sources of drag from the sources of thrust. If, for example, we can identify the caudal fin as the main source of propulsive force and the body as the main source of drag, then the caudal fin needs to generate a net positive force (its thrust F_x minus its drag D_p) in order to overcome the drag offered by the body D_b. In this case, the fin can be considered in isolation, and we

can define the efficiency of the propulsor as TU/P, where P is the power necessary to generate the net propulsor thrust $T = F_x - D_p$, ignoring the question of how efficiently the input power was generated to begin with (that is, we are concerned with fluid mechanical efficiency and not metabolic efficiency). Furthermore, the net propulsor thrust T then determines the steady swimming speed of the body plus propulsor, through the force balance $T = F_x - D_p = D_b$. These broad assumptions are often used in propulsive models for oscillatory swimmers such as tuna and dolphins (see § 3).

1.4. *Undulatory and oscillatory swimming*

To compare the swimming styles of undulatory and oscillatory swimmers, we consider how the shape of the body midline changes during an actuation cycle. The results are shown for a number of different species in figure 5. The distinction among swimmer types is obviously less clear than that implied by the conventional view that there are distinct morphological differences between undulatory and oscillatory swimmers (Lindsey 1978; Sfakiotakis *et al.* 1999). That is, all four types shown here display a midline motion that grows similarly in amplitude along the body length. Although the anguilliform motion grows more uniformly along the body compared to other species, there is no great distinction among the other three types where the motion is largely restricted to the posterior one third of the body.

Instead of using body morphology to distinguish oscillatory and undulatory swimmers, we therefore use a criterion based on the mechanism that generates thrust. In the first group we have animals that pass a travelling wave along the body such as eels, lampreys, snakes. We call these undulatory swimmers because the wavelength of the undulation is equal to or shorter than the length of the body. Some rajiform species such as the blue spotted stingray and Atlantic stingray similarly undulate their pectoral fins to generate thrust, and amiiform and gymnotiform swimmers such as the bowfin and knifefish may also be included in this group, since they move by propagating undulations along their elongated anal or dorsal fin, with a wavelength shorter than the length of the fin (Fish 2001).

In the second group we have carangiform and thunniform swimmers where the primary mechanism for producing thrust is a prominent caudal fin. Here, the wavelength of the undulation is longer than the body length, and so the caudal fin describes a combination of heaving and pitching motions. Some species of ray such as the manta ray and cownose ray move their pectoral fins in a similar motion, which happens when the wavelength of the undulation is longer than the chord of the pectoral fin (called mobuliform swimming). We also include cetaceans in this group, because their primary propulsive force is due to the oscillatory motion of the fluke in the vertical plane. The swimming kinematics of cetaceans are characteristic of the thunniform mode, also known as carangiform with lunate tail (Lighthill 1969, 1970; Webb 1975; Lindsey 1978). The role of flexibility varies widely, in that the

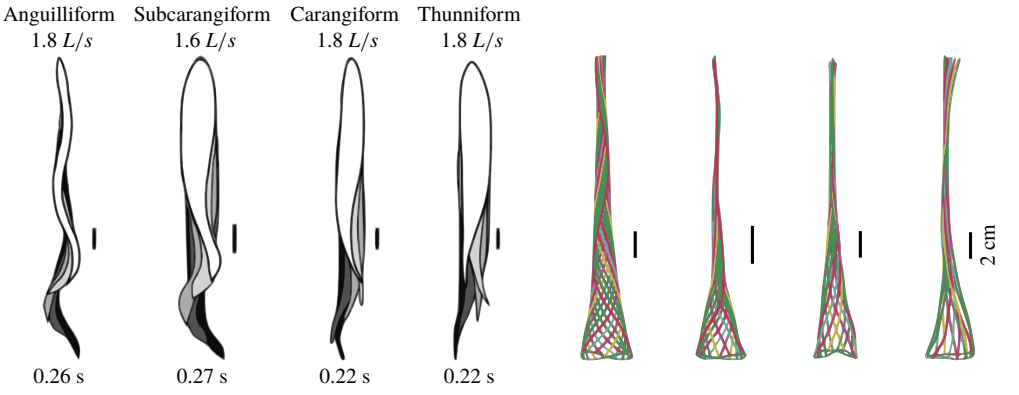

FIGURE 5. Four classical categories of fish undulatory propulsion illustrated with fish outlines and midlines derived from recent experimental data. Outlines of swimming fishes are shown above with displacements that to illustrate forward progression, while midlines at equally spaced time intervals throughout a tail beat are superimposed at right, aligned at the tip of the snout; each time is shown in a distinct colour. Anguilliform mode based on *Anguilla*, subcarangiform mode based on *Lepomis*, carangiform mode based on *Scomber* and thunniform mode based on *Euthynnus*. All fishes were between 20 and 25 cm total length (L), and swam at a similar speed of 1.6 to 1.8 L/s. Times shown indicate duration of the tail beat. Scale bars = 2 cm. Adapted with permission from Lauder & Tytell (2005).

caudal fin of tuna are stiff compared to the rather flexible flukes of dolphins, and manta rays can actively control the flexibility of their pectoral fins by muscle action.

In some species, however, it is not always possible to make a clear demarcation between undulatory and oscillatory swimming. Sharks, for example, display motions ranging from anguilliform to thunniform (Wilga & Lauder 2004). They also have a distinctive heterocercal tail, that is, an asymmetric caudal fin shape, and so are expected to generate asymmetric wake structures (Flammang *et al.* 2011). Nevertheless, the broad distinction based on the propulsive mechanism proves to be useful as an organizing principle.

In what follows, we first consider undulatory swimming, and then oscillatory swimming. Mobuliform swimmers like manta rays will be considered separately, in that they are a good example of animals that actively control the shape of their fins to change the waveform of actuation. Some basic themes will emerge. One, there is no one-to-one correspondence between wake structure and efficiency. Two, the primary velocity scale for propulsion is the characteristic velocity of the trailing edge. Three, the drag of the propulsor is crucially important in determining its thrust and efficiency. Four, flexibility (either passive or active) can have a major effect on performance, and a proper exploitation of flexibility seems essential to attain high thrust and efficiency.

2. Undulatory swimming

Taylor (1952) was the first to estimate the thrust produced by long and narrow animals such as snakes, eels and marine worms, by 'considering the equilibrium of a flexible cylinder immersed in water when waves of bending of constant amplitude travel down it at constant speed. The force on each element of the cylinder is assumed to be the same as that which would act on a corresponding element of a long straight cylinder moving at the same speed and inclination to the direction of motion'. This approach is now known as the 'resistive model' of thrust production, and the total thrust is found by integrating the streamwise contributions from all the segments along the body. By using an appropriate estimate for the drag coefficient on each segment, and by allowing the amplitude of the bending wave to vary along the body, the model can be adapted to non-circular cross-sections, varying locomotion profiles, and a wide range of Reynolds numbers. For example, it was used by Gray & Hancock (1955) to analyse very low Reynolds number swimmers using a linear drag dependence. An important result is that for high Reynolds numbers the bending wave needs to move down the body at a speed greater than the swim velocity to achieve positive thrust.

As pointed out by Lauder & Tytell (2005) and many others, the theory is limited by the assumption of small-amplitude bending waves, and the assumption that the resistive force experienced by each segment is quasi-steady and independent of the adjacent segments. In addition, the drag coefficients used in the theory are determined from experiments on steady cylinders, and in unsteady flow added mass forces will appear, and the circulatory forces would also change from their steady flow values, at least for high Reynolds numbers. Therefore, although it is still widely used for low Reynolds number applications (see, for example, Zhong *et al.* (2013)), for high Reynolds number flows where accelerations (such as those associated with added mass effects) need to be considered, resistive models have largely been replaced by approaches based on some form of slender body theory.

2.1. *Slender body theory*

Lighthill (1960) was the first to apply slender body theory (originally developed in the context of airships and supersonic flow by Munk 1924; Tsien 1938) to the swimming of slender fish, that is, 'either a fish or a swimming mammal, whose dimensions and movements at right angles to its direction of locomotion are small compared with its length, while its cross-section varies along it only gradually'. It is similar to thin airfoil theory in the sense that the derivatives are evaluated at the body centreline without consideration to its thickness.

Several other assumptions are made in the basic theory. First, the flow is taken to be inviscid, so that the instantaneous energy conservation in aquatic animal self-locomotion is given by

$$P = E + TU, \tag{2.1}$$

where P is the power exerted by the animal, E is the rate of change of the kinetic energy of the fluid and TU is the rate of work done to produce thrust T. In evaluating the efficiency, the drag is taken to be zero, and therefore the efficiency in slender body theory measures the part of the power that goes to produce thrust, compared to the total power input that includes the loss of energy to the fluid (that is, the wake). Second, the theory assumes that the force on each segment of the body is given by the reactive force due to the acceleration of the added mass per unit length of the segment, which is why it is sometimes called a 'reactive' model. This reactive force is taken to act only in the y-direction, which is normal to the direction of the forward progress of the animal (taken to be the x-direction). Circulatory forces are not considered. Third, it assumes that each segment is independent of the next, which is the same infinite cylinder approximation used in resistive theory. Fourth, motions are taken to be small (although the theory was extended to large-amplitude motions by Lighthill 1971).

We now summarize the salient results. The notation and approach follow Wu (2011), and the theory applies equally well to long slender bodies and thin membranes (that is, flexible ribbon plates of constant width where the width is small compared to its length). We give more details than might be wise, but the results will find a number of applications in the rest of this paper.

For a travelling wave described by $h(x, t)$, the local velocity in the y-direction is given by $V(x, t) = (\partial/\partial t + U\partial/\partial x)h$. The associated force per unit length is called the specific lift $\mathcal{L}$ (Wu 2011), where $\mathcal{L} = (\partial/\partial t + U\partial/\partial x)(mV)$. Note that $\mathcal{L}$ depends entirely on the added mass per unit length m, and that there is no contribution due to circulatory forces. Typically, the added mass model is very simple, in that it is taken to be proportional to the area of the body cross-section. Then, instantaneously,

$$P = -\int_0^\ell \frac{\partial h}{\partial t}\mathcal{L}\,\mathrm{d}x, \quad E = -\int_0^\ell \left(\frac{\partial h}{\partial t} + U\frac{\partial h}{\partial x}\right)\mathcal{L}\,\mathrm{d}x, \quad T = \int_0^\ell \frac{\partial h}{\partial x}\mathcal{L}\,\mathrm{d}x, \quad (2.2a\text{–}c)$$

where ℓ is the body length, and E is evaluated as the rate of shedding of kinetic energy of lateral fluid motions into the fluid. The thrust T is found from the energy balance in (2.1), although it can be formally shown that T is the projection in the x-direction of the forces due to pressure differences acting on the body.

For a body in periodic motion with $m(x) = 0$ and $m(\ell) = m_\ell$, the time-averaged values are given by

$$\overline{P} = m_\ell U\left\{\overline{\frac{\partial h}{\partial t}\left(\frac{\partial h}{\partial t} + U\frac{\partial h}{\partial x}\right)}\right\}_\ell = m_\ell U\left[\overline{\frac{\partial h}{\partial t}V}\right]_\ell \quad (2.3)$$

and

$$\overline{E} = \frac{m_\ell}{2}U\left\{\overline{\left(\frac{\partial h}{\partial t} + U\frac{\partial h}{\partial x}\right)^2}\right\}_\ell = \frac{m_\ell}{2}U[\overline{V^2}]_\ell. \quad (2.4)$$

Then, from the energy balance given in (2.1),

$$\overline{T} = \frac{m_\ell}{2}\left\{\overline{\left(\frac{\partial h}{\partial t}\right)^2} - U^2\overline{\left(\frac{\partial h}{\partial x}\right)^2}\right\}_\ell . \tag{2.5}$$

We see that the mean thrust and power depend only on the conditions at the trailing edge where $x = \ell$. In addition, the lateral velocity of the tail, V, plays a crucial role in determining the performance.

Following Lighthill (1960) and Wu (1971*b*), we consider the special case of a distally propagating wave $g(x)\gamma(x - c_w t)$, where c_w is the wave velocity and the wave amplitude g depends on x ($|\gamma| = 1$). It will be assumed that such a motion can be made to satisfy the restrictions on the lateral and angular momenta embodied in the evaluation of the specific lift (the so-called 'recoil' constraint). Lighthill (1960) argues, on the basis of efficiency, that it is best to have $g_x(\ell) = 0$, and if this condition is satisfied then

$$\overline{T} = \tfrac{1}{2}m_\ell(1 - k_\lambda^{-2})g^2(\ell)\overline{(\mathrm{d}\gamma/\mathrm{d}t)^2_\ell}, \tag{2.6}$$

where $k_\lambda = c_w/U = f\lambda/U$. The thrust is therefore proportional to the mean square lateral velocity of the trailing edge, and for a given k_λ it is independent of U. Also, the travelling wave needs to move down the body at a speed greater than the swim velocity to achieve positive thrust; that is, T is only positive for $c_w > U$, the same conclusion reached by Taylor (1952) using resistive theory.

To find the steady swimming speed, we balance the thrust against the body drag. If it is assumed that the drag depends only on the body wetted area A_b so that $D_b = \rho U^2 A_b C_D/2$, where C_D is the drag coefficient, then

$$U^2 = \frac{m_\ell}{\rho A_b C_D}(1 - k_\lambda^{-2})g^2(\ell)\overline{(\mathrm{d}\gamma/\mathrm{d}t)^2_\ell}. \tag{2.7}$$

For a given body at a fixed value of k_λ, the swim speed is therefore proportional to the root-mean-square (r.m.s.) lateral velocity of the trailing edge. Furthermore, since the thrust only depends on the conditions at the trailing edge, it would be 'wasteful' (Lighthill's word) to keep $g(x)$ constant along the length of the body, and it is more desirable to let it increase from zero at the snout to its maximum at the tail.

Such observations follow from the model, which is entirely based on added mass considerations. Neglecting the circulatory force seems reasonable for long slender bodies because these forces tend to be important mostly near the leading edge. In this respect, the assumption that the lateral motion of the leading edge motion was zero is an important ingredient of the model; relaxing this assumption might also introduce a significant contribution from lift.

Finally, Lighthill considered how the angular and transverse momenta affected the thrust and efficiency, and concluded that minimizing the angular 'recoil' due to the body motion would be particularly desirable. This could be achieved by

confining the motions to the rear part of the fish where the fish mass is low, and by letting the waveform have both a positive and negative phase in the region of substantial motion amplitude. This accurately describes anguilliform motion. For example, Tytell & Lauder (2004) investigated the kinematics of a steadily swimming American eel and found that the motion of the body midline was described well by an exponentially growing travelling wave,

$$y(s) = ae^{[\alpha(s/\ell - 1)]} \sin[2\pi(s - c_w t)/\lambda], \tag{2.8}$$

where y is the lateral position of the midline, s is the coordinate following the midline, λ is the wavelength, a is the tail beat amplitude and α is the amplitude growth rate. Equation (2.8) also describes lamprey motion (Hultmark *et al.* 2007), and it appears to satisfy Lighthill's conditions for high thrust production and minimal recoil but not the condition for high efficiency, in that $y_s \neq 0$ at the tail.

The important role played by the lateral tail velocity in undulatory swimming was also confirmed by studying the thrust production of lampreys. Hultmark *et al.* (2007) used a robotic lamprey that was actuated to copy the lamprey motion described by (2.8). The near-wake structure for the lamprey robot and the American eel were shown in figure 4(*a*,*b*) and figure 6 gives the instantaneous vorticity fields generated by the robot at three phases in its motion. A band of positive vorticity is evident in the region near the body, confined to a relatively thin boundary layer rather than being shed and convected downstream. The undulatory motion of the robot generates alternating favourable and unfavourable pressure gradients along the body, seen in the streamwise varying strength of the near-surface vorticity, but there is no evidence of separation. The flow in the vicinity of the body, therefore, is unlikely to contribute little to either drag or thrust. As the tail moves to the right (figure 6*b*), the maximum strength of the near-surface vorticity increases, and as the tail changes direction the pressure gradients change sign and the region of vorticity becomes weaker, as seen in figure 6(*c*), indicating that a significant amount of vorticity has been shed into the wake. As might be expected, the tail motions and the vortices shed into the wake are closely correlated to the fluctuations in pressure on the body near the tail (Leftwich & Smits 2011).

To determine the contributions to the thrust, the momentum flux was integrated over the boundaries of a two-dimensional control volume containing the wake and parts of the tail. By varying the size of the box to include progressively more of the body, it was found that the region very close to the tail ($x/\ell \geqslant 0.99$) was responsible for the majority of the thrust production. For the region $0.99 \geqslant x/\ell \geqslant 0.9$ the thrust was essentially balanced by the drag, and at locations upstream of $x/\ell = 0.9$ the drag was found to be greater than the thrust. The dominant role of the tail in producing thrust is in complete accordance with slender body theory. In addition, Leftwich & Smits (2011) found that the net mean thrust produced by their lamprey robot at $St = 0.53$ was only approximately 20 % less than that given by (2.5). That would

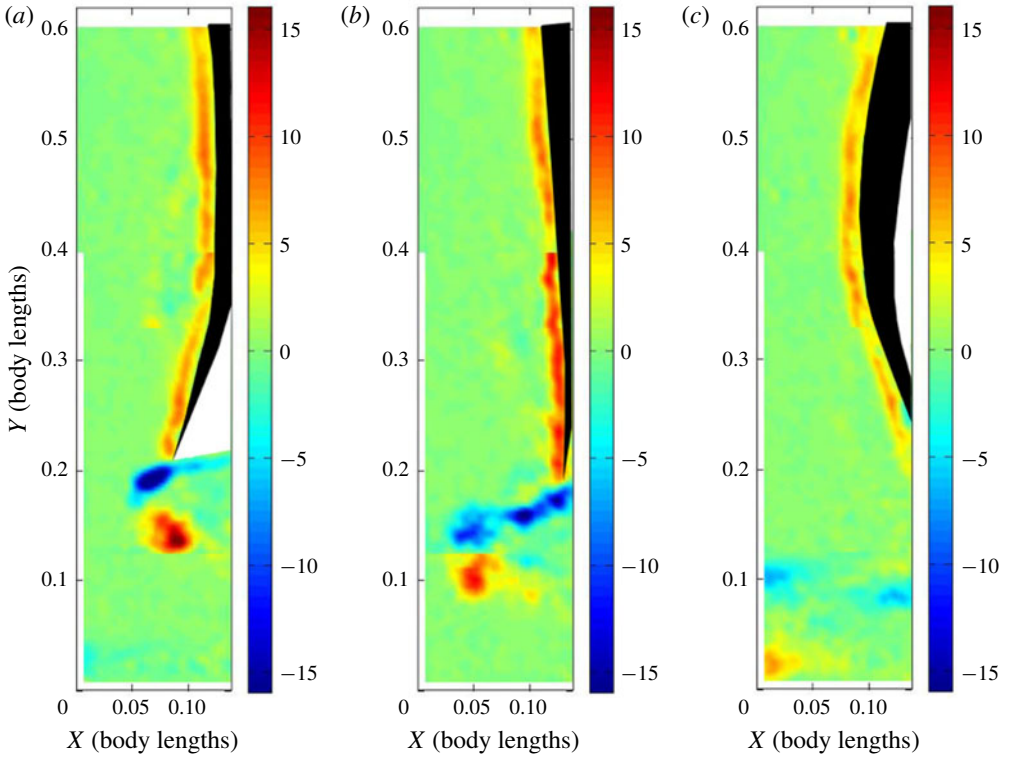

FIGURE 6. Phase-averaged out-of-plane vorticity fields along the body and in the wake for a steadily swimming robot. The flow is from top to bottom, and the body of the robot is indicated by the black shape. Reproduction with permission from Hultmark *et al.* (2007).

imply a drag coefficient for the robot of about 0.08, which seems like a reasonable value.

2.2. *Flexible panels in undulatory motion*

Slender body theory gives estimates for the forces acting on the body and the surrounding fluid under a prescribed motion. It does not generally consider the mechanical response of the body itself, although Wu (1971*b*) considered the internal forces generated by an elastic membrane in prescribed motion in terms of the attendant recoil. In fish, the amplitude and wavelength of their undulation can generally be controlled by muscle action. In laboratory studies of undulatory motion, this sort of active control is rarely imitated (for an exception, see Clark & Smits 2006). Instead, experiments typically rely on a predetermined motion input (such as heave or pitch) and allow the flexibility of the foil, membrane or body to determine its response. Computations generally go further, and prescribe the full motion, typically determined directly from animal studies, without accounting for any fluid–structure interaction.

To understand the effects of flexibility and the mechanical response of the body more generally, Quinn, Lauder & Smits (2014) examined the behaviour of flexible, rectangular panels, actuated in heave at their leading edge with an amplitude a'. For small deflections h of a flexible panel with constant thickness δ and span s, the panel response can be modelled by the Euler–Bernoulli beam equation,

$$\rho_p s\delta \frac{\partial^2 h}{\partial t^2} + EI\frac{\partial^4 h}{\partial x^4} = F_{ext}, \tag{2.9}$$

where ρ_p is the density of the panel, E is the elastic modulus, I is the area moment of inertia and F_{ext} is the external force per unit length (Allen & Smits 2001). Since $\rho_p/\rho = O(1)$ and $\delta/c \ll 1$, the added mass forces are expected to dominate over the inertia of the panel, and so the mass per length of the panel, $\rho_p s\delta$, is replaced with an effective (added) mass per length, ρsc, which is assumed constant along the chord. For long, narrow panels ($\mathcal{AR} \ll 1$), the added mass per unit length will vary as ρs^2, and for short, wide panels ($\mathcal{AR} \gg 1$) it varies as ρcs. For panels with $\mathcal{AR}$ of $O(1)$, the appropriate added mass term is less clear. Quinn *et al.* used panels with $\mathcal{AR} = 0.77$, so their choice of ρsc is somewhat arbitrary but since the aspect ratio was fixed it does not affect any of their conclusions (see also Allen & Smits 2001; Thiria & Godoy-Diana 2010; Dewey *et al.* 2013; Ramananarivo, Godoy-Diana & Thiria 2013). This issue is addressed in more detail in § 3.6.

Introducing the dimensionless variables $x^* \equiv x/c$, $h^* \equiv h/a$, and $t^* \equiv tf$, where a is (as usual) the amplitude of the trailing edge motion, gives

$$\Pi_1^2 \frac{\partial^2 h^*}{\partial t^{*2}} + \frac{\partial^4 h^*}{\partial x^{*4}} = F'_{ext}, \tag{2.10}$$

where $F'_{ext} \equiv F_{ext}\, c^4/(EIa)$ is the dimensionless external force per unit length, except for added mass, which is now incorporated into the left-hand side as the effective mass per length. These external forces could include, for example, circulatory forces and internal damping or viscous drag. Here,

$$\Pi_1 = f\sqrt{\rho sc^5/(EI)}\ \ (= f/\hat{f}_1 = f^*), \tag{2.11}$$

and it is the ratio of added mass forces to internal bending forces, called the effective flexibility. We also recognize it as a non-dimensional frequency f^*, that is, the ratio of the driving frequency to the first resonant frequency of the panel when added mass forces are considered.

The effect of resonances for pitching foils was examined with a more exact, though two-dimensional fluid dynamical model by Alben (2008), who found that the resonances were distributed as integers to the $-5/2$ power, and the input power and thrust power were proportional to the parameter $R_2 = \Pi_1'$ at the resonances. The Froude efficiency tended to 1 at small thrust power (when many wavelengths are present on the body), then dropped to a fixed fraction at large thrust power. No peaks were seen in the efficiency, as was also found by Floryan & Rowley

Panel	D	C	P_1	P_2	P_3	P_4	P_5	B	P_6	A	P_∞
$EI \times 10^3$ N m^{-2}	0.069	0.81	0.54	1.3	2.5	3.6	7.2	11	14	320	18 000
$\delta/c \times 10^3$	0.6	1.6	1.1	1.6	2.1	3.2	4.2	3.9	5.3	3.4	26.5
Π_1'	—	—	0.3	0.7	1.4	2.0	4.0	—	7.8	—	$O(10^4)$

TABLE 1. Panel physical properties. Panels A to D from Quinn *et al.* (2014); Panels P_1 to P_∞ from Dewey *et al.* (2013). Here, $\Pi_1' = k^2/\Pi_1$ (see (3.19)). The effective stiffness for fish is likely in the range $1.4 < \Pi_1' < 4$ (panels P_3 to P_5).

(2018). Alben *et al.* (2012) later studied (theoretically and experimentally) a freely swimming flexible foil in heave, and observed that the scaling of swimming speed with bending modulus and foil length was given as power laws at resonant peaks (separate power laws in terms of dimensional and dimensionless parameters).

Quinn *et al.* (2014) conducted experiments on four panels with bending stiffnesses ranging from $EI = 320 \times 10^{-3}$ (Panel A, rigid) to 0.069×10^{-3} N m^{-2} (Panel D, the most flexible), as listed in table 1. The modal contributions to the panel undulatory motion were expressed in terms of the eigenfunctions for the homogenous form of (2.10), that is, where $F'_{ext} = 0$. The natural frequencies of these modes, $\hat{f}_i$, are such that $f/\hat{f}_i = \Pi_1 \lambda_i^2$, where λ_i is the corresponding wavelength. Flexibility essentially adds resonances to the system. The two most rigid panels displayed only the first mode, while the most flexible panel exhibited the first four modes. As the heaving frequency of the more flexible panels increased, the modal contributions passed through a series of peaks as successively higher modes were activated, and with increasing flow speed these peaks shifted to higher frequencies. Resonance occurred at certain driving frequencies where the trailing edge amplitude was locally maximized, and Quinn *et al.* (2014) found that the frequency at which this resonance occurs was a strong function of f^*, but relatively independent of flow speed (for a factor of 5 variation).

From slender body theory, we know that the conditions at the trailing edge are paramount. For flexible panels, the trailing edge amplitude a is an output of the system since it depends on the panel response to the input a'. The amplitudes of the resonant peaks in a/a' decrease with increasing flexibility as the deflections are more easily suppressed by fluid forces when the panel is more flexible. They also decrease with increasing flow speed as the form drag at higher flow speeds suppresses panel deflections and thereby reduces the amplitude of the wave along the panel. It appears that the first-order effect of form and viscous drag is to stretch the shape of the panel in the streamwise direction but leave the resonant frequencies relatively unaffected.

The time-averaged thrust behaviour is shown in figure 7. In general, $\overline{T}$ increases with heaving frequency, but it does so at different rates, and in some ranges even decreases with frequency. The resulting plateaus are directly related to resonance at the trailing edge. Since the more flexible panels pass through multiple resonant

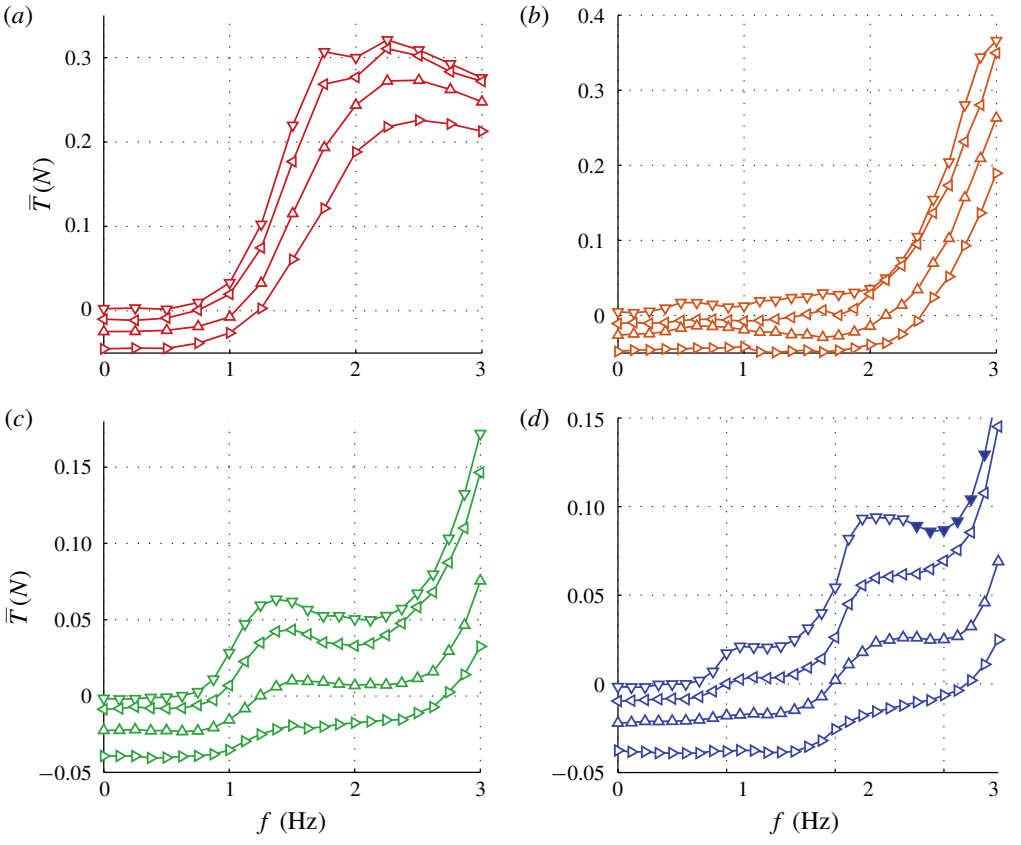

FIGURE 7. Time-averaged thrust. (a,b,c,d) $\triangledown$, $u_\infty = 40$ mm s^{-1}; $\triangleleft$, $u_\infty = 110$ mm s^{-1}; $\triangle$, $u_\infty = 170$ mm s^{-1}; $\triangleright$, $u_\infty = 240$ mm s^{-1}. Adapted with permission from Quinn *et al.* (2014).

frequencies, they exhibit multiple plateaus (for (b) the first resonance is close to 1 Hz, and the second resonance occurs beyond 3 Hz).

Higher flow speeds reduce $\overline{T}$ in two main ways. One way is by shifting the curves downward due to viscous drag producing an offset between them (see also § 3.1). At higher frequencies, the curves differ by more than just an offset, especially for the more flexible panels. This trend suggests that variations beyond the simple offset are due to the different kinematics brought on by higher flow speeds. A similar behaviour was seen by Floryan & Rowley (2018) who analysed the response of two-dimensional, flexible panels in heave and pitch. When the flow speed increases, circulatory forces start to become important, the natural frequencies of the system begin to shift away from their quiescent behaviour, and the eigenvalues become more damped.

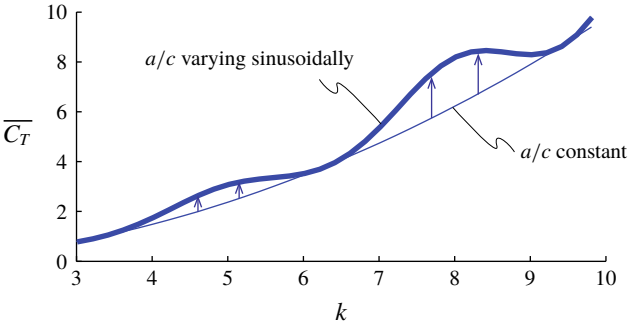

FIGURE 8. Predictions of the Lighthill model for a sinusoidal propulsor. Thin line: $a/c = 0.1$; thick line: $a/c = 0.1(1 + 0.15\sin^2 k)$. Adapted with permission from Quinn *et al.* (2014).

Quinn *et al.* (2014) used slender body theory to help understand the formation of the plateaus in thrust. From (2.5) we can write

$$\overline{C_T} \equiv \frac{\overline{T}}{\frac{1}{2}\rho U^2 sc} = \frac{m_\ell}{\rho sc}\left(\frac{a}{c}\right)^2 \left[k^2\overline{\left(\frac{\partial h^*}{\partial t^*}\right)^2} - \overline{\left(\frac{\partial h^*}{\partial x^*}\right)^2}\right]_{x^*=1}. \tag{2.12}$$

Consider a panel experiencing a sinusoidal travelling wave with a wavelength equal to the chord, that is, $h^* = \sin(2\pi(x^* + t^*))$. Figure 8 plots the predicted variation of the thrust coefficient for the case where a/c is constant, and for the case where a/c varies sinusoidally with the reduced frequency k. The local maxima in the trailing edge amplitude increase the net thrust coefficient such that plateaus appear in the k–$\overline{C_T}$ curve. In addition, if the heaving panel were perfectly rigid ($EI \to \infty$), h^* would have no spatial variation. For finite rigidities, however, h^* varies with x^*, and (2.12) predicts that this spatial variation will reduce $\overline{C_T}$, which is consistent with the data shown in figure 7.

The efficiency can be quantified for thrust-producing conditions ($\overline{T} > 0$) where the propulsor is accelerating or overcoming the drag on a body to which it is attached. Following Dewey *et al.* (2013), the results for the flexible propulsors with $\overline{T} > 0$ are shown in figure 9 as $\hat{\eta} = \eta St$ (this scaling will be addressed further in § 3.6). Peaks in $\hat{\eta}$ occur at or just above the f^* values where the trailing edge amplitude was maximal. The efficiency is maximized at low speeds and high flexibilities. At high flow speeds, flow visualizations indicated the presence of flow separation on the membrane itself, undoubtedly resulting in significantly higher drag and lower efficiency.

Since the value of the Strouhal number in the vicinity of the peaks varies from approximately 0.5 to 1, it is evident from figure 9 that the corresponding values of the efficiency η for a flexible heaving panel are quite low. In a later study focusing on panel D (see table 1), Quinn, Lauder & Smits (2015) found that adding

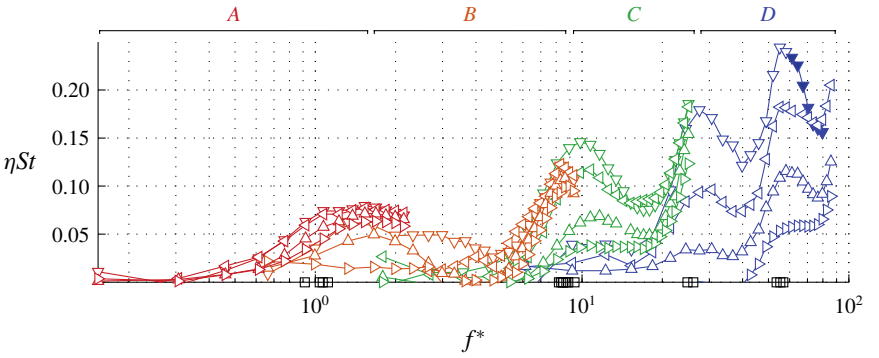

FIGURE 9. Efficiency peaks of heaving flexible panels at multiple resonance modes. Panels *A*, *B*, *C* and *D* have stiffnesses $EI = 3.2 \times 10^{-1}$, 1.1×10^{-2}, 8.1×10^{-4}, 6.9×10^{-5}, and are coloured red, orange, green and blue respectively. Adapted with permission from Quinn *et al.* (2014).

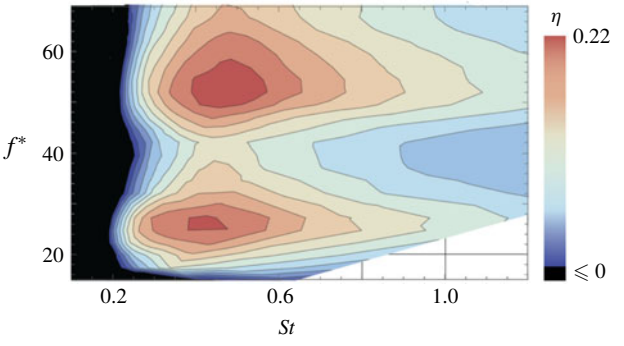

FIGURE 10. Contour plot of propulsive efficiency, heave only motions, $a'/c = 0.07$. Adapted with permission from Quinn *et al.* (2015).

a pitching motion enhanced the efficiency considerably. Although the net thrust and power scaled as expected with the frequency and amplitude of the leading edge, the efficiency showed a complex multimodal response. For heave only motions, two optimal conditions were found, one with $\eta = 0.23$ at $St = 0.53$, and one with $\eta = 0.21$ at $St = 0.40$, as illustrated in figure 10. For pitch and heave motions combined, two optimal conditions were also found, one for $St = 0.26$, $\eta = 0.38$, and the other for $St = 0.33$, $\eta = 0.37$, so the addition of pitch increased the efficiency by a factor of approximately 1.7. The conditions correspond almost exactly to a doubling of the parameter $\Pi_1 = f^*$, that is, the non-dimensional frequency describing the resonant modes.

In this respect, Floryan & Rowley (2018) showed that linear inviscid theory predicts that local resonant maxima in thrust and power appear, but it does not predict any local resonant maxima in efficiency, whereas such efficiency peaks are

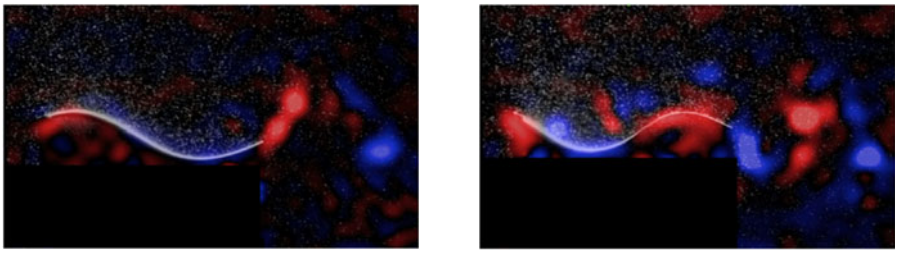

FIGURE 11. Phase-averaged spanwise vorticity (red is positive, blue is negative). (*a*) First optimum, $St = 0.26$, $f^* = 24.8$, $a'/c = 0.07$, $\alpha = 30°$, $\phi = 76°$, $\eta = 0.38$. (*b*) Second optimum, $St = 0.33$, $f^* = 50.8$, $a'/c = 0.07$, $\alpha = 30°$, $\phi = 96°$, $\eta = 0.37$. Adapted with permission from Quinn *et al.* (2015).

clearly observed in experiments. Therefore, the resonant peaks in efficiency are due to either finite Reynolds number effects, nonlinear effects, or both. Floryan & Rowley (2018) found that the presence of drag will always create resonant peaks in efficiency, while Ramananarivo, Godoy-Diana & Thiria (2011) showed that nonlinearities can create non-resonant peaks in efficiency for flexible flapping wings.

Figure 11 shows the phase-averaged vorticity plots corresponding to the two optima for heave and pitch combined. Although the efficiencies are almost the same, they occur at two different mode shapes, and generate very different wakes; whereas the first optimum resembles a 2S (reverse von Kármán street) structure, the second optimum is more a 2P structure. For simple flexible panels, therefore, efficient swimming can be achieved for (at least) two different wake structures.

In general, Quinn *et al.* (2015) concluded that efficiency is globally optimized when (i) the Strouhal number is high enough that the flow does not separate over the peaks and troughs in the panel waveform, but low enough that the vortex cores in the wake remain tightly packed and coherent; (ii) the panel is actuated at a resonant frequency of the fluid–panel system; (iii) heave amplitude is tuned such that trailing edge amplitude is maximized while the flow along the body remains attached; and (iv) the maximum pitch angle and phase lag are chosen so that the effective angle of attack is minimized.

We now turn to oscillatory swimming.

3. Oscillatory Swimming

For fast, efficient swimming in sustained cruise, the prototypical animal is the tuna (Webb 1984). The tuna has a streamlined (fusiform) shape that is deepest about halfway between the head and the tail (see figure 12), and its particular swimming motion is called thunniform, as described earlier. As pointed out by Lighthill (1969), the body morphology also helps to minimize recoil. For anguilliform swimmers, the unsteady side forces and yawing moments tend to cancel because they have at

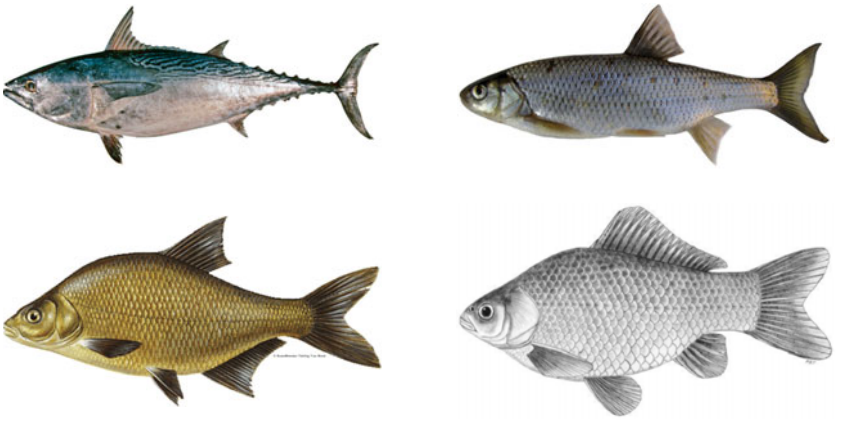

FIGURE 12. Clockwise from top left: Kawakawa (*Euthynnus affinis*, or mackerel tuna, License: by Attribution-Noncommercial Australian National Fish Collection, CSIRO); Dace (*Leuciscus leuciscus*, reproduced by attribution from http://www.fishinginireland.info/index.htm); Bream (*Abramis brama*, reproduced with permission from www.sommen.nu); Goldfish (*Carassius auratus*, reproduced by attribution from https://archive.usgs.gov/archive/sites/fl.biology.usgs.gov/Carp_ID/html/carassius_auratus.html).

least one wavelength present along their body length. Carangiform and thunniform swimmers do not, but the recoil motions are minimized by having a deep anterior body and a narrowing posterior.

Because the posterior part tapers down to a narrow peduncle, and the caudal fin planform area is relatively large by comparison, it is expected that most of the thrust production is due to the caudal fin motion, and that the contribution by the body motion is secondary. Bainbridge (1963) analysed the swimming performance of dace, bream and goldfish, and estimated that the contribution of the caudal fin to the total thrust varied from a value of 45 % for the bream, to 65 % for the goldfish, to 84 % for the dace. He also quotes Gray (1933), who estimated 40 % for the whiting (*Gadus merlangu*). We will show that these estimates are probably low (see § 3.10), and so a useful approximation for the purposes of modelling is to assume that all of the thrust is provided by the motion of the caudal fin (or fluke, as the case may be), and, by extension, that the body is the principal (but not the only) source of drag.

We therefore focus on the hydrodynamic performance of the caudal fin. In essence, it describes a combination of heaving and pitching, naively described by sinusoidal motions at a common frequency, so that

$$h = h_0 \sin(2\pi ft), \quad \theta = \theta_0 \sin(2\pi ft + \phi), \tag{3.1a,b}$$

where h_0 is the heave amplitude, θ_0 is the pitch amplitude and ϕ is the phase difference between pitch and heave. For reference, figure 16 illustrates the motion of a swimming foil for phase differences $\phi = 0°, 90°, 180°$ and $270°$.

We now describe some simple models for thrust and efficiency of heaving and pitching foils, based on experiments and analytical considerations. We mainly consider rectangular foils as an abstraction of a caudal fin, but some aspects of the fin planform shape including the aspect ratio and the shape of the trailing edge will also be discussed. The coefficients of thrust and power are given by

$$C_T = \frac{F_x}{\frac{1}{2}\rho U^2 A}, \quad C_P = \frac{F_y \dot{h} + M\dot{\theta}}{\frac{1}{2}\rho U^3 A}, \tag{3.2a,b}$$

where F_x is time-averaged thrust in the streamwise direction produced by the foil motion, F_y is the force perpendicular to the free-stream direction and M is the moment taken about the leading edge of the foil.

3.1. *Pitching foils*

We begin with a simple example that captures some of the salient characteristics of oscillatory propulsion. Consider a two-dimensional NACA0012 airfoil pitching about its quarter chord in a uniform stream of speed U so that its pitch angle θ varies as $\theta_0 \sin(2\pi ft)$. There is no heaving motion. The results for the thrust, power and efficiency shown in figure 13 were computed using the direct numerical simulations (DNS) method described by Sentürk & Smits (2018) and Sentürk *et al.* (2019). The Reynolds number was varied from 500 to 32 000. To put that range into perspective, consider a fish with a caudal fin that has a chord length 10 % of its overall length. A chord Reynolds number of 500 would then correspond to a fish of length 70 mm, swimming at about one body length per second, which is a typical speed for the kind of fish we are interested in. Similarly, a chord Reynolds number of 32 000 would correspond to a fish of length 560 mm, also swimming at one body length per second. The corresponding fluke Reynolds numbers for dolphins can reach 10^6, with a body length Reynolds number of 10^7, and the corresponding numbers for whales could be 10 times higher.

We first note that the mean thrust and power coefficients increase nonlinearly with Strouhal number. The thrust varies approximately as St^2, and power varies approximately as St^3 (the actual scaling is considered in § 3.3). Second, we see that the thrust coefficient and the efficiency display a strong Reynolds number dependence. Third, the thrust coefficient has a negative offset at small values of the Strouhal number, which corresponds to the drag offset at very low Strouhal number (quasi-steady flow), averaged over a pitching cycle. This offset is similar to that seen by Quinn *et al.* (2014) for a flexible pitching panel in heave (see figure 7). Fourth, the efficiency tends to negative values at low Strouhal number (corresponding to a negative thrust coefficient), rising quickly as the Strouhal number increases, before falling more slowly at higher Strouhal numbers. The curves display a maximum value of efficiency η_m at a particular Strouhal number St^*, where both η_m and St^* depend strongly on Reynolds number; increasing the Reynolds number tends to

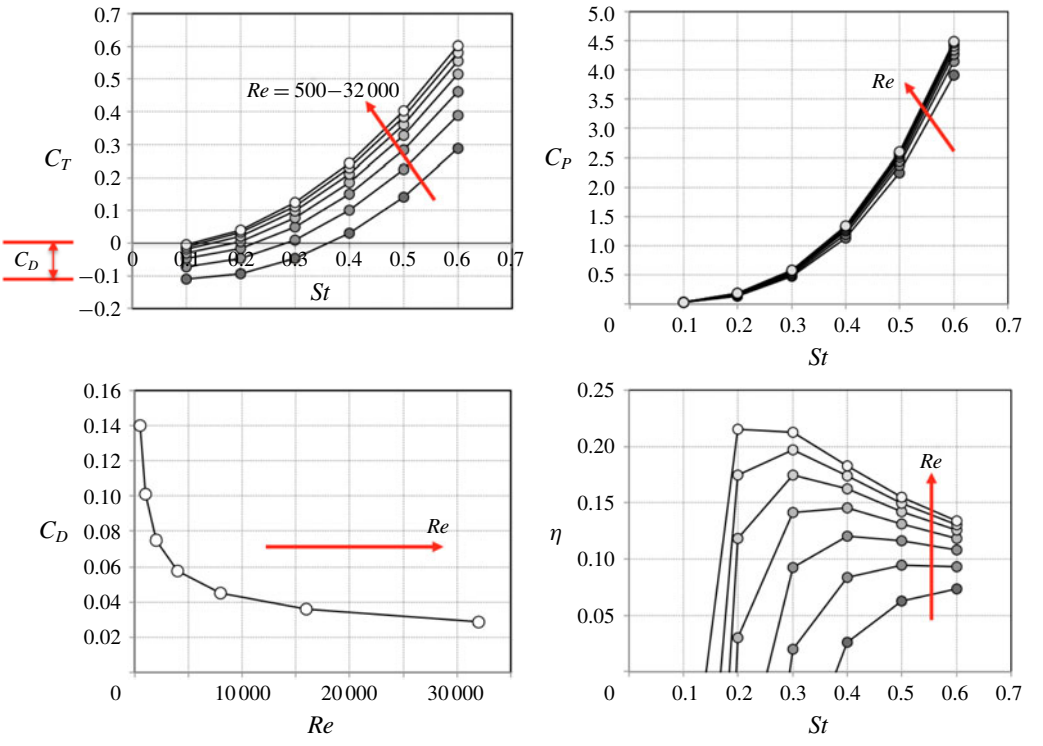

FIGURE 13. NACA0012 foil pitching about quarter chord from the leading edge ($\theta_0 = 8°$). DNS by Sentürk & Smits (2019). All data averaged over one pitching cycle. Adapted with permission from Sentürk & Smits (2019).

increase the efficiency at all Strouhal numbers, while also notably increasing the maximum efficiency. Similar peaks in efficiency were seen for flexible panels in undulatory motion (figure 10).

These DNS results are in broad agreement with the experiments of Buchholz & Smits (2008) on rigid rectangular panels pitching about their leading edge. Buchholz *et al.* found that decreasing the aspect ratio of the panel monotonically decreased the thrust coefficient, while the efficiency was largely unaffected except for the smallest aspect ratio ($\mathcal{AR} = s/c = 0.54$) where it decreased somewhat. As to the effects of Reynolds number, their measurements were conducted over two Reynolds number ranges with average values of approximately 10 000 and 21 000. Small differences in the thrust and efficiency were observed, but conclusive trends were difficult to discern, which is perhaps not surprising given the results shown in figure 13, where C_D is seen to vary slowly for Reynolds numbers larger than approximately 10 000, and its effects on thrust and efficiency are also seen to diminish.

It is important to note that the drag coefficient for a given foil depends on its profile shape as well as its Reynolds number. Maximizing thrust and efficiency at a given Reynolds number therefore poses an optimization problem to find the foil

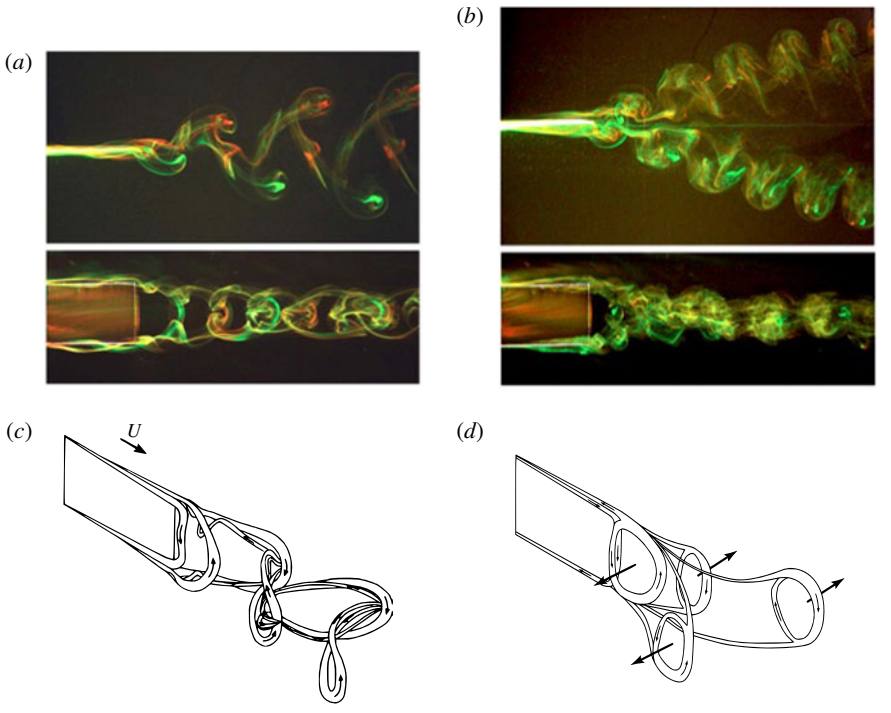

FIGURE 14. (*a*,*b*) Dye flow visualizations. Flow is from left to right. (*c*,*d*) Vortex skeleton models of the wake for $\mathcal{AR} = 0.54$, $A/s = 0.31$ and $Re_c = 640$. (*a*,*c*) $St = 0.23$; (*b*,*d*) $St = 0.43$. Adapted with permission from Buchholz & Smits (2005, 2006).

shape with the lowest drag coefficient for a given motion profile (Van Buren *et al.* 2019*b*) (see also § 3.4).

In addition to considering the thrust and efficiency, Buchholz & Smits (2005, 2006) visualized the wake using different colour dyes, and suggested vortex skeleton models for the wake structure (see figure 14). For these low Reynolds number wakes ($Re_c = 640$), three distinct and highly three-dimensional wake structures were observed as the Strouhal number was varied. For approximately $0.20 < St < 0.25$, two horseshoe vortices were shed per pitching cycle, which interacted with neighbouring structures to form a three-dimensional chain of vortex loops. When viewed along the spanwise axis, the wake resembles a transversely growing von Kármán vortex street. Two critical attributes are that the streamwise legs of the structures increase in strength (circulation) toward the trailing edge, as well as changing in strength with the phase of the motion. This influences the dynamics of the wake in that the interaction between horseshoes is dominated by the most recently created structure. It also implies the existence of spanwise vorticity bridging the legs which is a salient feature of the wakes observed at higher Strouhal numbers and is consistent with the dynamic stall vortex shed by other unsteady propulsors. For all wakes, there

is a strong compression of the wake in the spanwise direction, and an expansion in the plane of the motion.

For approximately $St > 0.25$, the wake bifurcates into two oblique trains of vortex structures. At $St = 0.43$, the individual structures are topologically similar to the structures observed at $St = 0.23$ except that a portion of the spanwise shear layer found at $St = 0.23$ is shed from the trailing edge as a discrete spanwise vortex. The resulting fundamental structure is therefore a vortex ring that is partly entrained into the tip of a horseshoe vortex. These vortex rings move away from the centreline under their own induced velocity, and the wake is seen to bifurcate. At $St = 0.64$ (not shown here), the wake contains an additional feature in which streamwise vortices undergo a perturbation near the trailing edge of the panel which leads to the generation of hairpin or horseshoe vortices that convect outward in the spanwise direction. This transition from a kind of 2S structure to a 2P structure with increasing Strouhal number is very similar to that seen in other cases, such as pitching and heaving plates (Guglielmini 2004; Dong *et al.* 2005).

The wake structure was found to depend on the Reynolds number, although a similar global wake behaviour was observed at moderate Reynolds numbers of $O(10^4)$. Of course, the effects of Strouhal number and Reynolds number are intertwined, as made clear by the results shown in figure 13 for the NACA0012 airfoil. That is, at a given Strouhal number (for example, 0.3), the efficiency at low Reynolds number is negative, meaning the drag is larger than the thrust, whereas at higher Reynolds numbers the efficiency is positive because the thrust is larger than the drag. In this regard, the orientation of the vortices in the plane of motion for $St = 0.23$ in figure 14 suggests that for this panel at this Strouhal number and this Reynolds number the wake is drag producing. Increasing the Reynolds number will reduce the drag, lead to a net positive thrust, and a re-orientation of the vortices.

3.2. *Heaving and pitching foils*

The results shown in figure 13 also demonstrate that the peak efficiency for this particular pitching foil does not exceed about 25 %, even at the largest Reynolds number considered. Adding a heave motion, with an appropriate phase difference can improve this result substantially. For example, figure 15 displays the time-averaged thrust coefficient and efficiency of a pitching foil with incremental increases in heave amplitude while keeping the pitch amplitude fixed at $\theta_0 = 15°$. Similar increases in thrust and efficiency for undulatory swimming were seen in the case of a flexible plate, where adding pitch to heave increased the optimal efficiency by a factor of about 1.7 (see figure 10). For the rigid foil shown in figure 15 the efficiency curves also exhibit a clear maximum value, suggesting that an optimum efficiency exists for any heave/pitch combination. For reduced frequencies below the optimum, the efficiency decreases sharply as the effects of the viscous drag on the propulsor become important.

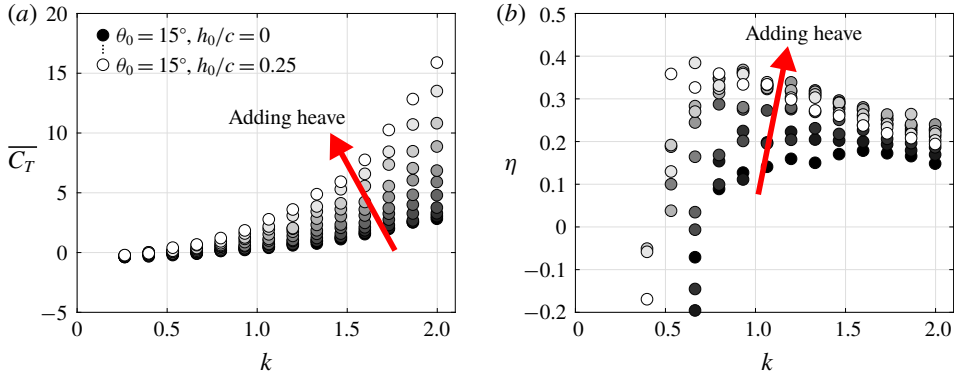

FIGURE 15. Pitching foil with incremental increases in heave amplitude for $\phi = 270°$ ($f^* = k$). (*a*) Thrust coefficient; (*b*) efficiency. Reproduction with permission from Van Buren, Floryan & Smits (2018*a*).

When combining sinusoidal heaving and pitching motions the phase offset is a critical parameter. Figure 16 illustrates the motion of a swimming foil for phase differences $\phi = 0°, 90°, 180°$ and $270°$. When heave and pitch are in phase ($\phi = 0$), the motion appears to an observer moving with the foil as if the foil is pitching about some point upstream of the leading edge. For phase angles around $\phi = 90°$, the trailing edge leads the leading edge, and when $\phi = 180°$ the foil appears to pitch about a point behind the leading edge. For $\phi = 270°$ the motion seems to be the most 'fish-like', cleanly slicing through the water with the lowest angles of attack (the angle between the foil and its instantaneous direction of motion). This case is further illustrated in figure 17. Compared to heave-only motions, greater heave velocities can be achieved for the same angle of attack by adding the appropriate pitch. The increased heave velocity increases the thrust component and rotates more of the lift vector in the thrust direction, increasing the efficiency. As a useful measure of the relative magnitudes of pitching and heaving, Lighthill (1969, 1970) introduced the proportional-feathering parameter, Θ defined so that $\alpha_m = \Theta V/U$, where α_m is the maximum angle of attack. Therefore Θ is a parameter that measures the reduction in the instantaneous angle of attack from its maximum value, and decreasing Θ tends to increase thrust while decreasing the efficiency.

The performance of submerged foils in combined heaving and pitching motion has been studied relatively extensively (Lighthill 1970; Dickinson 1996; Sfakiotakis *et al.* 1999; Triantafyllou *et al.* 2000; Von Ellenrieder, Parker & Soria 2003). In a particularly influential work, Anderson *et al.* (1998) obtained efficiencies as high as 87 % using a heaving and pitching two-dimensional NACA0012 airfoil in sinusoidal motion. They connected the wake structure to the performance of the foil, arguing that for maximum efficiency the leading edge vortex pair needs to interact beneficially with the trailing edge vorticity. The flow visualization was performed

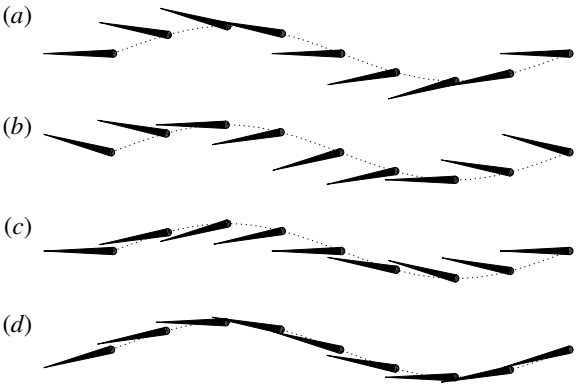

FIGURE 16. Motion of a foil swimming from left to right via heave and pitch motions with a phase offset (*a*) $\phi = 0°$, (*b*) 90°, (*c*) 180° and (*d*) 270°. In this example, $h_0/c = 0.375$, $\theta_0 = 15°$ and $f^* = 0.16$. Reproduction with permission from Van Buren *et al.* (2018*a*).

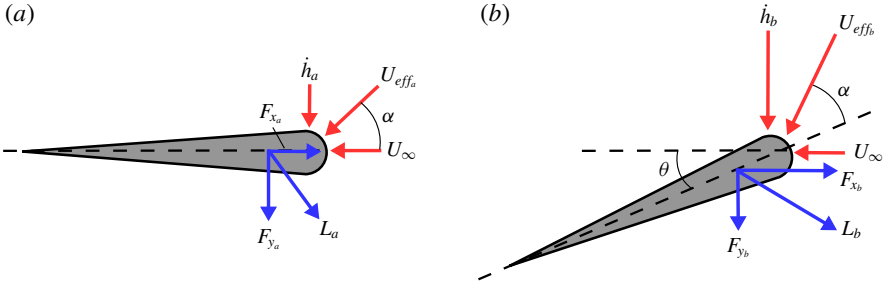

FIGURE 17. Heaving foil at the same instantaneous angle of attack (*a*) without and (*b*) with added pitch motion ($\phi = 270°$). Streamwise, heave and effective velocities shown in red, resulting lift-based forces shown in blue. Reproduction with permission from Van Buren *et al.* (2018*a*).

at $Re = 1000$, whereas their force measurements were at $Re = 40\,000$. Subsequent research suggests that it is necessary to avoid leading edge vortices altogether in order to maximize efficiency (Tuncer & Kaya 2005; Young *et al.* 2006; Young & Lai 2007). In related work, Read, Hover & Triantafyllou (2003) recognized the importance of the peak angle of attack when considering performance, although they reported lower values of efficiency (55 %–70 %) than the 87 % reported by Anderson *et al.* (1998) in the same laboratory under similar experimental conditions. We take that to indicate the crucial role played by drag in determining the efficiency, as we will see. Experiments on large amplitude motions by Scherer (1968) showed similar peak efficiency values to those found by Read *et al.* (2003), over a wide range of parameters. We now present some simple models for the thrust production,

power expenditure, and efficiency of heaving and pitching foils, to help explain these trends.

3.3. *Analysis of heaving or pitching foils*

The analysis of heaving and pitching plates and foils has a distinguished history, dating back to Theodorsen (1935), who first derived the linearized expressions for the forces generated by an oscillating foil in the context of aerodynamic flutter. His analysis included the contributions due to circulatory and added mass forces, and Garrick (1936) used his results to develop expressions for thrust and power for a two-dimensional, rigid propulsor. We now follow Floryan *et al.* (2017*a*), Floryan, Van Buren & Smits (2018) and Van Buren *et al.* (2018*a*) to consider a foil moving in heave and pitch as a simplified model of an isolated propulsor. The unsteady lift model of Theodorsen (1935) will be combined with the added mass force model by Sedov (1965) to construct scaling relations for the thrust and efficiency. The added mass model given by Sedov (1965) is preferred to that given by Theodorsen (1935) because Sedov's model includes both the normal and tangential contributions. In this section, we examine either heaving or pitching foils in sinusoidal motion, as described by (3.1). Combined motions are studied in the following section.

The only circulatory (lift-based) forces considered are those that arise when the foil is at an instantaneous angle of attack to the free stream given by α. The effective flow velocity seen by the foil has a magnitude $U_{eff} = \sqrt{U^2 + \dot{h}^2}$, and an angle relative to the free-stream velocity of $\arctan(\dot{h}/U)$, so that $\alpha = \theta - \arctan(\dot{h}/U)$ (notation as given in figure 18). Hence, for a foil of chord c and span s,

$$F_x = -L\sin(\theta - \alpha) = -L\dot{h}/U_{eff}, \tag{3.3}$$

$$F_y = L\cos(\theta - \alpha) = LU_\infty/U_{eff}. \tag{3.4}$$

Here, F_x is the thrust, F_y is the lateral force, L is the lift on the foil given by $L = (1/2)\rho U_{eff}^2 scC_L$ and the lift coefficient $C_L = 2\pi\sin\alpha + (3/2)\pi\dot{\alpha}c/U$ (Theodorsen 1935). The moment about the leading edge is $M = -cL/4$. The wake correction term due to downwash (Theodorsen's lift deficiency factor) is neglected as it is approximately constant under the conditions considered here.

Floryan *et al.* (2017*a*) combined circulatory and added mass-based contributions to the thrust and power for pitching or heaving foils. They showed that. the mean thrust generated by heaving motions is entirely lift-based (see figure 18), whereas mean thrust generated by pitching motions is from added mass alone. However, for both heave and pitch motions, the mean input power (and thus efficiency) depends on lift-based and added mass forces. In contrast, slender body theory, and the analysis of undulatory motions in general, assumes that the only forces acting are those due to added mass.

We can anticipate some later results by first doing a simple scaling analysis (see also Dewey *et al.* 2013, Quinn *et al.* 2015). We expect that the thrust generated by

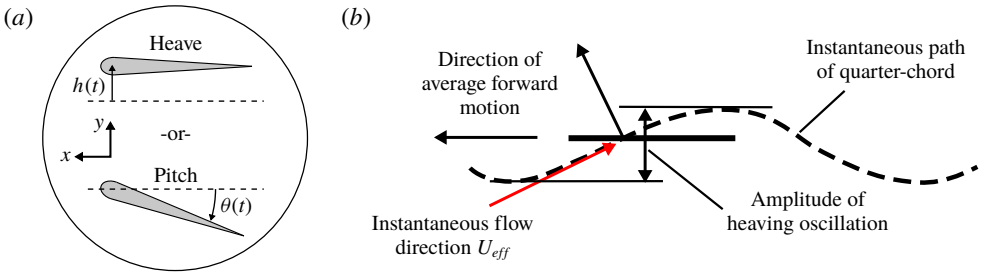

FIGURE 18. (*a*) Notation. (*b*) Lift-based thrust generation for a foil in pure heave. Adapted from the original shown in Katz & Plotkin (2001).

a purely pitching motion will scale as the component in the streamwise direction of the added mass ($\sim\rho c^2 s$ for two-dimensional panels, that is, $\mathcal{AR} \gg 1$) times the acceleration ($\sim c\ddot{\theta}$). Hence,

$$F_x \sim \rho s c^3 \ddot{\theta}\theta, \tag{3.5}$$

so that the mean thrust scales as

$$\overline{F}_x \sim \rho s c^3 f^2 \theta_0^2 \approx \rho s c V^2, \tag{3.6}$$

where V is the amplitude of the trailing edge velocity.

For a purely heaving motion, the thrust is expected to scale as the component in the streamwise direction of the instantaneous lift force. That is, from (3.4),

$$F_x \sim L(\dot{h}/U_{eff}). \tag{3.7}$$

If we assume that the contribution to the lift is quasi-steady, and that for small angles of attack $\alpha \approx \dot{h}/U_{eff}$, then

$$F_x \sim \tfrac{1}{2}\rho U_{eff}^2 s c\,(2\pi\alpha)(\dot{h}/U_{eff}) \sim \pi\rho s c\,\dot{h}^2, \tag{3.8}$$

so that the mean thrust scales as

$$\overline{F}_x \sim \rho s c f^2 h_0^2 \approx \rho s c V^2. \tag{3.9}$$

We see that for both pitch and heave, to this level of approximation, the time-averaged thrust depends on the velocity of the trailing edge, and it is independent of the flow velocity. The experimental results given by Van Buren *et al.* (2018*b*) demonstrated that this scaling with V for heaving and pitching foils holds well for a twofold change in mean velocity, and oscillations in the flow velocity of up to 38 %. That is, the most important velocity scale for describing the thrust performance is not the flow velocity but the characteristic velocity of the trailing edge. This is completely in accord with the conclusions drawn from slender body theory (§ 2.1), although here we considered both circulatory and added mass forces. It is also not unexpected. The early work by Garrick (1936) on flapping

and oscillating airfoils had already indicated that the mean thrust should depend approximately on V^2 (Garrick's equation 29 simplified), and in the context of fish swimming Bainbridge (1963) indicated that the thrust should depend on 'the square of its speed of transverse movement', although his reasoning is unclear. More recently, Gazzola, Argentina & Mahadevan (2014) offered a mechanistic basis for the importance of the transverse tail velocity, and they showed that for added mass forces the thrust should scale as V^2. However, aerodynamic forces are important when heaving motions are present, and so considerations of pitching and heaving propulsors need to take into account both added mass and lift-based forces (Floryan *et al.* 2017*a*).

Equations (3.6) and (3.9) also suggest that the thrust coefficient C_T (as conventionally defined) scales with St^2. However, this simple scaling argument neglects the drag on the propulsor, and as we saw earlier (as in figure 13) the drag can have an important effect on the total thrust. Thus the conclusions embodied in (3.6) and (3.9) will only hold when the drag is small relative to the total thrust. As suggested by the results shown in figure 13, this requires the Reynolds number and Strouhal number to be sufficiently large.

A more complete treatment, as given by Floryan *et al.* (2017*a*), includes the unsteady effects embodied by $\dot{\alpha}$, the interaction between lift-based and added mass forces, and the drag on the propulsor. In addition, high-frequency and large-amplitude motions will undoubtedly strengthen the nonlinearities in the response; the work of Liu *et al.* (2014) suggests that this will alter the phase differences between forces and motions. As such, terms that are expected to be 90° out of phase (for example, displacement and velocity, or velocity and acceleration) may develop in-phase components. These phase shifts are included in the analysis that follows, although they will be assumed to remain fixed for simplicity. In this way, some degree of nonlinearity is retained in an otherwise linear model.

Following Floryan *et al.* (2017*a*), we obtain for purely heaving motions

$$\left.\begin{aligned} C_T &= c_1 St_h^2 + c_2 St_h^2\, k\, U^* - C_{Dh}, \\ C_P &= c_3 St_h^2 + c_4 St_h^2\, k + c_5 St_h^2\, k\, U^*, \\ \eta &= \frac{c_1 + c_2 k U^*}{c_3 + c_4 k + c_5 k U^*}, \end{aligned}\right\} \tag{3.10}$$

where C_{Dh} is the drag coefficient on the propulsor for heaving motions. Here, $U^* = U_{eff}/U$, and $St_h = 2fh_0/U$. The constants c_i need to be determined by experiment. The thrust coefficient demonstrates a St_h^2 scaling, but the reduced frequency and the effective velocity also make an appearance (however, for small motions $U^* \approx 1$). The expression for the efficiency neglects the drag force, and this inviscid estimate depends only on k and U^*. Furthermore, for large k, the inviscid efficiency tends to a constant value.

Similarly, for purely pitching motions, Floryan *et al.* (2017*a*) finds

$$\left.\begin{aligned} C_T &= c_6 St_\theta^2 + c_7 St_\theta \theta_0 - C_{Dp}, \\ C_P &= c_8 St_\theta^2 + c_9 St_\theta^2 \, k, \\ \eta &= \frac{1}{k} \frac{c_6 k + c_7/2}{c_9 k + c_8}, \end{aligned}\right\} \tag{3.11}$$

where C_{Dp} is the drag coefficient for pitching motions, and $St_\theta = 2fc\theta_0/U$. Note that the expression for efficiency only holds in the limit of negligible drag, and that this inviscid estimate is independent of the Strouhal number, and depends only on the reduced frequency, falling off as k^{-1} for large k.

These results on efficiency may be compared to those of two-dimensional small-amplitude theory. Wu (1971*c*) considered the problem of a rigid plate in sinusoidal pitching and heaving motions in inviscid flow. For pure pitch, the efficiency was found to increase monotonically from a value of zero at $k = 1.781/\pi$ (for smaller values of the reduced frequency the thrust was negative) to a value of 0.5 at $k = \infty$. For pure heave, he found that the efficiency monotonically decreased from a value of one at $k = 0$ to a value of about 0.5 at $k = \infty$. These predictions are rather different from those given by (3.11) and (3.10), so we now consider the comparisons with experiment.

The results for a heaving foil are given in figures 19 and 20. The thrust data collapse well onto a single curve, suggesting that the simplified physics used in the model are sufficient to explain the behaviour of the thrust. In (3.10), the St_h^2 term is rooted in circulatory forces due to the angle of attack, and the $St_h^2 kU^*$ term corresponds to the rate of change of angle of attack. We see therefore that the thrust for heaving motions is entirely due to lift-based forces, and that the effects of unsteadiness on the mean thrust appear to be well captured by the rate of change of angle of attack. The data also suggest that the drag coefficient C_{Dh} is small (of $O(0.1)$) and approximately constant over the conditions explored in the experiment.

Likewise, the power data collapse well onto a single curve, although there is some spread in the data for the stronger motions. The angle of attack, the rate of change of angle of attack and added mass contribute to the power scaling. Power for heaving motions is thus affected by both lift-based and added mass forces, and the essential effects of unsteadiness on the mean power are well captured by the rate of change of angle of attack and added mass. The fact that the mean power is a weakly nonlinear function of the scaling parameters suggests the limits of our model; this is likely caused by the modification of the added mass (Liu *et al.* 2014), although Moored & Quinn (2018) propose an alternative explanation that considers the energy shed into the wake.

The efficiency data are given in figure 20, presented both as a function of Strouhal number and the reduced frequency. For heaving motions, the scaling arguments indicate that the efficiency in the absence of drag should be approximately constant

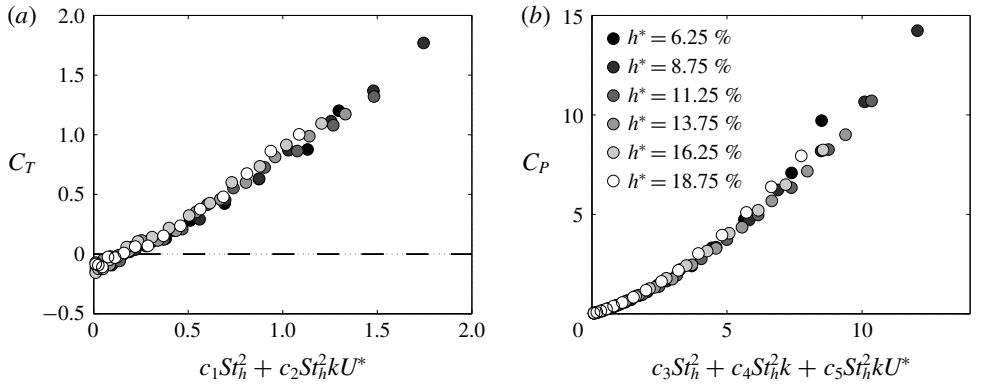

FIGURE 19. Heaving motions of a tear-drop shaped foil. Time-averaged (*a*) thrust and (*b*) power coefficients as functions of the scaling parameters (3.10) for various $h^* = h_0/c$. Adapted with permission from Floryan *et al.* (2017*a*).

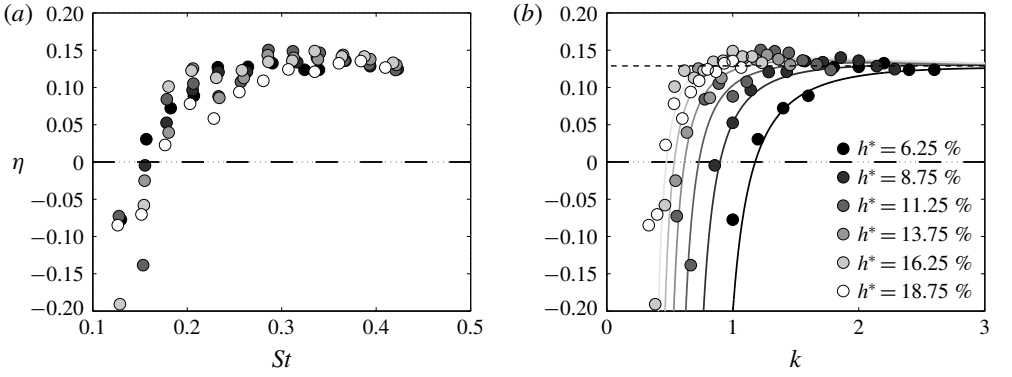

FIGURE 20. Heaving motions of a tear-drop shaped foil. Efficiency as a function of (*a*) Strouhal number *St*, and (*b*) reduced frequency *k*. In (*b*) solid lines indicate the scaling given by (3.10); short dashed line indicates the scaling with $C_{Dh} = 0$ and large *k*. Adapted with permission from Floryan *et al.* (2017*a*).

(for these constants and this range of parameters). For higher values of the reduced frequency we see that the efficiency data indeed approach a constant, marked by the dashed line. The efficiency deviates from this trend for lower values of the reduced frequency and for smaller heave amplitudes due to the viscous drag on the foil. As motions become weaker, they produce less thrust. The drag, however, remains essentially constant. Thus, as the motions become weaker, the drag will constitute a larger portion of the net streamwise force, eventually overtaking any thrust produced and leading to a negative efficiency. The solid lines in figure 20(*b*) show the curve fits of our model after taking the drag into account, where C_{Dh} was estimated from the thrust measurements at zero frequency.

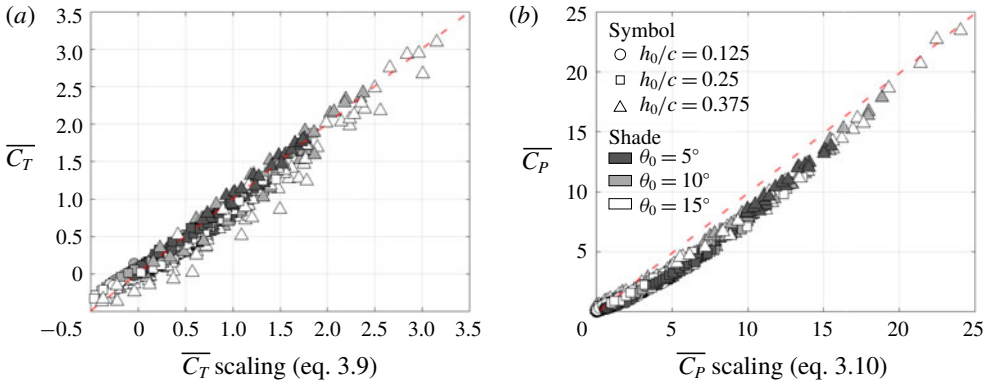

FIGURE 21. Scaling of the time-averaged (*a*) thrust and (*b*) power coefficients for all motion amplitudes and phases for the tear-drop shaped foil tested by Van Buren *et al.* (2018*a*). Adapted with permission from Van Buren *et al.* (2018*a*).

The results on pitch-only motions are similar to those for heave-only motions, in that the scaling given here collapses the data onto a single curve for thrust and power (see Floryan *et al.* (2017*a*) for details). The drag coefficient C_{Dp} was found to be small ($\approx$0.08) and the efficiency data for large values of the reduced frequency followed the k^{-1} scaling predicted by the model.

3.4. *Analysis of heave and pitch motions combined*

To find the total thrust and power expended by the foil in a combined heaving and pitching motion, Van Buren *et al.* (2018*a*) used the same scaling advanced in the previous section. All the motions were assumed to be small, which also implies that $U^* \approx 1$, and the out-of-phase terms were retained, as in Floryan *et al.* (2017*a*). Van Buren *et al.* (2018*a*) gives

$$\overline{C_T} = c_1\, St^2 + c_2\, St_h\theta_0 \sin\phi + c_3\, St_\theta\theta_0 - \overline{C_D}, \tag{3.12}$$

$$\overline{C_P} = c_5\, St^2 + c_6\, kSt_hSt_\theta \sin\phi + c_7\, St_h\theta_0 \sin\phi + c_8\, kSt_h^2 + c_9\, kSt_\theta^2 + c_{10}\, St_\theta\, \theta_0. \tag{3.13}$$

The total motion Strouhal number is defined by $St = 2fa/U$, and $St^2 = St_h^2 + St_\theta^2 + 2St_hSt_\theta \cos\phi$. In the special cases of pure pitch ($h_0 = 0$) and pure heave ($\theta_0 = 0$), these expressions for thrust and power reduce to those given in (3.11) and (3.10), as required.

To verify these scaling relationships, Van Buren *et al.* (2018*a*) performed experiments over a wide range of motion amplitudes and phase differences $[0°, 360°]$, for the same tear-drop shaped foil used by Floryan *et al.* (2017*a*). The results shown in figure 21 display the expected linear relationship between the data and the model thrust, but again the power shows a slight nonlinear behaviour. To make the power

scaling linear, we would need to add a higher-order term (one in St^3), but that is beyond the level of the current analysis. The coefficients were determined via linear regression over the entire experimental dataset.

A number of useful approximations can now be made (Van Buren *et al.* 2018*a*; Floryan *et al.* 2018). The heave-based term in the power, kSt_h^2, which originates from the out-of-phase $\ddot{h}\dot{h}$ term, made an important contribution to the power, and the drag term $\overline{C_D}$ was found to have a linear dependence on the pitch amplitude θ_0, that is, a linear dependence on the projected frontal area for slow motions ($f \to 0$). Furthermore, the pitch-based terms in the thrust and power (associated with constants c_3, c_9 and c_{10}) can be neglected without much penalty on the data collapse. Such terms are all of order $O(\theta_0^2)$, so this is not surprising.

Neglecting these terms, and noting that for biologically relevant motions where phase angles are confined to the range 0°–270° the terms associated with c_2 and c_7 are small compared to the other terms, Van Buren *et al.* (2018*a*) found that

$$C_T = c_1 St^2 - c_4\theta_0, \tag{3.14}$$

$$C_P = a_1 St^2 + a_2 kSt^2 + a_3 kSt_h St_\theta, \tag{3.15}$$

where a_i are new empirical constants. We see that the thrust and power are now independent of phase. Furthermore, based on the values of the constants in (3.14)–(3.15) as determined from the experiment, we can propose an approximate model where

$$C_T = c_1 St^2 - c_4\theta_0, \tag{3.16}$$

$$C_P = a_2 k(St^2 - St_h St_\theta). \tag{3.17}$$

Plotting the thrust and power data against expressions (3.16)–(3.17) yields figure 22. The collapse using these reduced models is similar to that seen using the full expressions (compare with figure 21). Hence,

$$\eta \sim \frac{A^*(St^2 - c_4\theta_0)}{St^3(1 - H^*\Theta^*)}, \tag{3.18}$$

where the constant c_4 sets the relative importance of the drag term compared to the thrust term (in general, we expect c_4 to be a function of Reynolds number). Also, $A^* = a/c$, $H^* = H = h_0/a$ and $\Theta^* = c\theta_0/a$. Parenthetically, at a given Strouhal number, the thrust in combined heave and pitch was consistently higher than the thrust in pitch only by a factor of approximately 5 (this observation will become useful in § 3.10).

We see immediately that to achieve high efficiency, the dimensionless amplitude A^* should be large. This observation is consistent with the argument that large-amplitude motions are more efficient than small-amplitude motions (Alexander 2003). However, there are two potential limiting factors. First, as A^* becomes larger the instantaneous angle of attack increases, so that leading edge vortex formation

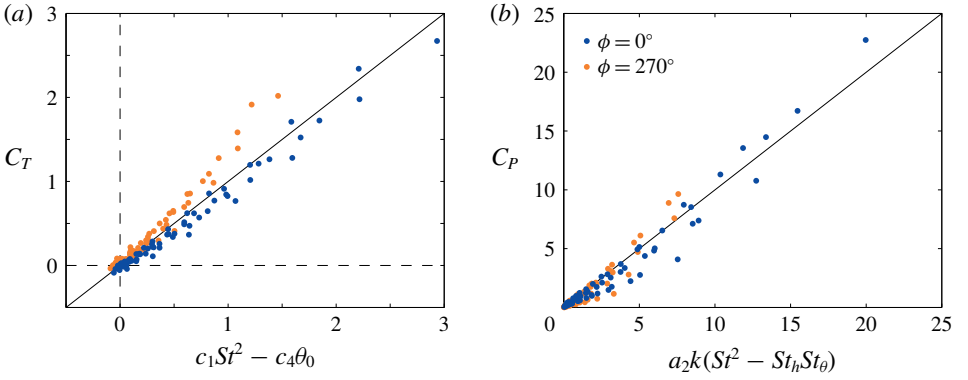

FIGURE 22. Thrust and power data plotted against expressions (3.16)–(3.17) for $\phi = 0°$ (blue) and $\phi = 270°$ (orange). The coefficients are $c_1 = 4.65$, $c_4 = 0.49$, $a_2 = 62.51$. Adapted with permission from Floryan *et al.* (2018).

and dynamic stall effects may become important and the drag model given here would be invalidated. Second, animal morphology naturally sets a limit as to how large they can make A^*. For efficient cruising, therefore, A^* should be as large as an animal's morphology allows, while avoiding dynamic stall at all times.

What about the optimal Strouhal number? Equation (3.18) gives negative efficiencies at low St, a rapid increase with St to achieve a positive peak value at $St = \sqrt{3c_4\theta_0}$, and a subsequent slow decrease with further increases in St as the influence of drag becomes weaker. The comparison between the form given by (3.18) and the data for a heaving and pitching airfoil makes this clear, as displayed in figure 23. The offset drag is critical in determining the low St behaviour and in setting the particular St at which the peak efficiency occurs. In addition, the maximum value of the efficiency is directly related to the value of the drag constant c_4, which further emphasizes the critical role of the drag term in determining the efficiency behaviour.

We expect that the relative importance of the drag, captured by c_4, will depend on the Reynolds number. Our drag model is similar to that for a bluff body, such as a sphere or cylinder, so we expect c_4 will be large at small Reynolds numbers, and decrease as the Reynolds number increases until it reaches approximately 1000, above which the drag will be almost constant (at least for $Re < 2 \times 10^5$, although biological measurements imply that the drag may remain constant up to $Re = 10^8$) (Gazzola *et al.* 2014). Our conclusion is consistent with biological measurements (at least for swimmers), where the preferred Strouhal number appears to decrease as the Reynolds number increases, until it reaches an asymptotic value (Gazzola *et al.* 2014). The drag on the propulsor is the crucial factor in creating an efficiency peak which dictates the cruising conditions of swimming animals. In other words, energetic considerations set the kinematics of the propulsor to the most efficient one,

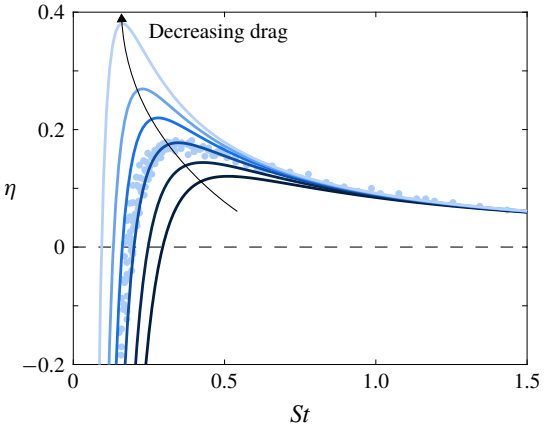

FIGURE 23. Efficiency η as a function of St. Data are as given for a heaving and pitching NACA0012 foil (Quinn *et al.* 2015). Solid lines are given by (3.18) with a fixed proportionality constant of 0.155. The drag constant, c_4, is set to 0.5, 0.35, 0.23, 0.15, 0.1 and 0.05 as the colours vary from dark to light. Reproduction with permission from Floryan *et al.* (2018).

and the net thrust of the propulsor at peak efficiency balances the drag of the body to set the cruising speed.

As noted earlier, the drag behaviour will depend on the profile shape of the propulsor as well as the Reynolds number, and it is likely that there exists an optimum profile for a given Reynolds number and set of operating conditions. Van Buren *et al.* (2019*b*) used variety of techniques to address this optimization problem, and figure 24 shows the path of optimization from the starting foil, NACA0012, to the optimized foil, on a map of the efficiency and thrust coefficient for two reduced frequencies, $k = 0.4$ and 1.0. The pitch and heave amplitudes were chosen to match experiments, with $c = 80$ mm, $h_0 = 30$ mm and $\theta_0 = 15°$. Although the optimization was aimed only at improving efficiency, the optimization improves both the efficiency and thrust by approximately 30 % and 15 %, respectively, at $k = 1$. The optimized foil performance exceeds other common foil shapes as well, including the EPPLER 836 and a dolphin fluke profile. Figure 25 shows the efficiency as it varies with Reynolds number. At $k = 1$ the foil is in the regime of high thrust but far from having peak efficiency, and the impact of Reynolds number is small. However, at $k = 0.4$ the foil is near peak efficiency and the Reynolds number becomes much more important, and the benefits of having an optimized foil increase with Reynolds number. Hence, the foil kinematics and shape are tightly intertwined and must be simultaneously taken into consideration to truly maximize performance.

There remains the question of setting an operating point where reasonable efficiency and thrust can be achieved at the same time. To illustrate this challenge, we use the data obtained by Van Buren *et al.* (2018*a*) and plot the efficiency versus

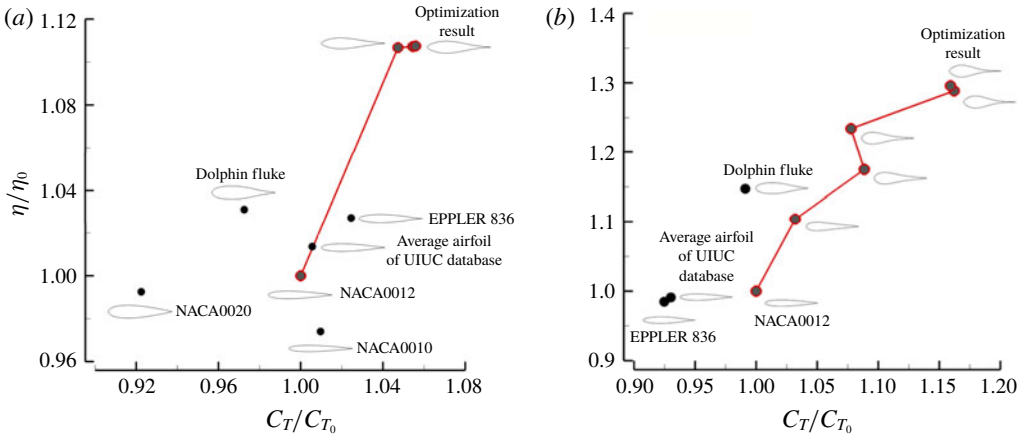

FIGURE 24. Efficiency and thrust for optimized two-dimensional foil, as they develop during optimization, relative to the NACA0012 reference foil. (*a*) $k = 0.4$; (*b*) $k = 1.0$. Other common foil shapes are also shown. Reproduction with permission from Van Buren *et al.* (2019*b*).

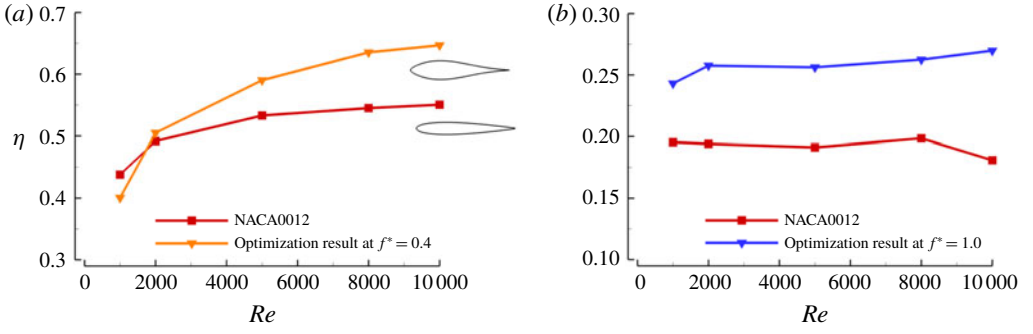

FIGURE 25. Reynolds number dependence of efficiency for optimized two-dimensional foil, compared to the NACA0012 reference foil. (*a*) $k = 0.4$; (*b*) $k = 1.0$. Reproduction with permission from Van Buren *et al.* (2019*b*).

the thrust coefficient for the cases where $210° \leqslant \phi \leqslant 330°$, as in figure 26. The data appear to display a Pareto front, where the maximum instantaneous angle of attack is less than about 30°. This limit of the angle of attack suggests that leading edge vortex formation and dynamic stall effects need to be avoided to achieve the best performance (Tuncer & Kaya 2005; Young *et al.* 2006; Young & Lai 2007). The presence of this front indicates that for rigid propulsors, even at optimum conditions, high efficiency motions occur at low thrust, and increasing the thrust reduces the efficiency.

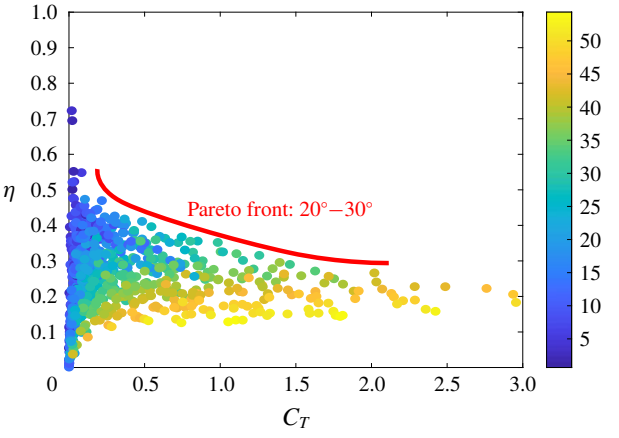

FIGURE 26. Combined heave and pitch motions of a rigid foil. Data points are coloured by maximum angle of attack. The Pareto front is broadly defined by α_m between 20° and 30°. Data obtained by Van Buren *et al.* (2018*a*).

3.5. *Flexibility in oscillatory motions*

In § 2.2 we examined the performance of flexible panels in undulatory motion, mainly by reference to the results obtained by Quinn *et al.* (2014, 2015). We now consider flexible panels in oscillatory motion by considering the work by Dewey *et al.* (2013) on flexible pitching panels. The flexibility was passive, in the sense that the foils were actuated in pitch at the leading edge, and the resulting foil shape was set by the interaction between the panel and the fluid flow. This passive flexibility might be a reasonable model for the flukes of mammals, where muscles appear to be absent. Seven panels with different flexibilities were considered, including one rigid panel (P_1–P_∞ in table 1). The flexibility of the panel was defined by the effective stiffness of the panel Π_1', where

$$\Pi_1' = \frac{E\delta^3}{12(1-\nu_p^2)\rho U_\infty^2 c^3}. \tag{3.19}$$

This definition of the effective stiffness differs from the bending stiffness coefficient of an isotropic plate $E\delta^3/[12(1-\nu_p^2)]$ used by Shyy *et al.* (2010). See also Alben (2008), where $R_2 = \Pi_1'$. In addition, $\Pi_1' = k_1^2/\Pi_1^2$, where Π_1 is the effective flexibility used by Quinn *et al.* (2014) (see § 2.2). It is difficult to assign a corresponding value of the effective stiffness for fish, but it is likely in the range $1.4 < \Pi_1' < 4$ (panels P_3–P_5).

Figure 27 shows the thrust coefficients as a function of reduced frequency. For the flexible panels, the thrust coefficient initially increases with k until a maximum is reached after which it declines slightly with a further increase in k. The peaks occur at a frequency that is approximately 50 % higher than the structural resonance

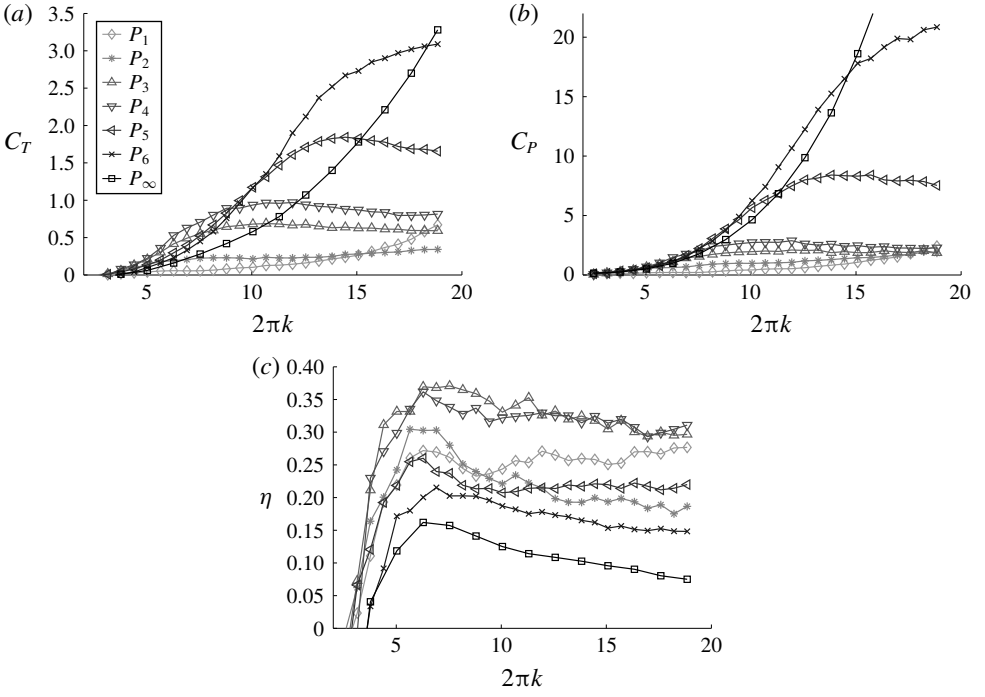

FIGURE 27. Coefficients of thrust, power and efficiency as a function of reduced frequency for nominally two-dimensional pitching panels. Panel properties given in table 1. Adapted with permission from Dewey *et al.* (2013).

frequency f_1 for each panel, as measured when the panel is immersed in water (for Panels P_1 and P_2 the resonant frequency of the first beam bending mode is lower than the frequencies examined here). Each of the flexible panels generates a higher thrust coefficient than its rigid counterpart over a certain frequency range. For example, at $k = 10$, the results in figure 27(*a*) indicate that panels P_5 and P_6 yield thrust coefficients that are twice as large as the rigid panel (P_∞). The coefficient of power C_P (figure 27*b*) demonstrates qualitatively similar trends.

Figure 27(*c*) indicates that the moderately flexible panels (P_3 and P_4) yield the highest propulsive efficiencies, and that there is an optimal stiffness for maximum efficiency. The global maximum efficiency for the rigid panel reaches only 16 % at $k = 6.3$, but for the flexible panels it reaches about 38 % (panel P_3) at the same reduced frequency. In addition, the flexible panels exhibit high efficiency across a wide range of frequencies whereas the rigid panels display sharper peaks. As the frequency is increased, therefore, the performance benefit of the flexible panels over the rigid panels becomes even more pronounced. This trend may be contrasted with the efficiency curve of a typical propeller, which shows a relatively slow rise with the advance ratio up to its peak value followed by a sharp decline.

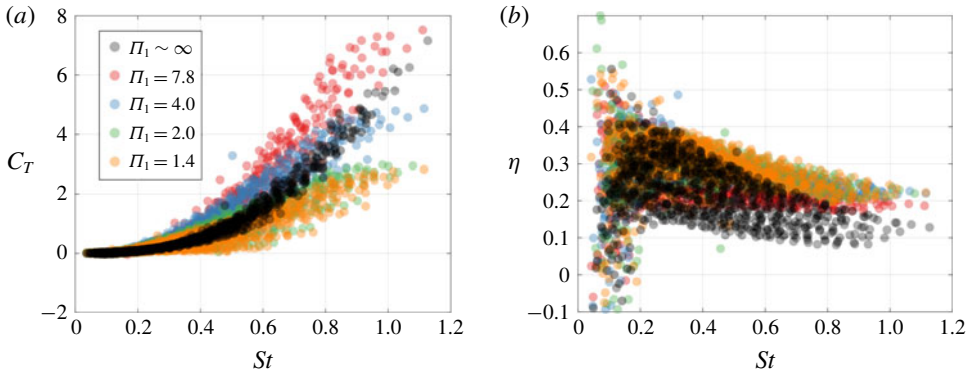

FIGURE 28. Effects of flexibility on time-averaged (*a*) thrust and (*b*) efficiency for a pitching and heaving panels separated by phase $\phi = 270°$. Pitch amplitudes $\theta = \{6°, 9°, \ldots, 15°\}$; heave amplitudes $h_0/c = \{0.083, 0.167, \ldots, 0.33\}$; and frequencies $f = \{0.2, 0.25, \ldots, 1\ \text{Hz}\}$. The rigid panel corresponds to $\Pi_1' \sim \infty$. See table 1. Adapted with permission from Van Buren *et al.* (2019*a*).

Dewey *et al.* (2013) concluded that the global maximum in propulsive efficiency across a range of panel flexibilities is achieved when two conditions are simultaneously satisfied: (i) the oscillation of the panel yields a Strouhal number in the range $0.25 < St < 0.35$; and (ii) the frequency of motion is tuned to the structural resonant frequency of the panel.

These conclusions were made with respect to panels in pitch only. To demonstrate the effects of flexibility on the performance of panels in combined pitch and heave motions, consider the results shown in figure 28. These panels had effective stiffnesses similar to those used by Dewey *et al.* (2013) – see table 1. For certain flexibilities, there is a clear envelope where the thrust production is up to 1.5 times higher than the thrust of a rigid panel. Here, the peak efficiency is less influenced by flexibility than thrust, but the efficiency tends to remain higher over a larger Strouhal number range, which also means higher thrust levels. Thus, those animals that can control their fin stiffness using muscle action may be able to maintain high efficiency at higher cruising speeds by actively changing the stiffness.

3.6. *Effects of aspect ratio*

So far, we have analysed rectangular foils or panels in oscillatory motion that were effectively two-dimensional, as in Floryan *et al.* (2017*a*) and Van Buren *et al.* (2018*a*), or the panels had a fixed aspect ratio, as in Quinn *et al.* (2014). The effects of aspect ratio have not yet been considered, but it is obviously an important consideration given the range of caudal fin and fluke shapes seen in nature. These effects were explored systematically for rectangular panels by Buchholz & Smits (2008), Green & Smits (2008), Dai *et al.* (2012), Dewey *et al.* (2013) and, more

recently, Ayancik *et al.* (2018). Chopra (1974) extended Lighthill's (1970) and Wu's (1971*a*) inviscid flow theory for a thin plate to the three-dimensional case of finite aspect ratio, for combined pitch and heave motion. He concluded that reducing the aspect ratio would lead to lower thrust and efficiency.

Buchholz & Smits (2008) studied rectangular rigid panels in pitch with $\mathcal{AR} = 0.54$, 0.83. 1.11 and 2.38. For the highest aspect ratio, the panel spanned the working section, and so was taken to represent the two-dimensional case ($\mathcal{AR} = \infty$). At a given Strouhal number, the thrust coefficient (defined on the basis of panel area sc, as usual) decreased with increasing aspect ratio, but the effects on efficiency were generally rather minor. Green & Smits (2008) analysed the same data, and showed that the thrust results could be collapsed by the scaling $C_T^* = C_T(1 + c'a/s)$ where c' is an empirical constant, and noted that this scaling is similar to the that used to account for the effects of aspect ratio on the lift coefficient in finite wing theory. This last observation is somewhat misleading in that the thrust produced by a pitching panel is primarily due to added mass forces, not circulatory forces, but as we shall see the added mass scaling with aspect ratio follows a somewhat similar variation.

Dewey *et al.* (2013) considered rectangular flexible panels in pitch with $\mathcal{AR} = 0.5$, 1.0, 1.5 and 2.0, and found that flexible panels did not exhibit a monotonic trend with aspect ratio (see figure 29*a*). For panel P_4, for example, the coefficient of thrust increases with aspect ratio at lower frequencies, while it decreases with aspect ratio at higher frequencies. The results for C_P demonstrate qualitatively similar trends as those of C_T (figure 29*b*). Whereas for the rigid panels the coefficient of power monotonically increases with reduced frequency, for the flexible panels it initially increases with reduced frequency until a maximum is reached at which point the coefficient of power tends to level off. The peak in C_P occurs at a frequency that is approximately 50 % higher than the structural resonance frequency, which is the same point where the thrust reaches its maximum. In addition, for each flexibility examined, the efficiency increases with aspect ratio as observed by Buchholz & Smits (2008) for rigid panels (figure 29*c*), although this effect is rather small compared to the effects of flexibility, where there is a clear optimal stiffness to achieve maximum efficiency.

For all the flexible panels considered by Dewey *et al.* (2013), only the first mode was excited, so that f_1 was the single resonant frequency of interest. In such cases, the elastic forces in bending become important, so that the dynamics will be governed by the balance between inertial, fluid forces and elastic forces acting on the panel. The inertial force F_i is the mass of the panel times its characteristic acceleration, so that $F_i \sim \rho_p sc\delta(f^2 c)$, and for thin panels in water this is expected to be small compared to the other forces. The fluid force F_v is taken to be due to added mass, so that $F_v \sim \rho s^2 c(f^2 c)$. Here, Dewey *et al.* (2013), chose to use $\rho s^2 c$ for the added mass, which is the form appropriate to panels with small aspect ratios,

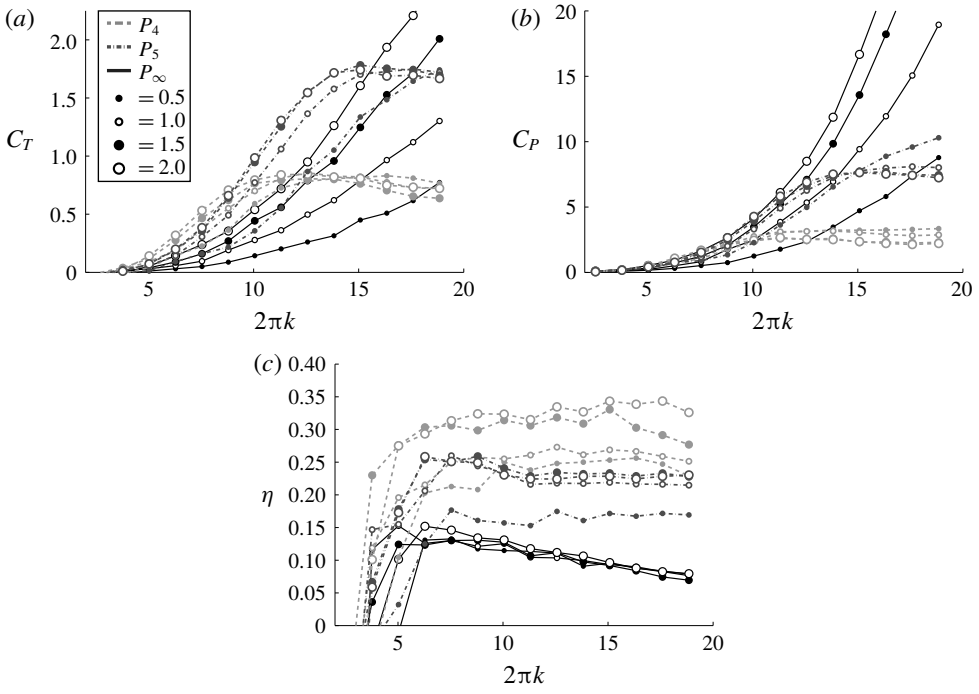

FIGURE 29. Coefficients of thrust, power and efficiency as a function of reduced frequency for finite-aspect-ratio pitching panels. Panel properties given in table 1. Adapted with permission from Dewey *et al.* (2013).

even though the aspect ratios in their experiments varied from 0.5 to effectively infinite. The elastic forces depend on the flexural stiffness of the panel ($EI \sim Es\delta^3$), and so the characteristic elastic force is $F_e = Es\delta^3/c^2$.

When flexibility is the dominant effect, we expect that the thrust will scale with F_e, and the characteristic power expended in bending is then expressed by the product of F_e and a characteristic velocity. Dewey *et al.* (2013) chose fc for this velocity scale, whereas a more natural choice might be fa, since that represents the characteristic velocity of the trailing edge. However, the pitch amplitude at the leading edge was fixed ($\theta_0 = 7.2°$), and if we ignore Panels P_1 and P_2, the amplitude of the trailing edge motion compared to its value for the rigid panel was only approximately 20 %–30 % larger for the infinite-aspect-ratio cases, and 25 %–40 % larger for the finite-aspect-ratio cases. Hence the difference between choosing fc and fa is generally rather small for these experiments. If we accept this scaling, the non-dimensional thrust production and power input for flexible panels are then given by

$$\widetilde{C_T} = \frac{T}{F_e} = \frac{Tc^2}{E\delta^3 s} \quad \text{and} \quad \widetilde{C_P} = \frac{P}{fcF_e} = \frac{Pc^2}{E\delta^3 s(fc)}. \tag{3.20a,b}$$

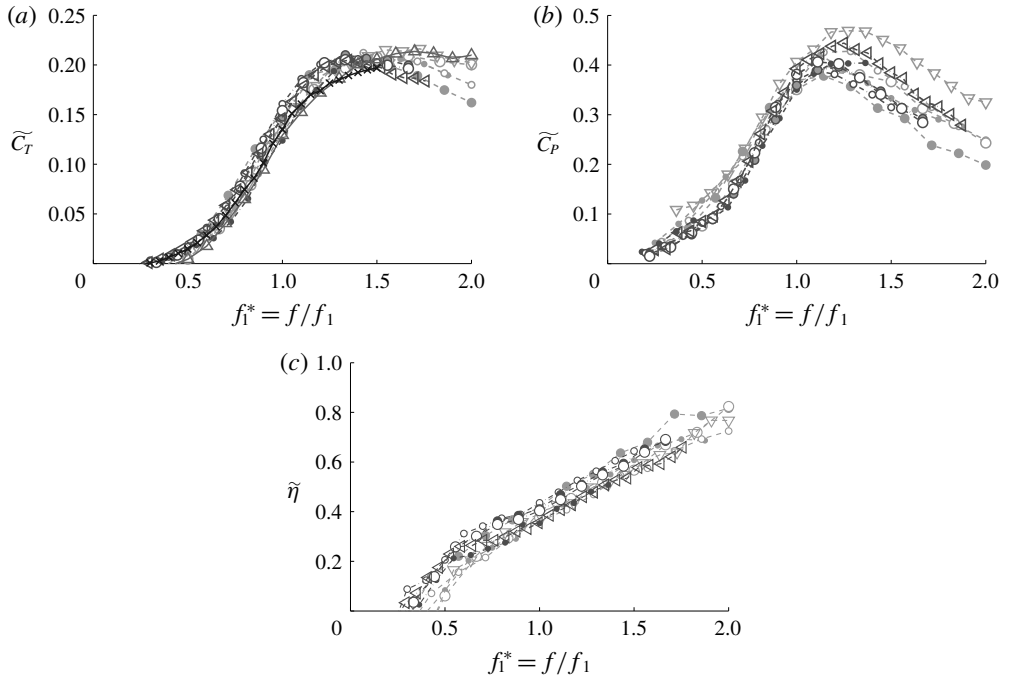

FIGURE 30. Flexible pitching panels with $0.5 \leqslant \mathcal{AR} \leqslant \infty$. (*a*) Scaled thrust behaviour; (*b*) scaled power behaviour; and (*c*) scaled efficiency behaviour. Symbols are the same used in figure 27, but only the flexible panel data for panels P_3 to P_6 are presented here. Reproduction with permission from Dewey *et al.* (2013).

This suggests a new efficiency parameter given by $\widetilde{\eta} = T(fc)/P = k\eta$. The thrust, power and efficiency data in this new scaling are shown in figure 30, where $f_1^* = f/f_1$. This scaling collapses the data remarkably well across all aspect ratios examined. The effects of aspect ratio for these flexible panels therefore seem to be well accounted for by the elastic response of the panel.

For the rigid panels examined by Dewey *et al.* (2013) we expect that the data should scale with the characteristic fluid force F_v. That is, we can define new thrust and power coefficients according to

$$\widetilde{T} = \frac{T}{F_v} = \frac{T}{\rho s^2 c(f^2 c)} \quad \text{and} \quad \widetilde{P} = \frac{P}{fcF_v} = \frac{P}{\rho s^2 c(f^2 c)(fc)}, \tag{3.21a,b}$$

and, as before, $\widetilde{\eta} = T(fc)/P = k\eta$. The collapse of the data shown in figure 31 is quite remarkable, particularly in that it is independent of aspect ratio.

To see why, remember that the characteristic fluid force F_v is due to added mass. For small-aspect-ratio panels we would expect the added mass to vary as $\rho s^2 c$, that is, the circumscribing circle that is at the basis of added mass models is defined by the span. This is also used in slender body theory where the circumscribing circle is defined by the cross-sectional area of the body. However,

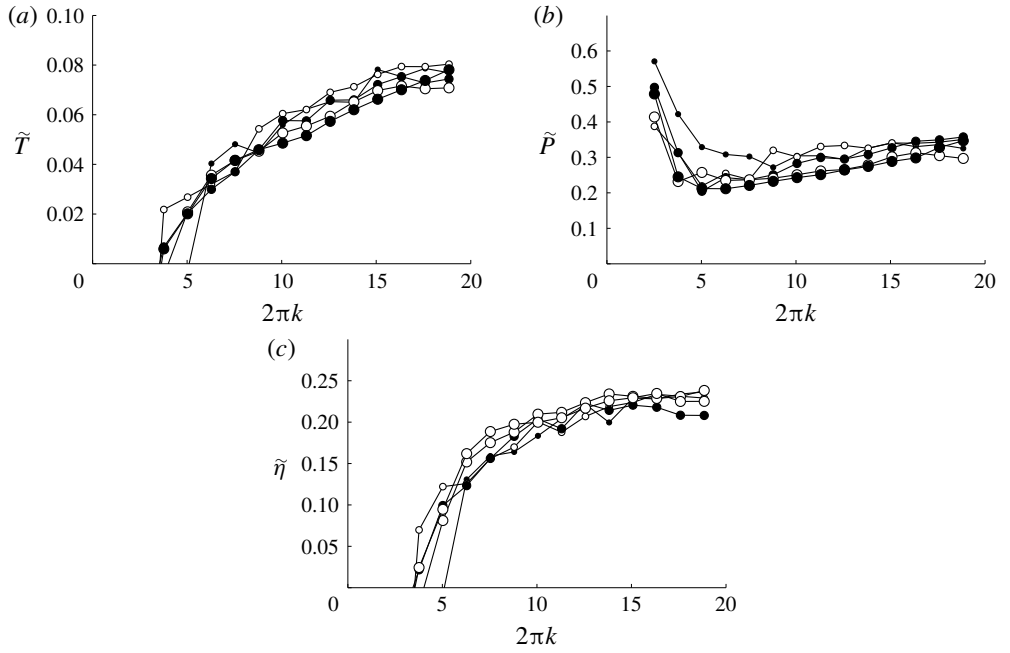

FIGURE 31. Rigid pitching panels (P_5) with $0.5 \leqslant \mathcal{AR} \leqslant \infty$. (*a*) Scaled thrust behaviour; (*b*) scaled power behaviour; and (*c*) scaled efficiency behaviour. Symbols are the same used in figure 27. Adapted with permission from Dewey *et al.* (2013).

for large-aspect-ratio panels we would expect the added mass term to look like ρsc^2, that is, the circumscribing circle is defined by the chord. The force F_v was defined using $\rho s^2 c$ for the added mass term, but given the range of aspect ratios covered in the experiments, the added mass term should depend on aspect ratio, something like $m \sim \rho sc^2 g(\mathcal{AR})$, where the function $g = \mathcal{AR}$ for $\mathcal{AR} \ll 1$ and $g = 1$ for $\mathcal{AR} \gg 1$. A suitable form would be $g = \mathcal{AR}/(1 + \mathcal{AR}^n)^{1/n}$, where the exponent n needs to be determined. The form with $n = 1$ was proposed by Brennen (1982), but the comparison with the data given in figure 32 is not encouraging. Rather unexpectedly, the data suggest that the variation with aspect ratio is not smooth and that they seem better fitted by a discontinuous function $g = 0.5\mathcal{AR}$ for $\mathcal{AR} < 2$, and $g = 1$ for $\mathcal{AR} \geqslant 2$. That is, the preferred added mass representation seems to be $m = \rho s^2 c$ for $\mathcal{AR} < 2$, and ρsc^2 for $\mathcal{AR} \geqslant 2$. Therefore Dewey *et al.* (2013)'s choice for the added mass term appears to embody precisely the correct scaling for the effects of aspect ratio, for the range of values considered in their experiments.

We conclude that the data for the thrust production and power input to the fluid for rigid and flexible panels in pitch collapse using scalings for the characteristic fluid force and the characteristic elastic force, respectively. In particular, the effects of aspect ratio for the flexible panels is contained within the characteristic elastic force, and for the rigid panels it is contained in a judicious choice for the added

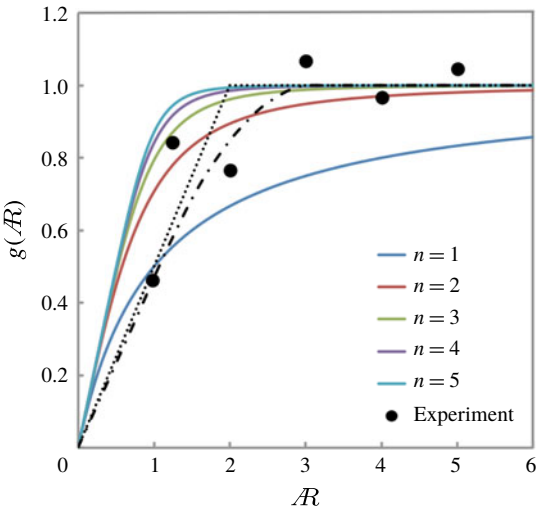

FIGURE 32. Added mass variation with aspect ratio, $g = \mathcal{AR}/(1 + \mathcal{AR}^n)^{1/n}$. Dotted line is the discontinuous function proposed here. Chain-dotted line is from Brennen (1982), apparently a smoothed curve fitted to the experimental data from Patton (1965), as reproduced here.

mass term in the characteristic fluid force. For those panels that have stiffnesses between what we have called 'rigid' or 'flexible' the scaling will undoubtedly depend on both the elastic force and the fluid force.

So far we have only discussed the effects of aspect ratio on panels in pitch. For panels in heave, the circulatory forces will be important, and so it seems likely that that the circulatory forces should vary with aspect ratio as indicated by finite wing theory, that is, they would reduce by the factor $\mathcal{AR}/(\mathcal{AR}+2)$. Recent results by Ayancik *et al.* (2018) support this expectation, although the results for finite wing theory are probably not reliable for $\mathcal{AR} < 1$, and for more complicated planform shapes.

3.7. *Effects of planform*

All the foils considered so far have been rectangular in planform. Caudal fins, of course, exhibit a wide range of shapes, as shown in figure 33 (see also figure 12). The shape of the caudal fin clearly affects the fish flow kinematics, swimming efficiency, acceleration and manoeuvrability (Sambilay Jr 1990; Lauder 2000; Sumich & Morrissey 2004). To understand the effects on performance, a number of investigations have systematically altered the planform of fin-like propulsors. For example, Webb (1973) employed caudal fin amputation as a tool to examine drag and thrust relations for a swimming fish, using the Lighthill (1969) model to analyse the thrust mechanics. Karpouzian, Spedding & Cheng (1990) analytically compared

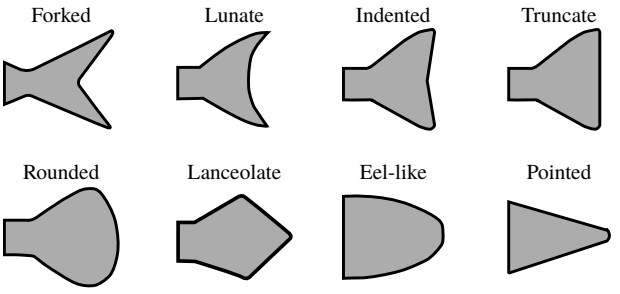

FIGURE 33. The variety of fish caudal fin types. Reproduction with permission from Van Buren *et al.* (2017*a*).

the performance of fins with varying aspect ratio and sweep, and both parameters were found to have a significant impact on thrust and efficiency. The effects of planform shape as it applies to many fish-like propulsors were studied analytically and numerically for inviscid flow by Chopra & Kambe (1977), who explored the complex relationship between thrust and (inviscid) efficiency when the sweep, taper and aspect ratio were varied. They found that 'compared with a rectangular tail, a curved leading edge as in lunate tails gives a reduced thrust contribution from the leading edge suction for the same total thrust; however, a sweep angle of the leading edge exceeding about 30° leads to a marked reduction of efficiency'. The reduction in leading edge suction would help to reduce the incidence of dynamic stall, as well as the possible formation of a strong leading edge vortex, so it seems likely that a curved leading edge would help push the performance envelope to higher angles of attack. The reduced efficiency at high sweep angles is associated with the reduced thrust developed by such planforms.

In addition, Li, Luodin & Lu (2012) and Liu & Bose (1993) compared the performance of three whale fins using a quasi-vortex-lattice numerical method. By varying pitch and heave amplitude, it was found that the tail shape significantly altered the conditions for maximum efficiency. Lauder *et al.* (2011) isolated the effects of trailing edge shape for highly flexible panels of very low aspect ratio ($0.194 \leqslant \mathcal{A}R \leqslant 0.340$) akin to eel-like swimmers, and found experimentally that the trailing edge could be manipulated to improve the panel self-propelled swimming speed.

Part of the complexity introduced by a change in planform is that it usually changes more than one fin parameter at the same time. For example, changing the sweep alters the angle of the leading and trailing edges simultaneously, and changing the planform of the panel also affects its flexibility. Even for rigid panels the planform can assume many different shapes, so that a multitude of geometric parameters come into play. Three studies that have addressed these issues to some extent are Green, Rowley & Smits (2011) and King, Kumar & Green (2018) who studied the behaviour of low aspect ratio trapezoidal panels with square trailing

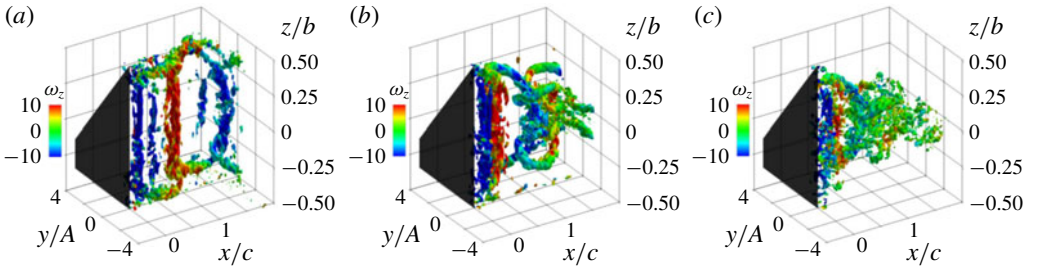

FIGURE 34. Wake development for pitching trapezoidal foil. Isometric views of Q isosurfaces at a value of 1 % Q_{max} at $t/T = 0$. Q isosurfaces are coloured by the local value of ω_z. (*a–c*) $St = 0.17$, 0.37 and 0.56. Adapted with permission from King *et al.* (2018).

edges (an approximation to the truncate caudal fin shape), and Van Buren *et al.* (2017*a*) who investigated foils with planforms that varied systematically from a shape that approximated a forked tail to that of a lanceolate tail.

King *et al.* (2018) focused primarily on the wake structure that develops downstream of the trapezoidal foil with increasing Strouhal number. Isometric views of the phase-averaged three-dimensional isosurfaces of Q are shown in figure 34, where the Q criterion proposed by Hunt, Wray & Moin (1988) helps to identify the vortex structure. They observed that the spanwise vortices shed from the trailing edge of the panel formed a reverse von Kármán vortex street in at least some sections of the wake at all Strouhal numbers considered. Streamwise vortices were created near the spanwise tips of the panel, connecting with spanwise vortices to create vortex rings, and a connected chain of vortex rings was shown to exist at each Strouhal number, prior to the onset of wake breakdown. The induced velocities of the vortex rings were consistent with the transverse expansion and a spanwise compression of the wake, and increasing the Strouhal number produced a greater amount of transverse wake expansion, together with a greater amount of spanwise wake compression. Such observations are consistent with those of Buchholz & Smits (2006) for a pitching rectangular panel with aspect ratio $\mathcal{AR} = 0.54$ (see figure 14), who demonstrated that the wake formation is dominated by the streamwise vorticity generated at the panel edges, driving the wake towards the panel centre, very much like the axis switching phenomena of non-axisymmetric jets (Dhanak & Bernardinis 1981).

The experiments by Van Buren *et al.* (2017*a*) were directed more to understanding the effects of changing the trailing edge shape, which was varied from concave to convex (see figure 35). The aspect ratio was held constant ($\mathcal{AR} = 1$) as was the foil planform area, so that the propulsive performance among the different foils could be compared directly. The wake visualizations displayed in figure 35 show that the angle of the trailing edge bends the trailing edge vortices so that the natural vortex

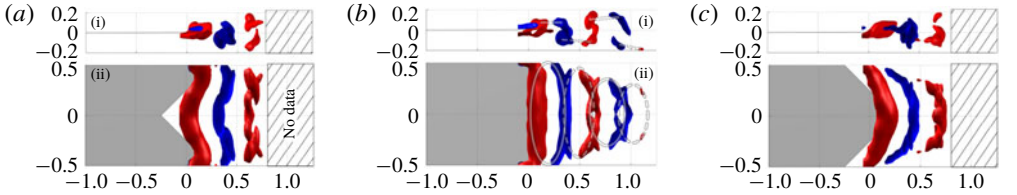

FIGURE 35. Isosurfaces of phase-averaged spanwise vorticity $\langle\omega_z^*\rangle$, for $St = 0.2$. Red is positive, blue is negative. Spanwise (i) and panel-normal (ii) views are shown for three cases. (*a–c*) concave, square and convex. Adapted with permission from Van Buren *et al.* (2017*a*).

bending and wake compression could be promoted (convex) or delayed (concave). This change in vortex formation had a significant impact on the time-averaged velocity field, with a single jet-like wake structure appearing for the concave panels, and a four jet structure for the convex panels. In terms of performance, the thrust and efficiency generally improved going from concave to convex trailing edges. For instance, the most convex panel produced a thrust that was approximately 15 % higher than the square panel. For concave panels, the peak efficiency was reduced by a maximum of approximately 3 % compared to the square trailing edge case, while for convex panels the peak efficiency was improved by a maximum of approximately 2 %. These were significant differences in that the average efficiency of the square panel was only approximately 10 %.

We take these results to imply that the evolution of the various fish caudal fin shapes may include other purposes than simply improving thrust and efficiency; most fish have concave tails, but the data suggest that this may not generate the optimum performance. It is possible that the diversity in caudal fin trailing edge shape fulfils other evolutionary purposes, or it may be that trailing edge shape works together with another parameter to improve performance, for example, sweep angle. It is also possible that the relatively small benefits due to trailing edge shape seen here might be outweighed by the much larger effects due to flexibility or an adaptation to the motion profile.

3.8. *Intermittent motions*

Many aquatic animals, such as sharks and seals as well as small schooling fish, exhibit an intermittent swimming behaviour, sometimes called burst-and-coast swimming (Videler & Weihs 1982; Blake 1983*b*; Fish, Fegely & Xanthopoulos 1991; Chung 2009). Fish practice intermittent swimming while hunting, fleeing a predator or pursuing a mate, and exhibit a wide range of ratios of burst-to-coast times (Kramer & McLaughlin 2001). Of interest here is the possible energy benefit of intermittent swimming versus continuous swimming.

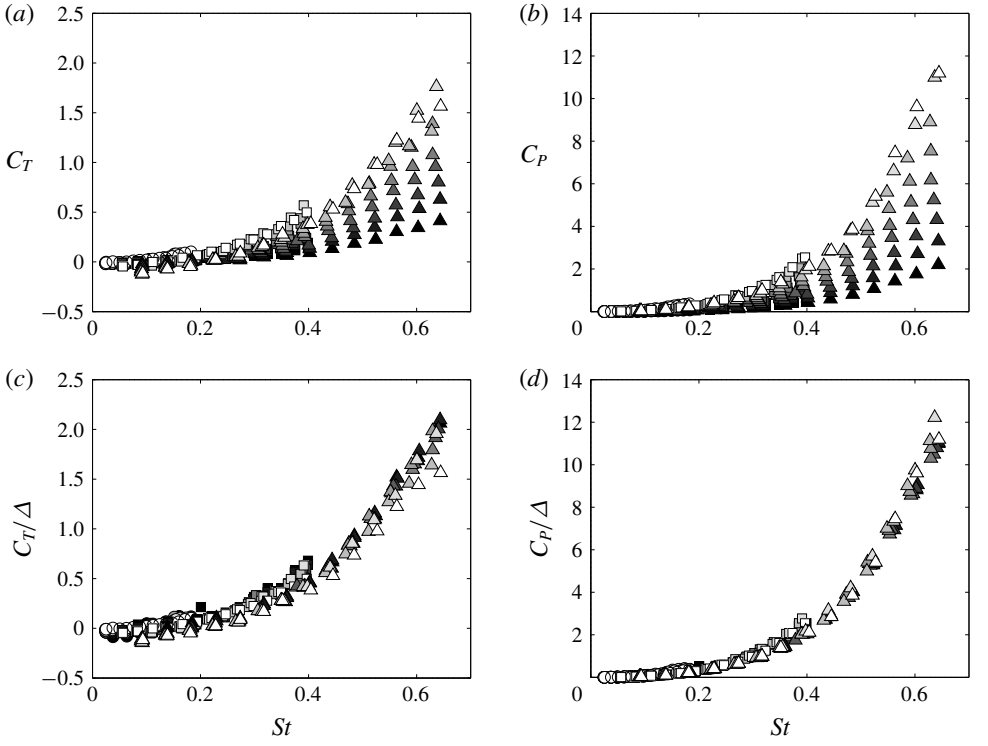

FIGURE 36. (*a*) Thrust and (*b*) power coefficients as functions of Strouhal number. (*a*,*b*) Conventional scaling. (*c*,*d*) Coefficients normalized by duty cycle. Dark to light symbols represent increasing duty cycles, ranging from $\Delta = 0.2$ to 1 every 0.1. Symbols identify pitch amplitudes of $\theta_0 = 5°$ (circle), 10° (square) and 15° (triangle). Adapted with permission from Floryan *et al.* (2017*b*).

To help answer this question, Floryan, Van Buren & Smits (2017*b*) conducted experiments on a two-dimensional tear-drop foil in pitch, and varied the swimming duty cycle Δ from 0.2 to 1, where 1 represents continuous swimming. The results show that the mean thrust and power scale linearly with the duty cycle (figure 36), indicating that individual bursts of activity in intermittent motions are independent of each other (Akoz & Moored 2018 arrived at a similar result). This conclusion was corroborated by flow visualizations, which show that the main vortical structures in the wake did not change with duty cycle, at least for the range of Strouhal numbers considered. The results also indicate that wake vortex proximity to the propulsor itself does appear to be important. We expect that at higher Strouhal numbers these conclusions may not continue to hold because the interaction among the wake vortices would become more intense.

Of particular interest is the free swimming performance during intermittent swimming, that is, the point where the mean thrust is equal to the mean drag. Does the duty cycle decrease the energy required to travel a certain distance? Floryan

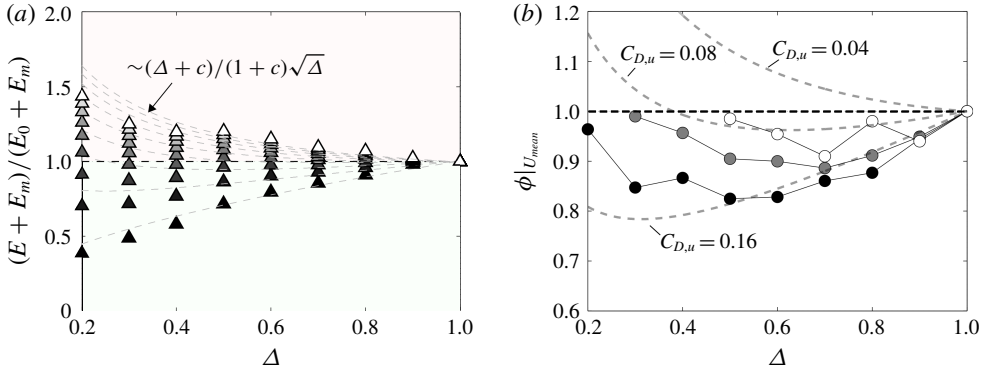

FIGURE 37. (*a*) Ratio of energy expended by intermittent motions to energy expended by continuous motions, including metabolic energy losses, as a function of duty cycle for $\theta_0 = 15°$, all frequencies, with $C_{Db} = 0.1$. Each point is an average over all frequencies. The shading denotes the value of the metabolic power fraction c_m, 0 to 2 in intervals of 0.25 (dark to light). (*b*) Ratio of energy expended by intermittent motions to energy expended by continuous motions, restricted to equal mean speeds. Dashed lines correspond to the model. The symbol grey scale corresponds to three values of (dimensional) mean speed chosen, $U_{mean} = 0.2, 0.25, 0.3$ (dark to light). The frequency of the intermittent motion was chosen so that it would have a speed equal to the continuous motion. Reproduction with permission from Floryan *et al.* (2017*b*).

et al. (2017*b*) argue that over a fixed distance, the energy ratio $\phi = E/E_0$ should scale according to $\sqrt{\Delta}$, where E is the energy expended by intermittent motion, and E_0 is the energy expended by continuous motion with the same actuation. Their data generally follow this trend, and so for this simple case it would appear that intermittent motions are always energetically favourable. However, apart from energy spent on swimming, aquatic animals also expend energy on metabolic processes, E_m. When the mean power spent on metabolic processes is assumed the same for continuous and intermittent motion, and that it remains a constant fraction c_m of the power lost in continuous swimming, Floryan *et al.* find that

$$\frac{E+E_m}{E_0+E_{m0}} = \frac{\Delta+c_m}{(1+c_m)\sqrt{\Delta}}. \tag{3.22}$$

From figure 37(*a*) we see that the data and the scaling tell the same story: even though intermittent motions expend less energy on swimming, the metabolic losses can play a significant role because intermittent motions take more time to traverse a given distance than continuous motions. The extra time to travel will increase the metabolic energy losses, and this effect may dominate the benefits gained in reducing swimming energy losses. Estimates for c_m from nature are difficult to obtain, but it is likely in the range shown in figure 37(*a*), and so the possible benefits of intermittent swimming will vary with species.

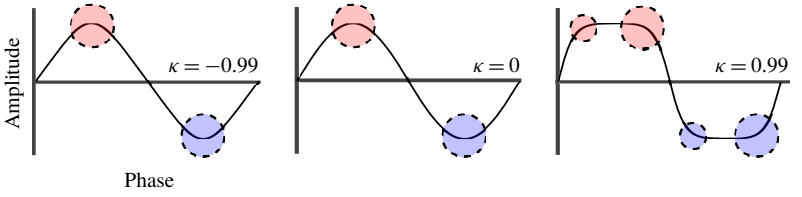

FIGURE 38. Jacobi elliptic functions produce varying actuation waveform shape based on the elliptic modulus, κ. Coloured circles represent points of vortex production in the cycle based on PIV measurements, and smaller circles correspond to secondary vortices (see figure 41). Adapted with permission from Van Buren *et al.* (2017*b*).

It is also possible to restrict ourselves to motions which produce the same mean speed, that is, $\phi|_{U_{mean}}$. For example, it may be that a continuous motion produces the same mean speed as an intermittent motion with a duty cycle of 0.5 actuating at twice the frequency. Which strategy is best if a swimmer wants to traverse a given distance in a given amount of time? The results are plotted in figure 37(*b*), where the lines in the figure are derived using the propulsive model derived in § 3.1 to make estimates for the thrust and power exerted in the free swimming condition. It appears that intermittent motions continue to be energetically favourable with the added time restriction. Energetically optimal duty cycles exist, and savings are greater for lower speeds, at least for the data considered here, despite having to increase the frequency of actuation in order to match the mean speed of continuous motions.

3.9. *Non-sinusoidal motions*

Thus far, we have always assumed that the foil is actuated sinusoidally, but there may be times when animals use non-sinusoidal motions, and there may be benefits to doing so. In terms of optimization, Kaya & Tuncer (2007) numerically studied heaving and pitching airfoil performance in laminar air flow, and used gradient-based optimization of the motion paths to show that there were significant benefits to thrust by moving non-sinusoidally. They found that motions that maintain a constant angle of attack for longer periods of time, a topic also considered by Read *et al.* (2003), produced higher thrust than purely sinusoidal motions. Similar results were reported by Van Buren *et al.* (2017*b*), who used Jacobi elliptic functions to vary the shape of the actuation from more triangular ($\kappa = -0.99$), to sinusoidal ($\kappa = 0$), to more square-like motions ($\kappa = +0.99$), as shown in figure 38.

Their results for heaving motions of a tear-drop shaped foil are shown in figure 39. We see that square-like motions exhibit much higher thrust and power than the triangular-like and sinusoidal motions. Similar results were found for pitch. This variation of thrust with κ suggested that the thrust may scale with waveform peak velocity, especially for heaving motions. Empirically, a function P_2 was found that was only a function of the peak velocity. When the scaling of Floryan *et al.* (2017*a*)

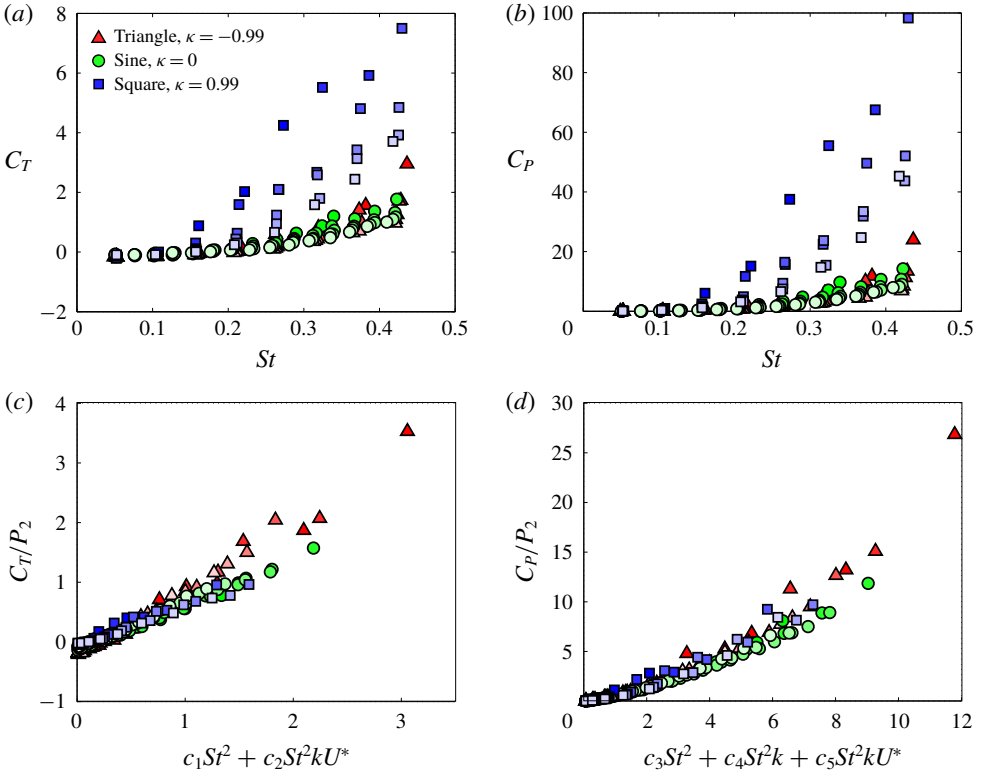

FIGURE 39. Performance as a function of Strouhal number, for heave. (*a*,*b*) (i) Thrust coefficient; (ii) power coefficient versus Strouhal number. (*c*,*d*) (i) Thrust and (ii) power modified by the lateral velocity scale plotted against the scaling proposed by Floryan *et al.* (2017*a*). Symbol colour identifies the waveform shape, and tone represents amplitude of motion ranging from low (dark) to high (light). For heave, $h/c =$ 6.25 %–18.75 % every 2.5 %. For pitch $\theta = 3°$–$15°$ every $2°$. Adapted with permission from Van Buren *et al.* (2017*b*).

is combined with this peak velocity scaling parameter, there is an encouraging collapse of the thrust and power coefficients for a large range of motion parameters, as shown in figure 39. The empirical constants used in the scaling were identical to those found by Floryan *et al.* (2017*a*) for purely sinusoidal motions.

The efficiency as a function of thrust is given in figure 40. For heave, the effects of waveform shape are rather minor (within the range of amplitudes studied), but for pitch increasing κ tends to decrease the efficiency at a given thrust, and the highest peak efficiency is achieved with sinusoidal motions. We see that actuation waveform can be used to regulate thrust/efficiency trade-offs during locomotion, for a given frequency and amplitude.

In addition to its effect on the performance, the waveform shape has a dramatic impact on the vortex structure produced in the wake of the foil. The rapid start

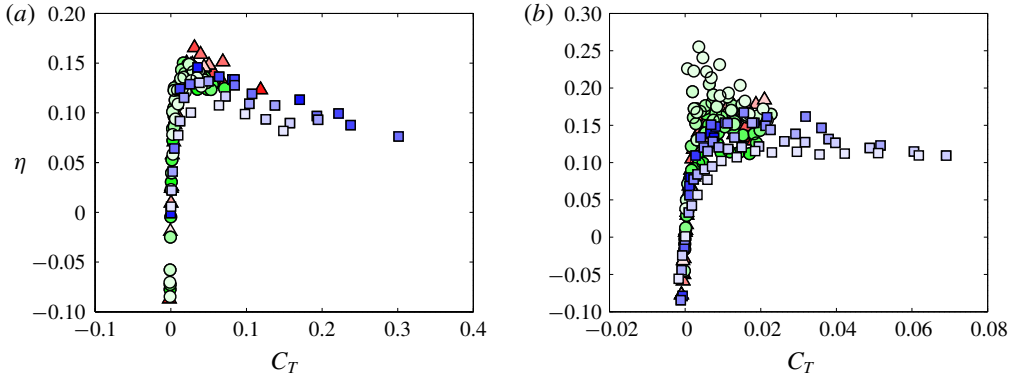

FIGURE 40. Efficiency versus thrust coefficient for (*a*) heave, and (*b*) pitch. Symbols and colours as in figure 39. Adapted with permission from Van Buren *et al.* (2017*b*).

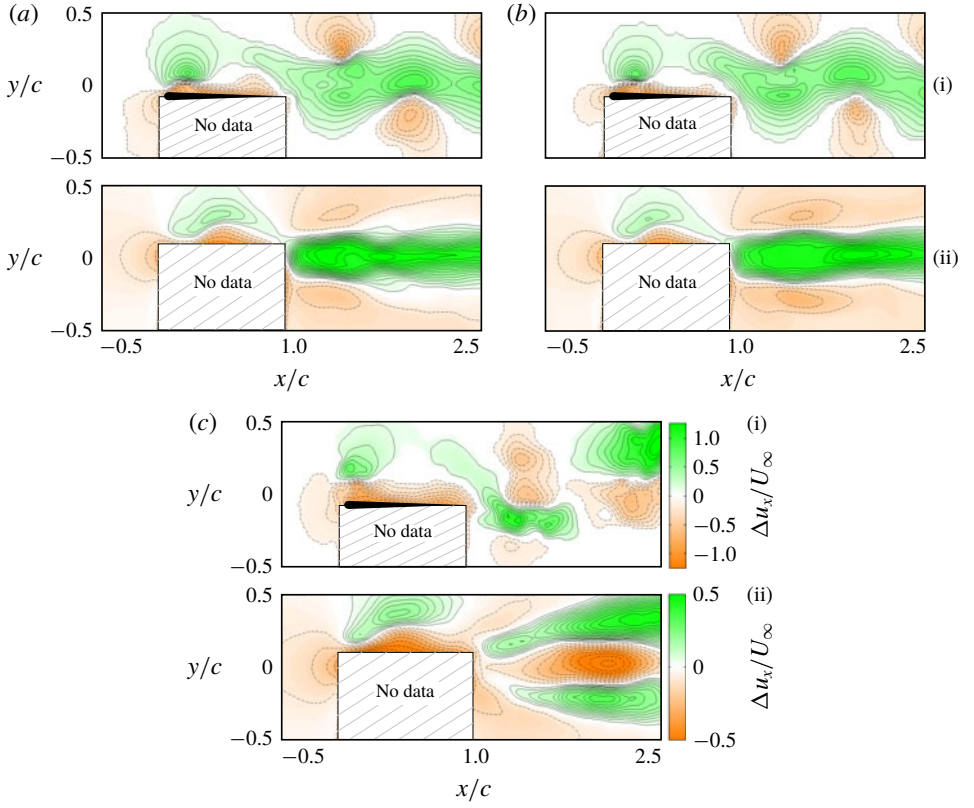

FIGURE 41. Heaving foil. (i) Phase- and (ii) time-averaged change in streamwise velocity ($h/c = 12.5\,\%$, $St = 0.4$). Waveform: (*a*) triangular-like $\kappa = -0.99$; (*b*) sinusoidal $\kappa = 0$; (*c*) square-like $\kappa = 0.99$. Reproduction with permission from Van Buren *et al.* (2017*b*).

and stop of square-like wave type motions produces vortex pairs instead of the typical vortex street, resulting in a dual-jet velocity wake (see figure 41). This wake structure was associated with large increases in the thrust, producing up to four times higher forces than sinusoidal motions. These effects are more pronounced in heave than in pitch, though similar trends were found in both cases and across all Strouhal numbers studied ($St = 0.2$, 0.3, and 0.4). Triangular-like and sinusoidal motions showed more typical behaviour, with a reverse von Kármán vortex street and a single jet-like wake.

As Van Buren *et al.* (2017*b*) indicate, these results imply that animals and vehicles could use non-sinusoidal propulsive motions to increase thrust, efficiency or swimming speed, depending on the need. A square wave motion, for example, could be used to accelerate quickly, whereas a sinusoidal motion could be used for efficient cruise. These ideas are consistent with the diversity of motion types seen in biological swimmers, and they suggest new strategies for effective motor control in swimming robots.

3.10. *Contribution of caudal fin to total thrust*

Our aim in modelling the propulsive forces produced by an oscillating foil was to help understand the swimming of fish and mammals. At the outset (§ 3), we made the assumption that for oscillatory swimming the caudal fin is the principal source of thrust, and the body is the principal source of drag. Now that we have some reasonable models for the production of thrust by heaving and pitching foils we can examine the plausibility of this approximation, at least for the case of the tuna. To do so, we revisit the analysis by Bainbridge (1963) of the swimming performance of dace, bream and goldfish (see figure 12). In particular, Bainbridge estimated the contribution of the caudal fin to the total thrust by using biological data on lateral velocity and planform area distributions. He assumed that for a segment of planform area dA the local thrust contribution is proportional to $V^2\,\mathrm{d}A$, so that

$$T \sim \int_b V^2\,\mathrm{d}A + \int_c V^2\,\mathrm{d}A = I_1 + I_2, \tag{3.23}$$

where T is the mean total thrust in steady swimming, V is the local transverse velocity and the first integral is taken over the body (from the snout to the fork) while the second integral is taken over the caudal fin. This scaling with the lateral velocity is entirely in accord with many of the observations we have made so far. As indicated earlier, Bainbridge found that the proportion of the total thrust contributed by the caudal fin varied from 45 % for the bream, 65 % for the goldfish, to 84 % for the dace, while Gray (1933) estimated 40 % for the whiting.

A similar analysis may be performed for a member of the tuna family, in particular the kawakawa (*Euthynnus affinis*, or mackerel tuna, see figure 12). Donley & Dickson (2000) measured the mean maximum intervertebral lateral displacement

of juvenile kawakawa during steady swimming, which together with measurements of the tail beat frequency and the assumption of sinusoidal actuation gives an estimate of V. Taking the planform aspect from the literature (as in figure 12) allows us to estimate the terms in (3.23), and the result indicates that for this member of the tuna family the caudal fin contributes approximately 40 % of the total thrust.

These analyses, however, overlook an important distinction between the thrust due to body movement and that due to caudal fin oscillation: the former is primarily a flapping or pitching motion, whereas the latter is primarily a combination of heave and pitch motions with a phase difference of approximately 270°. The difference is that heave is a much more effective means of generating thrust compared to pitch. For rigid, rectangular panels, for example, Floryan *et al.* (2017*a*) found that at a Strouhal number $St = 0.35$ a heaving motion gives $C_T = 0.6$ compared to a value of 0.2 for a pitching motion, at comparable amplitudes of the trailing edge motion ($h/c = 0.1875$ for heave, and $\theta = 10° = 0.1745$ rad for pitch), see § 3.1. That is, under similar conditions heave produces about three times the thrust produced by pitch. The difference is even larger in combined pitch and heave, where our earlier observations indicated a factor closer to five (see § 3.4). Therefore, in estimating the thrust contributions of the body motion compared to the caudal fin motion, we need to take these differences into account by weighting the caudal fin contribution given by I_2 in (3.23) by a factor close to five (for similar amplitudes of motion). When this is done for the kawakawa example, we find that the contribution by the caudal fin to the total thrust increases from 40 % to 77 %.

We also need to take into account the effects of aspect ratio, $\mathcal{A}$. The measurements on rectangular foils by Dewey *et al.* (2013) and theoretical considerations by Ayancik *et al.* (2018) indicate that the fall-off in thrust due to the contribution made by added mass forces is important only at small values of $\mathcal{A}$ (figure 32), and the fall-off due to circulatory forces depends approximately on $\mathcal{A}/(2 + \mathcal{A})$. For pitching motions, the thrust is due primarily to added mass forces, so that it needs to be discounted by a factor similar to that shown in figure 32. For heaving motions, the thrust is primarily due to circulatory forces, so that it needs to be discounted by the factor approximately given by $\mathcal{A}/(2 + \mathcal{A})$. For the kawakawa caudal fin, we have $\mathcal{A} = 5$, and for the body we use the local aspect ratio defined as $s^2/\mathrm{d}A$, where s is the local span of the fish in side view. The contribution by the caudal fin to the total thrust then increases from 77 % to 86 %.

We see that in modelling the propulsive forces produced by swimming fish of the kind considered here (low predation, steady swimming, high flow; Langerhans & Reznick 2010), it seems reasonable to assume that the caudal fin is the principal source of thrust, and the contribution made by the body motion can be discounted.

4. Mobuliform swimming

For undulatory swimming, we used eels and lampreys as prototypical examples, and for oscillatory swimming we put forward tuna and dolphins. Batoid swimmers like rays use a different propulsive mechanism, in that they use their greatly enlarged pectoral fins to propel themselves, and can display either undulatory or oscillatory swimming behaviours, called rajiform and mobuliform, respectively (Rosenberger & Westneat 1999; Rosenberger 2001; Fish *et al.* 2016, 2017). Rays are fish of the order Batoidei. They are related to sharks, and the order encompasses more than 500 species. Most species live on the ocean floor, but a few, such as the manta ray, live in the open sea. Rays such as the blue spotted and southern stingray are undulatory swimmers and display at least a full wavelength of activation on their pectoral fin ($\lambda^* = \lambda/c < 1$), while manta rays and cownose rays are oscillatory swimmers and display less than a full wavelength of activation ($\lambda^* > 1$). One of the important aspects of mobuliform swimming is that rays precisely control the shape of their fins to swim and manoeuver. While this is also true for undulatory swimmers such as eels and knifefish, manta rays provide a good example of an oscillatory swimmer that uses active rather than passive flexibility to control the amplitude and wavelength of the actuating waveform.

To help understand the swimming of rays that use oscillatory propulsion, Clark & Smits (2006) performed experiments on a flexible fin that replicated some features of the pectoral fin of a manta ray or cownose ray. The cross-section of the fin was approximated by a NACA0020 airfoil section, which is close to that seen in nature, and the planform was semi-elliptic, with the root chord assumed to act as a plane of symmetry ($\mathcal{AR} = 1.2$ for the half-span). The fin was aligned with the flow direction, and it was actuated in a travelling wave motion, with the wave amplitude increasing linearly along the span from root to tip (see figure 42). By changing the phase angle ϕ between the individual actuators from 0, 30, 60, 90, 120 and 240°, the wavelength could be varied from $\lambda^* = \infty$, to 12, 6, 4, 3 and 2. Since the wavelength was always larger than the chord of the fin, the motion was oscillatory in nature, with the added feature of having a fin with a chord-wise profile that conformed to the prescribed actuation.

The thrust and efficiency results are shown in figure 43. Thrust generally increases with Strouhal number, as expected, but local peaks are present in the vicinity of $St = 0.3$–0.35, where the Strouhal number is based on the amplitude of the trailing edge motion at midspan. The highest thrust was found to occur at either $\lambda^* = 4$ or 6 ($\phi = 90°$ or 60°). These wavelengths also gave the highest efficiencies, with a global maximum efficiency of approximately 54 % for $\lambda^* = 6$, which is impressive for such a relatively crude approximation to manta ray locomotion. Also, the optimal wavelength of $\lambda^* = 4$ to 6 is in accord with observations of manta rays in nature by Rosenberger (2001). Most intriguingly, the efficiencies displayed two local peaks; one at approximately $St = 0.2$ to 0.225, and another at approximately $St = 0.3$.

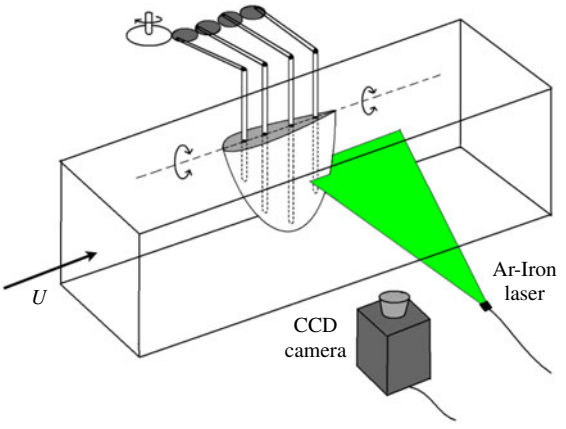

FIGURE 42. Fin actuation mechanism. A DC motor with a speed controller turns a shaft at frequency f which powers a gear train. The rotation of the gears actuates rods which impose a travelling wave along the fin through rigid spars. PIV was used to investigate the structure of the wake. Reproduction with permission from Dewey, Carriou & Smits (2012).

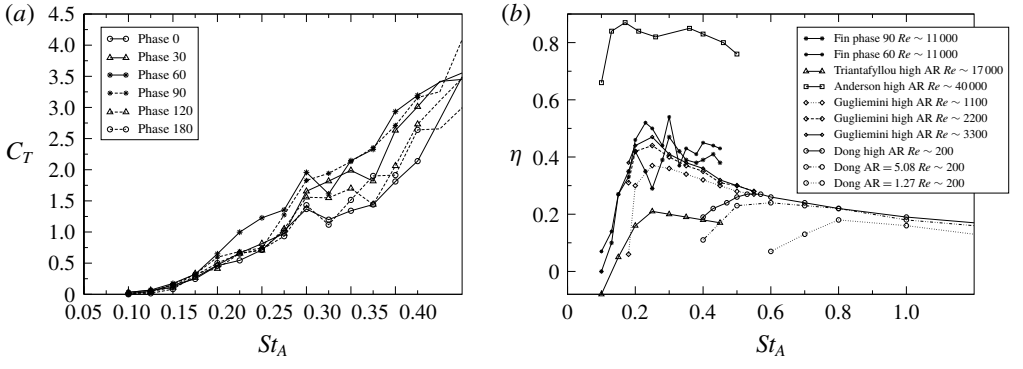

FIGURE 43. (*a*) Coefficient of thrust for different traveling wave phase differentials ϕ. (*b*) Efficiency at $\phi = 60°$ and $90°$ ($\lambda^* = 6$ and 4). For the fin, the Strouhal number St_A is based on $\bar{A}$, the trailing edge displacement at the mid-chord; for the other cases, $A = \bar{A}$. Reproduction with permission from Clark & Smits (2006).

Dewey *et al.* (2012) used PIV to investigate the wake structure corresponding to these thrust and efficiency trends. The highly three-dimensional wake exhibited a structure that varied with both the spanwise location and the streamwise location. Because the circulation distribution at any point in the flapping cycle varies along the span of the fin, with it being zero at the root and tip, the trailing edge vortex varies in strength along the span. It also varies in time, of course, because the motion is periodic. At $St = 0.25$ and $\lambda^* = 4$ (highest efficiency condition), both a 2S and a 2P wake were observed at different spanwise locations (2S at midspan), as also seen by Heathcote, Wang & Gursul (2008) for flexible foils where the

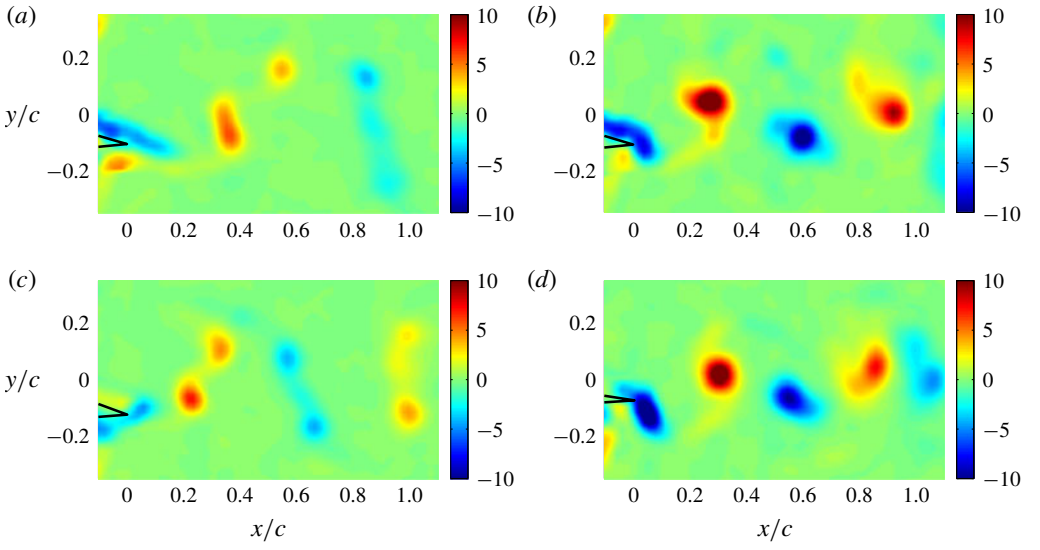

FIGURE 44. Wake transition from 2P to 2S with increasing Strouhal number at the midspan: (*a*,*b*) $\lambda^* = 6$, $St = 0.15$ (*a*) and $St = 0.25$ (*b*); (*c*,*d*) $\lambda^* = 3$, $St = 0.2$ (*c*) and $St = 0.3$ (*d*). Flow is from left to right, and the trailing edge of the fin is outlined in black. Adapted with permission from Dewey *et al.* (2012).

peak-to-peak amplitude increased with span. The wavelength of actuation had a significant impact, in that it caused a transition from a 2S to a 2P structure at a particular downstream location (see figure 44). This transition appeared to be directly linked to the increasing phase delay of the trailing edge of the fin with decreasing wavelength, and indicates that for a given Strouhal number (or non-dimensional wavelength) there is a specific non-dimensional wavelength (or Strouhal number) such that a transition from a 2S to 2P wake structure occurs. In fact, a transition from 2P to 2S always occurs with increasing Strouhal number, and at a fixed Strouhal number the distance from the trailing edge to the location of the bifurcation increases with decreasing wavelength. Similarly, for a fixed bifurcation distance, the longest wavelength ($\lambda^* = \infty$) causes the bifurcation to occur at the lowest Strouhal number.

5. Wake resonance

Moored *et al.* (2012) sought to gain a better understanding of the conditions necessary for efficient propulsion, and how these conditions make themselves evident in the flow field. They introduced the concept of wake resonance, which is based on a linear stability analysis of the mean velocity profile in the wake. The work built on that originally done by Triantafyllou *et al.* (1993), who performed a linear stability analysis of the time-averaged wake behind a two-dimensional

foil pitching about its quarter chord point with a small amplitude. They found that the maximum spatial growth of the instabilities of the velocity jet occurred over a range of Strouhal numbers of 0.25 to 0.35, corresponding to the range of Strouhal numbers observed for fish and mammals in nature. Hence, they inferred that efficient swimming occurs at the frequency of maximum amplification (see also § 1.2). That is, the perturbation waves will have the largest amplification (per unit input energy) at the 'resonant' frequency of the jet profile (where there is maximum spatial growth), and that this will cause an expedient shear layer roll up and entrainment, and result in the strongest momentum jet for a given input energy. Thus a peak in the propulsive efficiency is expected when the fin is driven at the resonant frequency of the jet. By inference, this peak was associated with a 2S (reverse von Kármán vortex street), and an 'optimal' Strouhal number range of $0.25 < St < 0.35$.

Although many animals swim in this Strouhal number range, we have seen that there are many cases where the peak efficiency falls outside this range (Anderson *et al.* 1998; Taylor, Nudds & Thomas 2003; Clark & Smits 2006; Buchholz & Smits 2008). Furthermore, elongated fish such as the eel and lamprey typically generate $2P$ wakes meaning that two pairs of vortices are shed per cycle (see figure 4*a*), and fish with low aspect ratio propulsors such as rays can exhibit both $2S$ and $2P$ wakes depending upon the fin kinematics (see figure 44). Other more elaborate wake structures have also been observed in the wakes of heaving and pitching airfoils (Lewin & Haj-Hariri 2003; Lentink *et al.* 2008).

For the model of mobuliform locomotion studied by Clark & Smits (2006) and Dewey *et al.* (2012), the instantaneous flow field at any spanwise location is characterized by the formation of wavy jet structures (figure 45*b*), while the time-averaged flow field exhibits a jet-like behaviour (figure 45*c*). In most cases, the jet can be considered weakly non-parallel, meaning that the characteristic length scale of a velocity profile changes slowly in the downstream direction as compared to the instability wavelength (Chomaz 2005), and so the flow may be analysed using a local spatial stability analysis. Moored *et al.* (2012) found that when the driving frequency is close to the jet resonant frequency, a peak in efficiency is expected. This may occur at more than one Strouhal number. With $\lambda^* = 4$, for example, the driving frequency is nearly coincident with the resonant frequency at two Strouhal numbers: $St = 0.2$ and 0.3 (see figure 46). Moreover, the two wake resonant frequencies from the linear stability analysis match closely to the two peaks observed in efficiency.

To connect the analysis to the wake structure, Moored *et al.* (2012) then examined the eigenfunction, $\phi(y)$, associated with each eigenvalue. The eigenfunctions relate to stream function perturbations and thus velocity perturbations that must be superimposed onto the base flow. The linear vorticity perturbation can also be obtained from $\phi(y)$ and captures many of the features of the observed wake

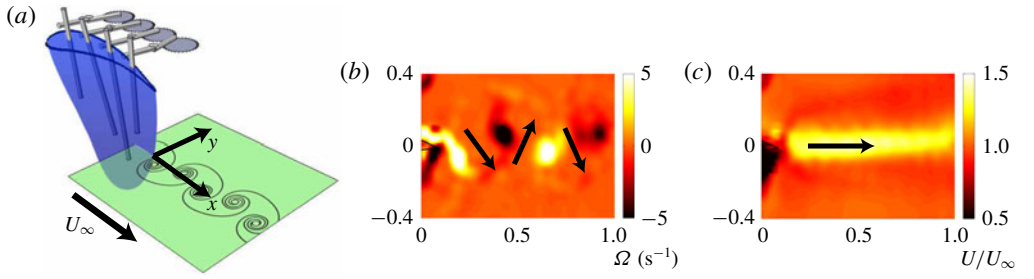

FIGURE 45. (*a*) Schematic of a ray-like robotic pectoral fin and the vortex wake structure at a laser illuminated plane, (*b*) reverse von Kármán vortex street inducing a wavy jet and (*c*) time-average velocity field. The *x*- and *y*-coordinates are non-dimensionalized with the chord length, *L*. Adapted with permission from Moored *et al.* (2012).

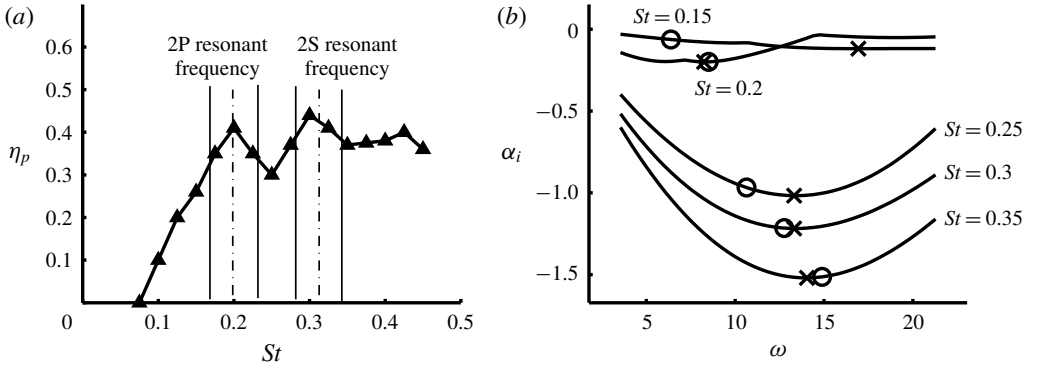

FIGURE 46. (*a*) Propulsive efficiency data of the elliptical fin measured by Clark & Smits (2006) for $\lambda^* = 4$. Dashed lines denote the resonant frequencies found by the linear stability analysis. The solid lines denote the regions of uncertainty in the wake resonant frequencies. (*b*) Stability curves for 5 velocity profiles taken from DPIV data measured by Dewey *et al.* (2012), where α_i is the imaginary part of the complex wavenumber. The × mark the resonant frequency of a stability curve while the ○ mark the driving frequency used to generate the velocity profile. Reproduction with permission from Moored *et al.* (2012).

structures. For example, the vorticity eigenmodes for $\lambda^* = 4$ are compared with the wake structure at the midspan at three Strouhal numbers in figure 47. At the first peak in efficiency (at $St = 0.2$ for this wavelength), the vorticity perturbation exhibits a characteristic $2P$ pattern, although some asymmetry occurs and the eigenfunction has a slightly different spatial wavelength compared to the experimentally observed vortices. The experimentally observed wake displays a $2P$ structure in the near wake, but for $x > 0.5$ a transition from $2P$ to $2S$ is occurring, which is reflected in the time-averaged velocity field (not shown here). When the Strouhal number increases, as in figure 47(*c–f*), the wake structures and vorticity eigenmodes begin to display the characteristics of a $2S$ wake. Each of the wake resonant frequencies

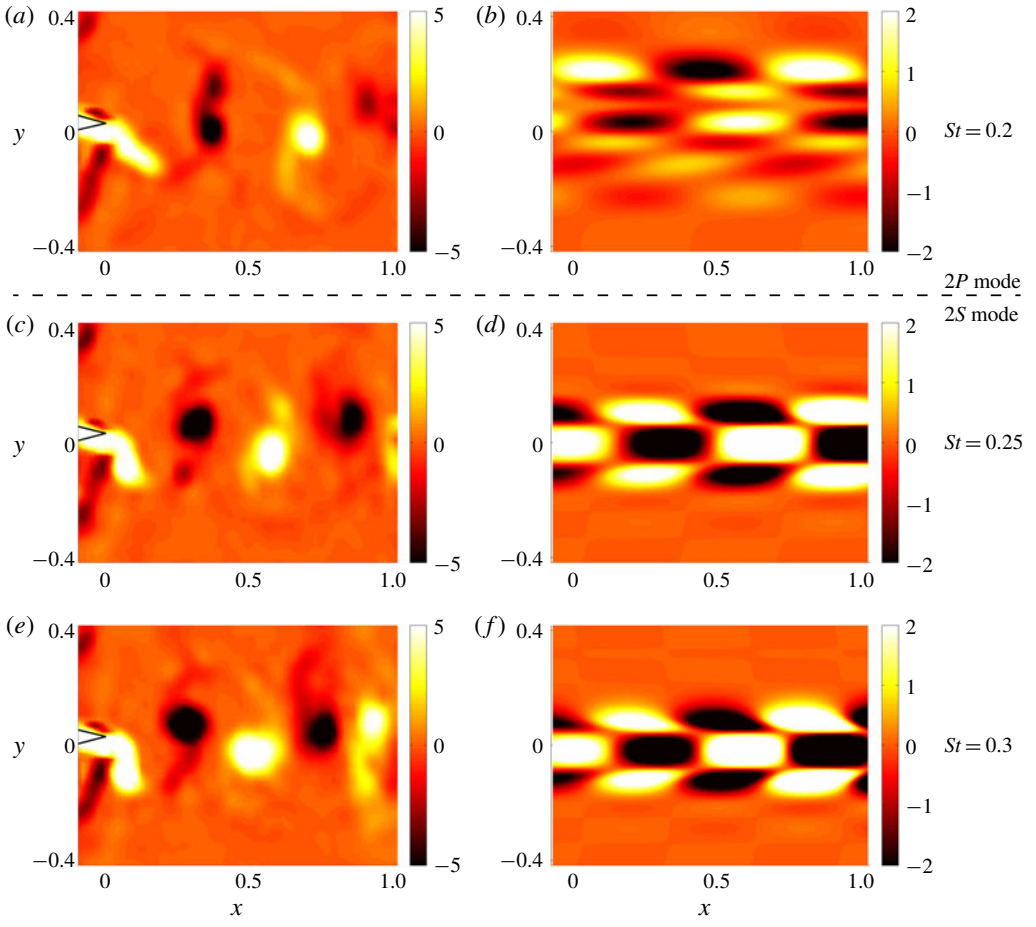

FIGURE 47. Observed wake structures for $\lambda^* = 4$ at (*a*) $St = 0.2$, (*c*) $St = 0.25$ and (*e*) $St = 0.3$. The vorticity perturbations (*b*), (*d*) and (*f*) are at the same parameters, respectively. A transition from a $2P$ wake to a $2S$ wake (dashed line) is observed. Reproduction with permission from Moored *et al.* (2012).

can now be associated with a specific wake mode. There is a resonant frequency for the $2P$ wake mode and a resonant frequency for the $2S$ wake mode (as labelled in figure 46*a*).

These wake resonance results, although derived in the context of manta ray locomotion, are expected to hold more generally. When combined with the experiments of Clark & Smits (2006) and Dewey *et al.* (2012), we now have a preliminary prescription for efficient unsteady propulsion. First, tuning the driving frequency to a wake resonant frequency results in a local peak in efficiency. Second, there may be multiple wake resonant frequencies relating to multiple peaks in efficiency. Third, some observed wake structures will transition when the wake instability modes transition. We see that a 2S wake structure is not the only wake

mode that leads to efficient locomotion and other wake modes such as a 2P mode can also lead to locally efficient propulsion. The global maximum in efficiency will be based on the kinematics of motion as well as the shape of the fin or device. That is, for one set of kinematics and one propulsor shape a 2P mode may be the most efficient wake mode to utilize, while for another set of kinematics and a different propulsor shape a 2S mode may be the optimally efficient wake mode.

In this respect, Linden & Turner (2001) and Dabiri (2009) have interpreted the structure of wakes generated by swimmers in terms of optimal vortex formation, a concept that was originally proposed in terms of vortex ring formation Gharib, Rambod & Shariff (1998). There may well be a connection between this concept and the idea of wake resonance, and this may be a profitable direction to explore in future work.

6. General observations

This may be a good place to end. I have attempted to give a perspective on undulatory and oscillatory swimming mechanisms, from a reasonably fundamental point of view. In doing so I have not addressed much of the other research that is relevant to swimming. I have largely ignored the strong connections to the fluid–structure interaction community, and to the extensive work on non-steady swimming, gust response, or other aggressive manoeuvers. Similarly, I have not highlighted the experiments done on entire fish, either in vivo or on robotic imitations, and passed over many of the computations of the flow field developed by swimming animals. Nor have I addressed the possible benefits of coordinated swimming, or swimming near the sea bottom, fin–fin interactions and many other interesting features of swimming as seen in nature. These are among the topics that I have neglected in order to focus on more basic theory and modelling efforts.

Within this restricted focus, I find that theory and modelling remain central to developing our understanding of swimming, and that observations on the fluid dynamics of simple membranes and foils in unsteady motion can illustrate much of the underlying physics seen. In particular, experiments and theory agree that the more important velocity scale is the characteristic lateral velocity of the tail motion rather than the swimming speed. Although the swimming speed is the most important factor in biology, in that it relates to survival, it is the characteristic lateral velocity of the tail motion that largely governs performance. The primacy of the lateral velocity over the swimming speed as the correct velocity scale erases to a large extent the difference between the results obtained in a tethered mode, compared to those obtained using a free swimming condition.

More particular observations are as follows. First, there is no one-to-one connection between the integrated swimming performance and the details of the wake structure. In this respect, wake resonance theory reveals the possibility of

multiple wake structures that exhibit high efficiency, while also helping to identify the conditions for efficient swimming. Second, there are fundamental differences between the study of rigid propulsors, and flexible ones. Animal locomotion usually involves fins with some level of flexibility, passive or active, and the distinction from rigid foils is important to remember since flexibility can be used to improve efficiency. Third, animals propel themselves using a wide variety of actions, which may combine undulatory motion with heaving and pitching motions. Studying heaving or pitching motions by themselves will only give limited insight into actual animal locomotion, and combined heave and pitch motions with an appropriate phase difference seem essential to achieve high performance. Fourth, the effects of Reynolds number are often ignored, based on the assumption that the unsteadiness (characterized by the Strouhal number or the reduced frequency), is the major physical phenomenon, and that viscous effects are secondary. Although we have been guilty of making this assumption at various times ourselves, it turns out that viscous effects play a critical role in determining the thrust and efficiency, and so any assumptions about Reynolds number effects need to be carefully substantiated (Floryan *et al.* 2018). Likewise, the shape of the foil influences its drag performance, and we have seen that optimizing the foil shape can result in substantial improvements in performance. In the context of fish swimming, the recent computations by Haibo Dong and his colleagues at UVA have shown that oscillation of the head and front body region in tuna acts to reduce the bending body coefficient of drag by 22 % (private communication). In addition, George Lauder and his colleagues at Harvard are finding very consistent head yaw patterns across species (private communication), and Gemmell *et al.* (2015) and Gemmell *et al.* (2016) have reported that the negative pressures associated with head movements in lampreys can lead to a strong 'pulling' contribution to thrust. Hence, there are undoubtedly other factors in addition to reducing drag that contribute to enhancing fish swimming efficiency. Fifth, cautionary remarks should also be made regarding changing aspect ratio, although we are close to a reasonable understanding of these effects. In contrast, we are far from understanding the effects of changing the planform shape. Sixth, almost all laboratory and computational work has been done on foils that are sinusoidally actuated, although non-sinusoidal gaits may be beneficial in some circumstances. In this context, the positive effects of intermittent swimming are now well recognized.

As a final remark, while it is true that the investigation of the mechanics of swimming is inspired by biological organisms, it is also true that such engineering studies have broadened our understanding of the performance of animals. In this area of research, biology and engineering are tightly intertwined, to the benefit of all.

Acknowledgements and a personal note

One of the first opportunities I ever had for snorkelling on a world-class reef was at Coral Bay on the western coast of Australia in about 2002. As part of an excursion to nearby Exmouth, I went swimming with manta rays. I had never seen such fluid grace and precision in any underwater animal before, and upon my return to Princeton I resolved to learn more about the mechanics of manta swimming. I was able to interest a talented senior, R. Clark, in designing and performing some water channel experiments on a robotic imitation of manta pectoral fin motion. This work turned into a masters thesis, and eventually led to the publication of Clark & Smits (2006). These experiences stimulated in me a new interest in underwater propulsion, using flexible and rigid foils of low aspect ratio. I found an abstract beauty in the formation and development of the wake, and it is a remarkable experience to see the wake generated in real time, and watch the exquisite detail present in the vortex formation and interaction. I was hooked, and so I was determined to find ways to continue this line of research. Fortunately, I became part of a team led by A. Cohen to study lamprey propulsion, which eventually led me back to manta rays, and then on to tuna, through two separate ONR-MURI efforts, both led by H. Bart-Smith. These efforts introduced me to F. Fish and G. Lauder, two of the key biologists who study swimming, who continue to be sources of inspiration to me. The research presented in this article was primarily supported by ONR through Program Manager R. Brizzolara. I would like to thank F. Fish for providing the biological data used in figure 2, and D. Floryan for preparing figure 32. D. Floryan, F. Fish, G. Lauder, T. Van Buren, L. Ding and T. Saxton-Fox gave constructive comments on an earlier draft and suggested some additional reference material, and T. Van Buren helped in preparing the figures. I am very grateful for their assistance, but of course I am solely responsible for any errors or omissions. H. Bart-Smith has been an amazing team leader and colleague, and a steadfast believer in the beautiful example given by manta rays. I am also deeply indebted to A. Cohen and L. Fauci who kept the flame burning on the NSF-NIH lamprey project. Finally, this article is based for the most part on the efforts of my graduate and undergraduate students, postdocs and visiting scholars. Thanks for the fun ride.

References

AKOZ, E. & MOORED, K. W. 2018 Unsteady propulsion by an intermittent swimming gait. *J. Fluid Mech.* **834**, 149–172.

ALBEN, S. 2008 Optimal flexibility of a flexible appendage in an inviscid fluid. *J. Fluid Mech.* **614**, 355–380.

ALBEN, S., WITT, C., BAKER, T. V., ANDERSON, E. & LAUDER, G. V. 2012 Dynamics of freely swimming flexible foils. *Phys. Fluids* **24**, 051901.

ALEXANDER, R. M. 2003 *Principles of Animal Locomotion*. Princeton University Press.

ALLEN, J. J. & SMITS, A. J. 2001 Energy harvesting eel. *J. Fluids Struct.* **15** (3–4), 629–640.

ANDERSON, J. M., STREITLIEN, K., BARRETT, D. S. & TRIANTAFYLLOU, M. S. 1998 Oscillating foils of high propulsive efficiency. *J. Fluid Mech.* **360**, 41–72.

AYANCIK, F., ZHONG, Q., QUINN, D. B., BRANDES, A., BART-SMITH, H. & MOORED, K. W. 2019 Scaling laws for the propulsive performance of three-dimensional pitching propulsors. *J. Fluid Mech.* **871**, 1117–1138.

BAINBRIDGE, R. 1958 The speed of swimming of fish as related to size and to the frequency and amplitude of the tail beat. *J. Expl Biol.* **35** (1), 109–133.

BAINBRIDGE, R. 1963 Caudal fin and body movement in the propulsion of some fish. *J. Expl Biol.* **40** (1), 23–56.

BLAKE, R. W. 1983*a* *Fish Locomotion*. CUP Archive.

BLAKE, R. W. 1983*b* Functional design and burst-and-coast swimming in fishes. *Can. J. Zool.* **61** (11), 2491–2494.

BRENNEN, C. E. 1982 A review of added mass and fluid inertial forces. *Tech. Rep.* CR 82.010. Naval Civil Engineering Laboratory.

BUCHHOLZ, J. H. J. & SMITS, A. J. 2005 Wake of a low aspect ratio pitching plate. *Phys. Fluids* **17** (9), 091102.

BUCHHOLZ, J. H. J. & SMITS, A. J. 2006 On the evolution of the wake structure produced by a low-aspect-ratio pitching panel. *J. Fluid Mech.* **546**, 433–443.

BUCHHOLZ, J. H. J. & SMITS, A. J. 2008 The wake structure and thrust performance of a rigid low-aspect-ratio pitching panel. *J. Fluid Mech.* **603**, 331–365.

CHOMAZ, J.-M. 2005 Global instabilities in spatially developing flows: non-normality and nonlinearity. *Annu. Rev. Fluid Mech.* **37**, 357–392.

CHOPRA, M. G. 1974 Hydromechanics of lunate-tail swimming propulsion. *J. Fluid Mech.* **64** (02), 375–392.

CHOPRA, M. G. & KAMBE, T. 1977 Hydromechanics of lunate-tail swimming propulsion. Part 2. *J. Fluid Mech.* **79** (1), 49–69.

CHUNG, M. H. 2009 On burst-and-coast swimming performance in fish-like locomotion. *Bioinspir. Biomim.* **4** (3), 036001.

CLARK, R. P. & SMITS, A. J. 2006 Thrust production and wake structure of a batoid-inspired oscillating fin. *J. Fluid Mech.* **562**, 415–429.

COLGATE, J. E. & LYNCH, K. M. 2004 Mechanics and control of swimming: a review. *IEEE J. Ocean. Engng* **29** (3), 660–673.

DABIRI, J. O. 2009 Optimal vortex formation as a unifying principle in biological propulsion. *Annu. Rev. Fluid Mech.* **41**, 17–33.

DAI, H., LUO, H., DE SOUSA, P. J. S. A. F. & DOYLE, J. F. 2012 Thrust performance of a flexible low-aspect-ratio pitching panel. *Phys. Fluids* **24** (101903), 1–9.

DEWEY, P. A., BOSCHITSCH, B. M., MOORED, K. W., STONE, H. A. & SMITS, A. J. 2013 Scaling laws for the thrust production of flexible pitching panels. *J. Fluid Mech.* **732**, 29–46.

DEWEY, P. A., CARRIOU, A. & SMITS, A. J. 2012 On the relationship between efficiency and wake structure of a batoid-inspired oscillating fin. *J. Fluid Mech.* **691**, 245–266.

DHANAK, M. R. & BERNARDINIS, B. 1981 The evolution of an elliptic vortex ring. *J. Fluid Mech.* **109**, 189–216.

DICKINSON, M. H. 1996 Unsteady mechanisms of force generation in aquatic and aerial locomotion. *Am. Zool.* **36** (6), 537–554.

DONG, H., MITTAL, R., BOZKURTTAS, M. & NAJJAR, F. 2005 Wake structure and performance of finite aspect-ratio flapping foils. *AIAA Paper* 2005-0081.

DONLEY, J. M. & DICKSON, K. A. 2000 Swimming kinematics of juvenile kawakawa tuna (Euthynnus affinis) and chub mackerel (Scomber japonicus). *J. Expl Biol.* **203** (20), 3103–3116.

DRUCKER, E. G. & LAUDER, G. V. 2001 Locomotor function of the dorsal fin in teleost fishes: experimental analysis of wake forces in sunfish. *J. Expl Biol.* **204** (17), 2943–2958.

ELOY, C. 2012 Optimal Strouhal number for swimming animals. *J. Fluids Struct.* **30**, 205–218.

FISH, F. E. 1987 Kinematics and power output of jet propulsion by the frogfish genus Antennarius (Lophiiformes: Antennariidae). *Copeia* **1987** (4), 1046–1048.

FISH, F. E. 1996 Transitions from drag-based to lift-based propulsion in mammalian swimming. *Am. Zool.* **36** (6), 628–641.

FISH, F. E. 2001 Swimming in fish. In *eLS*. John Wiley & Sons.

FISH, F. E., DONG, H., ZHU, J. J. & BART-SMITH, H. 2017 Kinematics and hydrodynamics of mobuliform swimming: oscillatory winged propulsion by large pelagic batoids. *J. Mar. Technol. Soc.* **51** (5), 35–47.

FISH, F. E., FEGELY, J. F. & XANTHOPOULOS, C. J. 1991 Burst-and-coast swimming in schooling fish (Notemigonus crysoleucas) with implications for energy economy. *Comp. Biochem. Physiol. A Mol. Integr. Physiol.* **100A** (3), 633–637.

FISH, F. E. & LAUDER, G. V. 2006 Passive and active flow control by swimming fishes and mammals. *Annu. Rev. Fluid Mech.* **38**, 193–224.

FISH, F. E. & LAUDER, G. V. 2013 Not just going with the flow. *Am. Sci.* **101** (2), 114–123.

FISH, F. E., LEGAC, P., WILLIAMS, T. M. & WEI, T. 2014 Measurement of hydrodynamic force generation by swimming dolphins using bubble DPIV. *J. Expl Biol.* **217** (2), 252–260.

FISH, F. E. & ROHR, J. J. 1999 Review of dolphin hydrodynamics and swimming performance. *Tech. Rep.* Space and Naval Warfare Systems Command, San Diego CA.

FISH, F. E., SCHREIBER, C. M., MOORED, K. W., LIU, G., DONG, H. & BART-SMITH, H. 2016 Hydrodynamic performance of aquatic flapping: efficiency of underwater flight in the manta. *Aerospace* **3** (3), 1–24.

FLAMMANG, B. E., LAUDER, G. V., TROOLIN, D. R. & STRAND, T. 2011 Volumetric imaging of shark tail hydrodynamics reveals a three-dimensional dual-ring vortex wake structure. *Proc. R. Soc. Lond.* B **278** (1725), 3670–3678.

FLORYAN, D. & ROWLEY, C. W. 2018 Clarifying the relationship between efficiency and resonance for flexible inertial swimmers. *J. Fluid Mech.* **853**, 271–300.

FLORYAN, D., VAN BUREN, T., ROWLEY, C. W. & SMITS, A. J. 2017*a* Scaling the propulsive performance of heaving and pitching foils. *J. Fluid Mech.* **822**, 386–397.

FLORYAN, D., VAN BUREN, T. & SMITS, A. J. 2017*b* Forces and energetics of intermittent swimming. *Acta Mechanica Sin.* **33** (4), 725–732.

FLORYAN, D., VAN BUREN, T. & SMITS, A. J. 2018 Efficient cruising for swimming and flying animals is dictated by fluid drag. *Proc. Natl Acad. Sci. USA* **115** (32), 8116–8118.

FLORYAN, D., VAN BUREN, T. & SMITS, A. J. 2019 Swimmers' wakes are not reliable indicators of swimming performance. arXiv:1908.10826.

GARRICK, I. E. 1936 Propulsion of a flapping and oscillating airfoil. *Tech. Rep.* 567. National Advisory Committee for Aeronautics.

GAZZOLA, M., ARGENTINA, M. & MAHADEVAN, L. 2014 Scaling macroscopic aquatic locomotion. *Nat. Phys.* **10** (10), 758–761.

GEMMELL, B. J., COLIN, S. P., COSTELLO, J. H. & DABIRI, J. O. 2015 Suction-based propulsion as a basis for efficient animal swimming. *Nat. Commun.* **6**, 8790.

GEMMELL, B. J., FOGERSON, S. M., COSTELLO, J. H., MORGAN, J. R., DABIRI, J. O. & COLIN, S. P. 2016 How the bending kinematics of swimming lampreys build negative pressure fields for suction thrust. *J. Expl Biol.* **219** (24), 3884–3895.

GHARIB, M., RAMBOD, E. & SHARIFF, K. 1998 A universal time scale for vortex ring formation. *J. Fluid Mech.* **360**, 121–140.

GRAY, J. 1933 Studies in animal locomotion III. The propulsive mechanism of the whiting (Gadus merlangus). *J. Expl Biol.* **10**, 391–402.

GRAY, J. 1968 *Animal Locomotion*. Weidenfeld & Nicolson.

GRAY, J. & HANCOCK, G. J. 1955 The propulsion of sea-urchin spermatozoa. *J. Expl Biol.* **32** (4), 802–814.

GREEN, M. A., ROWLEY, C. W. & SMITS, A. J. 2011 The unsteady three-dimensional wake produced by a trapezoidal pitching panel. *J. Fluid Mech.* **685**, 117–145.

GREEN, M. A. & SMITS, A. J. 2008 Effects of three-dimensionality on thrust production by a pitching panel. *J. Fluid Mech.* **615**, 211–220.

GUGLIELMINI, L. 2004 Modeling of thrust generating foils. PhD thesis, University of Genoa, Genoa, Italy.

HEATHCOTE, S., WANG, Z. & GURSUL, I. 2008 Effect of spanwise flexibility on flapping wing propulsion. *J. Fluids Struct.* **24**, 183–199.

HULTMARK, M., LEFTWICH, M. C. & SMITS, A. J. 2007 Flowfield measurements in the wake of a robotic lamprey. *Exp. Fluids* **43**, 683–690.

HUNT, J. C. R., WRAY, A. A. & MOIN, P. 1988 Eddies, stream, and convergence zones in turbulent flows. *Center for Turbulence Research Report* CTR-S88 pp. 193–208.

KARPOUZIAN, G., SPEDDING, G. & CHENG, H. K. 1990 Lunate-tail swimming propulsion. Part 2. Performance analysis. *J. Fluid Mech.* **210**, 329–351.

KATZ, J. & PLOTKIN, A. 2001 *Low-Speed Aerodynamics*, vol. 13. Cambridge University Press.

KAYA, M. & TUNCER, I. H. 2007 Nonsinusoidal path optimization of a flapping airfoil. *AIAA J.* **45**, 2075–2082.

KING, J. T., KUMAR, R. & GREEN, M. A. 2018 Experimental observations of the three-dimensional wake structures and dynamics generated by a rigid, bioinspired pitching panel. *Phys. Rev. Fluids* **3** (3), 034701.

KRAMER, D. L. & MCLAUGHLIN, R. L. 2001 The behavioral ecology of intermittent locomotion 1. *Am. Zool.* **41** (2), 137–153.

LANGERHANS, R. B. & REZNICK, D. N. 2010 Ecology and evolution of swimming performance in fishes: predicting evolution with biomechanics. In *Fish Locomotion: An Eco-ethological Perspective*, pp. 200–248. Science Publishers.

LAUDER, G. V. 2000 Function of the caudal fin during locomotion in fishes: kinematics, flow visualization, and evolutionary patterns. *Am. Zool.* **40** (1), 101–122.

LAUDER, G. V., LIM, J., SHELTON, R., WITT, C., ANDERSON, E. & TANGORRA, J. L. 2011 Robotic models for studying undulatory locomotion in fishes. *Mar. Technol. Soc. J.* **45** (4), 41–55.

LAUDER, G. V. & TYTELL, E. D. 2005 Hydrodynamics of undulatory propulsion. *Fish Physiol.* **23**, 425–468.

LEFTWICH, M. C. & SMITS, A. J. 2011 Thrust production by a mechanical swimming lamprey. *Exp. Fluids* **50** (5), 1349–1355.

LENTINK, D., MUIJRES, F. T., DONKER-DUYVIS, F. J. & VAN LEEUWEN, J. L. 2008 Vortex-wake interactions of a flapping foil that models animal swimming and flight. *J. Expl Biol.* **211** (2), 267–273.

LEWIN, G. C. & HAJ-HARIRI, H. 2003 Modelling thrust generation of a two-dimensional heaving airfoil in a viscous flow. *J. Fluid Mech.* **492**, 339–362.

LI, G. J., LUODIN, Z. H. U. & LU, X. Y. 2012 Numerical studies on locomotion performance of fish-like tail fins. *J. Hydrodyn.* B **24** (4), 488–495.

LIAO, J. C. 2007 A review of fish swimming mechanics and behaviour in altered flows. *Phil. Trans. R. Soc. Lond.* B **362** (1487), 1973–1993.

LIGHTHILL, M. J. 1960 Note on the swimming of slender fish. *J. Fluid Mech.* **9** (2), 305–317.

LIGHTHILL, M. J. 1969 Hydromechanics of aquatic animal propulsion. *Annu. Rev. Fluid Mech.* **1** (1), 413–446.

LIGHTHILL, M. J. 1970 Aquatic animal propulsion of high hydromechanical efficiency. *J. Fluid Mech.* **44** (02), 265–301.

LIGHTHILL, M. J. 1971 Large-amplitude elongated-body theory of fish locomotion. *Proc. R. Soc. Lond.* B **179**, 125–138.

LINDEN, P. F. & TURNER, J. S. 2001 The formation of 'optimal' vortex rings, and the efficiency of propulsion devices. *J. Fluid Mech.* **427**, 61–72.

LINDSEY, C. C. 1978 Form, function and locomotory habits in fish. In *Fish Physiology Vol. VII Locomotion* (ed. W. S. Hoar & D. J. Randall), pp. 1–100. Academic Press.

LIU, P. & BOSE, N. 1993 Propulsive performance of three naturally occurring oscillating propeller planforms. *Ocean Engng* **20** (1), 57–75.

LIU, T., WANG, S., ZHANG, X. & HE, G. 2014 Unsteady thin-airfoil theory revisited: application of a simple lift formula. *AIAA J.* **53** (6), 1492–1502.

MOORED, K. & QUINN, D. B. 2018 Inviscid scaling laws of a self-propelled pitching airfoil. *AIAA J.* 1–15.

MOORED, K. W., DEWEY, P. A., SMITS, A. J. & HAJ-HARIRI, H. 2012 Hydrodynamic wake resonance as an underlying principle of efficient unsteady propulsion. *J. Fluid Mech.* **708**, 329–348.

MÜLLER, U. K., VAN DEN HEUVEL, B. L. E., STAMHUIS, E. J. & VIDELER, J. J. 1997 Fish foot prints: morphology and energetics of the wake behind a continuously swimming mullet (Chelon labrosus Risso). *J. Expl Biol.* **200** (22), 2893–2906.

MUNK, M. M. 1924 The aerodynamic forces on airship hulls. *NACA Tech. Rep.* NACA-TR-1845.

NAUEN, J. C. & LAUDER, G. V. 2002 Hydrodynamics of caudal fin locomotion by chub mackerel, Scomber japonicus (Scombridae). *J. Expl Biol.* **205** (12), 1709–1724.

PATTON, K. T. 1965 An experimental determination of hydrodynamic masses and mechanical impedances. *Tech. Rep.* AD-758 096. Navy Underwater Sound Laboratory, New London CT.

QUINN, D. B., LAUDER, G. V. & SMITS, A. J. 2014 Scaling the propulsive performance of heaving flexible panels. *J. Fluid Mech.* **738**, 250–267.

QUINN, D. B., LAUDER, G. V. & SMITS, A. J. 2015 Maximizing the efficiency of a flexible propulsor using experimental optimization. *J. Fluid Mech.* **767**, 430–448.

RAMANANARIVO, S., GODOY-DIANA, R. & THIRIA, B. 2011 Rather than resonance, flapping wing flyers may play on aerodynamics to improve performance. *Proc. Natl Acad. Sci. USA* **108** (15), 5964–5969.

RAMANANARIVO, S., GODOY-DIANA, R. & THIRIA, B. 2013 Passive elastic mechanism to mimic fish-muscle action in anguilliform swimming. *J. R. Soc. Interface* **10** (88), 20130667.

READ, D. A., HOVER, F. S. & TRIANTAFYLLOU, M. S. 2003 Forces on oscillating foils for propulsion and maneuvering. *J. Fluids Struct.* **17** (1), 163–183.

ROHR, J. J. & FISH, F. E. 2004 Strouhal numbers and optimization of swimming by odontocete cetaceans. *J. Expl Biol.* **207** (10), 1633–1642.

ROSENBERGER, L. 2001 Pectoral fin locomotion in batoid fishes: undulation versus oscillation. *J. Expl Biol.* **204**, 379–394.

ROSENBERGER, L. J. & WESTNEAT, M. W. 1999 Functional morphology of undulatory pectoral fin locomotion in the stingray Taeniura lymma (Chondrichthyes: Dasyatidae). *J. Expl Biol.* **202** (24), 3523–3539.

SAMBILAY, V. C. JR 1990 Interrelationships between swimming speed, caudal fin aspect ratio and body length of fishes. *Fishbyte* **8** (3), 16–20.

SCHERER, J. O. 1968 Experimental and theoretical investigation of large amplitude oscillation foil propulsion systems. *Tech. Rep.* 662-1. Hydronautics Inc. Laurel, MD.

SEDOV, L. I. 1965 *Two-dimensional Problems in Hydrodynamics and Aerodynamics*. Interscience Publishers.

SENTÜRK, U., BRUNNER, D., JASAK, H., HERZOG, N., ROWLEY, C. W. & SMITS, A. J. 2019 Benchmark simulations of flow past rigid bodies using an open-source, sharp interface immersed boundary method. *Prog. Comput. Fluid Dyn* (submitted) doi:10.1504/PCFD.2017.10009753.

SENTÜRK, U. & SMITS, A. J. 2018 Numerical simulations of the flow around a square pitching panel. *J. Fluids Struct.* **76**, 454–468.

SENTÜRK, U. & SMITS, A. J. 2019 Reynolds number scaling of the propulsive performance of a pitching hydrofoil. *AIAA J.* (submitted).

SFAKIOTAKIS, M., LANE, D. M. & DAVIES, J. B. C. 1999 Review of fish swimming modes for aquatic locomotion. *IEEE J. Ocean. Engng* **24** (2), 237–252.

SHYY, W., AONO, H., CHIMAKURTHI, S. K., TRIZILA, P., KANG, C.-K., CESNIK, C. E. S. & LIU, H. 2010 Recent progress in flapping wing aerodynamics and aeroelasticity. *Prog. Aerosp. Sci.* **46**, 284–327.

SUMICH, J. L. & MORRISSEY, J. F. 2004 *Introduction to the Biology of Marine Life*. Jones & Bartlett Learning.

TAYLOR, G. I. 1952 Analysis of the swimming of long and narrow animals. *Proc. R. Soc. Lond.* A **214** (1117), 158–183.

TAYLOR, G. K. 2018 Simple scaling law predicts peak efficiency in oscillatory propulsion. *Proc. Natl Acad. Sci. USA* **115** (32), 8063–8065.

TAYLOR, G. K., NUDDS, R. L. & THOMAS, A. L. R. 2003 Flying and swimming animals cruise at a Strouhal number tuned for high power efficiency. *Nature* **435**, 707–711.

THEODORSEN, T. 1935 General theory of aerodynamic instability and the mechanism of flutter. *NACA Tech. Rep.* 496; originally published as ARR-1935.

THIRIA, B. & GODOY-DIANA, R. 2010 How wing compliance drives the efficiency of self-propelled flapping flyers. *Phys. Rev.* E **82**, 015303(R).

TRIANTAFYLLOU, G. S., TRIANTAFYLLOU, M. S. & GROSENBAUGH, M. A. 1993 Optimal thrust development in oscillating foils with application to fish propulsion. *J. Fluids Struct.* **7** (2), 205–224.

TRIANTAFYLLOU, M. S., HOVER, F. S., TECHET, A. H. & YUE, D. K. P. 2005 Review of hydrodynamic scaling laws in aquatic locomotion and fishlike swimming. *Appl. Mech. Rev.* **58** (4), 226–237.

TRIANTAFYLLOU, M. S. & TRIANTAFYLLOU, G. S. 1995 An efficient swimming machine. *Sci. Am.* **272** (3), 64–70.

TRIANTAFYLLOU, M. S., TRIANTAFYLLOU, G. S. & YUE, D. K. P. 2000 Hydrodynamics of fishlike swimming. *Annu. Rev. Fluid Mech.* **32** (1), 33–53.

TSIEN, H.-S. 1938 Supersonic flow over an inclined body of revolution. *J. Aero. Sci.* **5** (12), 480–483.

TUNCER, I. H. & KAYA, M. 2005 Optimization of flapping airfoils for maximum thrust and propulsive efficiency. *AIAA J.* **43** (11), 2329–2336.

TYTELL, E. D. & LAUDER, G. V. 2004 The hydrodynamics of eel swimming I. Wake structure. *J. Expl Biol.* **207**, 1825–1841.

VAN BUREN, T., FLORYAN, D., BRUNNER, D., ŞENTÜRK, U. & SMITS, A. J. 2017*a* Impact of trailing edge shape on the wake and propulsive performance of pitching panels. *Phys. Rev. Fluids* **2** (1), 014702.

VAN BUREN, T., FLORYAN, D., QUINN, D. & SMITS, A. J. 2017*b* Nonsinusoidal gaits for unsteady propulsion. *Phys. Rev. Fluids* **2** (5), 053101.

VAN BUREN, T., FLORYAN, D. & SMITS, A. J. 2018*a* Scaling and performance of simultaneously heaving and pitching foils. *AIAA J.* 1–12.

VAN BUREN, T., FLORYAN, D. & SMITS, A. J. 2019*a* Bio-inspired underwater propulsors. In *Bioinspired Design* (ed. L. Daniel & W. Soboyejo), chap. 11. Cambridge University Press.

VAN BUREN, T., FLORYAN, D., SMITS, A. J., PAN, H., BODE-OKE, A. T. & DONG, H. 2019b Optimizing foil shape for efficient unsteady propulsion *AIAA Paper* 2019-1379.

VAN BUREN, T., FLORYAN, D., WEI, N. & SMITS, A. J. 2018*b* Flow speed has little impact on propulsive characteristics of oscillating foils. *Phys. Rev. Fluids* **3** (1), 013103.

VIDELER, J. J. 1993 *Fish Swimming*, Fish and Fisheries Series, vol. 10. Chapman & Hall.

VIDELER, J. J. & WEIHS, D. 1982 Energetic advantages of burst-and-coast swimming of fish at high speeds. *J. Expl Biol.* **97** (1), 169–178.

VON ELLENRIEDER, K. D., PARKER, K. & SORIA, J. 2003 Flow structures behind a heaving and pitching finite-span wing. *J. Fluid Mech.* **490**, 129–138.

VON KÁRMÁN, T. & GABRIELLI, G. 1950 What price speed? Specific power required for propulsion of vehicles. *Mech. Engng* **72**, 775–781.

WEBB, P. W. 1973 Effects of partial caudal-fin amputation on the kinematics and metabolic rate of underyearling sockeye salmon (Oncorhynchus nerka) at steady swimming speeds. *J. Expl Biol.* **59** (3), 565–582.

WEBB, P. W. 1975 Hydrodynamics and energetics of fish propulsion. *Bull. Fish. Res. Board Can.* **190**, 1–159.

WEBB, P. W. 1984 Form and function in fish swimming. *Sci. Am.* **251** (1), 72–83.

WEBB, P. W., KOSTECKI, P. T. & STEVENS, E. D. 1984 The effect of size and swimming speed on locomotor kinematics of rainbow trout. *J. Expl Biol.* **109** (1), 77–95.

WEIHS, D. 1972 Semi-infinite vortex trails, and their relation to oscillating airfoils. *J. Fluid Mech.* **54** (4), 679–690.

WILGA, C. A. D. & LAUDER, G. V. 2004 Biomechanics of locomotion in sharks, rays, and chimeras. In *Biology of Sharks and Their Relatives* (ed. J. C. Carrier, J. A. Musick & M. R. Heithaus), pp. 139–164. CRC Press.

WILLIAMSON, C. H. K. & ROSHKO, A. 1988 Vortex formation in the wake of an oscillating cylinder. *J. Fluid Struct.* **2**, 355–381.

WU, T. Y. T. 1961 Swimming of a waving plate. *J. Fluid Mech.* **10** (3), 321–344.

WU, T. Y. T. 1971*a* Hydromechanics of swimming of fishes and cetaceans. In *Advances in Applied Mechanics* (ed. C. S. Yih), vol. 11, pp. 1–63. Elsevier.

WU, T. Y. T. 1971*b* Hydromechanics of swimming propulsion. Part 1. Swimming of a two-dimensional flexible plate at variable forward speeds in an inviscid fluid. *J. Fluid Mech.* **46** (2), 337–355.

WU, T. Y. T. 1971*c* Hydromechanics of swimming propulsion. Part 2. Some optimum shape problems. *J. Fluid Mech.* **46** (3), 521–544.

WU, T. Y. T. 2011 Fish swimming and bird/insect flight. *Annu. Rev. Fluid Mech.* **43**, 25–58.

YOUNG, J. & LAI, J. C. S. 2007 Mechanisms influencing the efficiency of oscillating airfoil propulsion. *AIAA J.* **45** (7), 1695–1702.

YOUNG, J., LAI, J. C. S., KAYA, M. & TUNCER, I. H. 2006 Thrust and efficiency of propulsion by oscillating foils. In *Computational Fluid Dynamics 2004*, pp. 313–318. Springer.

ZHANG, J. 2017 Footprints of a flapping wing. *J. Fluid Mech.* **818**, 1–4.

ZHONG, S., MOORED, K. W., PINEDO, V., GARCIA-GONZALEZ, J. & SMITS, A. J. 2013 The flow field and axial thrust generated by a rotating rigid helix at low Reynolds numbers. *Exp. Therm. Fluid Sci.* **46**, 1–7.